An Investigation of Fretting Wear in Aerospace Applications

by
Hermann Nortjé

Thesis presented in partial fulfilment of the requirements for the degree Master of Science in Engineering Management at the University of Stellenbosch

Supervisor: Prof. Guven Akdogan
Co-supervisor: Dr. Gert Adriaan Oosthuizen
Faculty of Engineering
Department of Industrial Engineering

December 2011

Declaration

By submitting this thesis/dissertation electronically, I declare that the entirety of the work contained therein is my own, original work, that I am the sole author thereof (save to the extent explicitly otherwise stated), that reproduction and publication thereof by Stellenbosch University will not infringe any third party rights and that I have not previously in its entirety or in part submitted it for obtaining any qualification.

December 2011

Abstract

Fretting wear results in the loss of fit and tolerance at contact interfaces. The aerospace and aircraft industry is severely impacted by fretting wear and fretting fatigue that frequently occurs in turbo machinery and riveted structural connections. There have been numerous studies, investigating the fretting phenomenon for these aerospace applications.

Literature available in regard to fretting wear encountered in these aerospace applications is limited. This study is therefore aimed at investigating the fretting wear encountered in aerospace application. An in-house fretting test apparatus was specially designed and developed in order to perform the fretting wear experiments. Ti-6Al-4V and Al7075-T6 are the two aerospace materials that were tested using the fretting test apparatus. An extensive experimental study was conducted in order to investigate the effect of the normal force on the fretting wear and friction behaviour of the two aerospace materials. The most severe of these experiments were identified and then repeated for up to 10^6 fretting cycles. Additional fretting wear experiments were also conducted between the two aerospace materials and cemented carbides, since the carbides are currently being utilized as coatings in some aerospace contacts that are prone to fretting induced damage.

The experimental study revealed that a decrease in the normal force resulted in an increase in the severity of the fretting wear of both aerospace materials. The additional fretting wear experiments involving carbide-metal contact couples found that Ti-6Al-4V and Al7075-T6 were prone to adhesive wear.

Opsomming

Knaagslytasie veroorsaak materiaalverlies by die kontakoppervlakke. Die lugvaart industrie is erg geraak deur knaagslytasie en knaaguitputting wat dikwels voorkom in turbo-enjin toepassings en strukturele verbindings. Daar was al talle studies gedoen oor die effek van knaag op lugvaart toepassings.

Literatuur met betrekking tot knaagslytasie in lugvaart toepassings is egter beperk. Hierdie studie was dus gemik daarop om knaagslytasie in sekere lugvaart toepassings te ondersoek. Tydens die studie is ŉ toetsopstelling ontwerp en ontwikkel om knaagslytasie eksperimente uit te voer. Ti-6Al-4V en Al7075-T6 is die twee lugvaartmateriale wat ondersoek is met behulp van die toetsopstelling. ŉ Omvattende eksperimentele studie is gedoen om die effek van die normaal krag op knaagslytasie en die wrywings gedrag van die lugvaartmateriale te ondersoek. Die eksperimente wat die ergste slytasie en hoogste wrywing getoon het, is herhaal vir 10^6 siklusse. Bykomende knaag eksperimente was ook tussen die twee lugvaartmateriale en sekere karbiede gedoen, aangesien karbiede tans as deklae in sommige lugvaart kontakte gebruik word.

Die eksperimentele studie het getoon dat 'n afname in die normale krag gelei het tot 'n toename in wrywing vir beide lugvaartmateriale. Die bykomende knaagslytasie eksperimente op karbied metaal pare het getoon dat Ti-6Al-4V en Al7075-T6twee lugvaart materiale nie in staat was om enige van die karbide te beskadig nie. Die lug-en Ruimte-materiaal aan die ander kant ervaar het kwaadaardige dra.

Acknowledgements

The Author expresses his gratitude to the following organizations and individuals for their contribution to this study:

DST/NRF Centre of Excellence in Strong Materials at the University of the Witwatersrand for funding.

Element 6 (pty).Ltd for providing facilities material testing.

Prof. G. Akdogan for his guidance, advice and forbearance.

Dr. G A Oosthuizen for his guidance and advice.

Dr. N Sacks for her guidance and advice.

My friends and family for their continuing support.

Table of Contents

List of Figures

List of Tables

1 Fretting Background and Literature Review

1.1 Nomenclature

Symbol	Description	Units
k	A constant. Typically in the range of 3.8 µm for slip amplitudes greater than 25 µm.	µm
d	Fretting/slip amplitde	µm
μ	Coefficient of friction	none
S_{fr}	Fretting fatigue strength	MPa
S_o	Fatigue strength in the absence of fretting	MPa
p_o	Contact pressure	MPa
M_i	Mass of the third body material	g
t	Time	s
Q_s	Source flow	g/s
Q_w	Wear flow	g/s
F_N	Normal force	N
F_T	Tangential excitation force	N
V	Sliding speed	N
F_R	Resisting/friction force	N
dW	Mass of matter detached during wear	g
dt	Unit time step	s
P	Applied pressure	MPa
K	Wear coefficient of the Archard equation	dimensionless

1.2 Introduction and Definitions

Tribology is the science and technology of the interfaces between two or more contacting surfaces in relative motion, and relates to friction, lubrication and wear [**1**]. Whenever two or more surfaces in contact are subjected to relative motion a phenomenon known as *wear* will occur. *Wear* is generally defined as damage of one or more surfaces, resulting in a progressive loss of material and/or dimension [**2**]. Fretting is the mechanical and chemical actions in which the contacting surfaces of two solid bodies are pressed together by a normal force and caused to execute oscillatory relative sliding motion [**3**]. Some authors regard fretting to be a form of reciprocating sliding wear, taking place at small relative displacements. There are however enough significant differences in the wear resulting from fretting to warrant the distinction. The *fretting*

interface refers to the contact interface between the surfaces of the two material bodies completing the fretting contact.

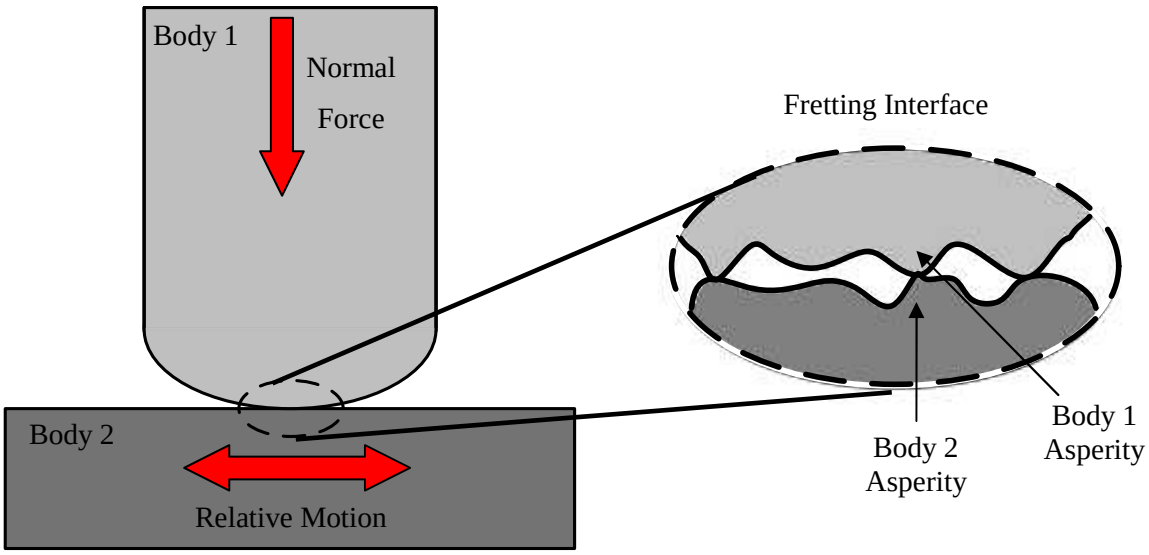

Figure 1.1: Fretting contact

Figure 1.1 provides a schematic representation of a fretting contact, also depiction the fretting interface. The *asperities* in the figure refer the microscopic irregularities on the surface of each body that form individual contact points between the bodies in question. The relative displacements between the contacting surfaces, resulting from the relative motion is known as *slip*. According to Szolwinski [**4**] the damage process associated with fretting is a synergistic competition between wear, corrosive and fatigue phenomenon. Accordingly the three main forms of fretting recognized are *fretting wear*, *fretting corrosion* and *fretting fatigue*. Collins [**3**] defines *fretting wear* as the change in the dimensions of one or both of the contacting surfaces completing the fretting contact, caused by wear directly attributed to the fretting process. The fretting wear process is generally thought of as a form of *abrasive wear*, which is a material removal process caused by hard particles forced to slide along on a surface [**2**]. According to Bock & Whitley [**5**] *fretting corrosion* is "*a form of accelerated atmospheric oxidation which occurs at the interface of contacting materials undergoing slight, cyclic relative motion*". Thus in essence *fretting corrosion* is a combination of *fretting wear* taking place in a corrosive environment. The fretting phenomenon is also capable of affecting the fatigue behaviour of materials. This process is known as *fretting fatigue* and results in the fatigue life reduction of the components involved [**6**]. During the *fretting fatigue* process the shear stress experienced by the materials in the fretting contact exceeds the fatigue strength of the materials, resulting in fatigue cracks.

The fretting phenomenon typically takes place at mechanical joints, leading to part fracture and loss of geometric precision. The most common fretting sites encountered in industry include:

- *Bolted joints*: Fretting fatigue plays an important role in lifetime of bolted joints, especially in the aircraft industry. According to Krishnakumar [**7**] fretting is major concern in the bolted structural members of aircraft.

- *Leaf springs*: The leaf springs used in the automobiles are subjected to varying stress and vibrations, as a result of varying road conditions. During study conducted by Aggarwal [**8**] it was discovered that shot peening and hard coatings will improve the fatigue life of leaf springs subjected to fretting conditions.
- *Spline Couplings*: The fretting phenomenon is also experienced in spline couplings in terms of fretting wear as well as fretting fatigue [**9**].
- *Wire ropes*: Wire ropes consist of many wires that are twisted together in order to form a single rope/cable. According to Chaplin [**10**] fretting wear and fretting fatigue is a major concern in the outer layers of wire ropes, resulting in the breakage of the wires in the outer layers of the wire ropes.
- *Bearings*: The fretting damage normally associated with bearing is known as false brinelling, occurring when loaded Hertzian contacts are subjected to fretting. According to Tillian [**11**] the fretting motion is caused by the repeated widening and narrowing of the Hertz area, as a result of time variable normal loading and/or slight angular oscillation. The movements responsible for creating the fretting motions are a result of a wide range of conditions, including the transportation of the bearings and the operation in environments subjected to vibrations.

Fretting was first identified in 1911 by Eden et al.[**12**], who identified the formation of iron oxide on the surfaces of test specimens being gripped by a test machine performing fatigue experiments. Tomlinson was however the first to conduct an official investigation of fretting in 1927 [**13**]. At that stage Tomlinson referred to the fretting phenomenon as rusting, due to the oxidation that took place between the surfaces at the contact interface. During his study Tomlinson investigated the effects of different parameters in order to find the cause of fretting. He concluded that the rusting was related to the tangential motion between the contacting surfaces [**13**].

1.3 Fretting Wear

Wear is defined as the process during which two or more material surfaces are pushed together and displaced [**14**]. During this process the material degradation takes place and material particles called “wear debris” are removed from the contact interface. Fretting wear can result in the loss of dimensional accuracy in mechanical and structural components. During the wear process the loss in dimensional accuracy can even further enhance wear process. In 1972 R.B. Waterhouse [**15**] proposed the following three simplified steps for the fretting wear mechanism:

- Step 1: The mechanical action of the fretting process disrupts the oxide films on the surface of the metal, exposing the clean metal. The clean surface would be extremely reactive in the presence of oxygen, resulting in rapid oxidation.

- Step 2: The removal of fine material particles from the surface by mechanical grinding. This is caused by direct shearing or local fatigue action, resulting in the formation of welds at contact points. These welds will then break at surfaces other than the origination surfaces. The atmosphere plays no role in this step of the process except if corrosion fatigue is caused by elevated fatigue levels.
- Step 3: Oxide debris resulting from one or both of the first two steps, form an abrasive powder which damages the surface even further.

By using the above mentioned mechanism the following four step progression of fretting wear damage of an arbitrary mechanical contact is depicted in Figure 1.2:

a) Accumulation of trapped particles.
b) Increase in the amount of oxide particles and the expansion of various contacting surfaces into a single unit.
c) Oxide particle spilling as a result of accumulation.
d) Pit formation as a result of the increasingly strong abrasive action.

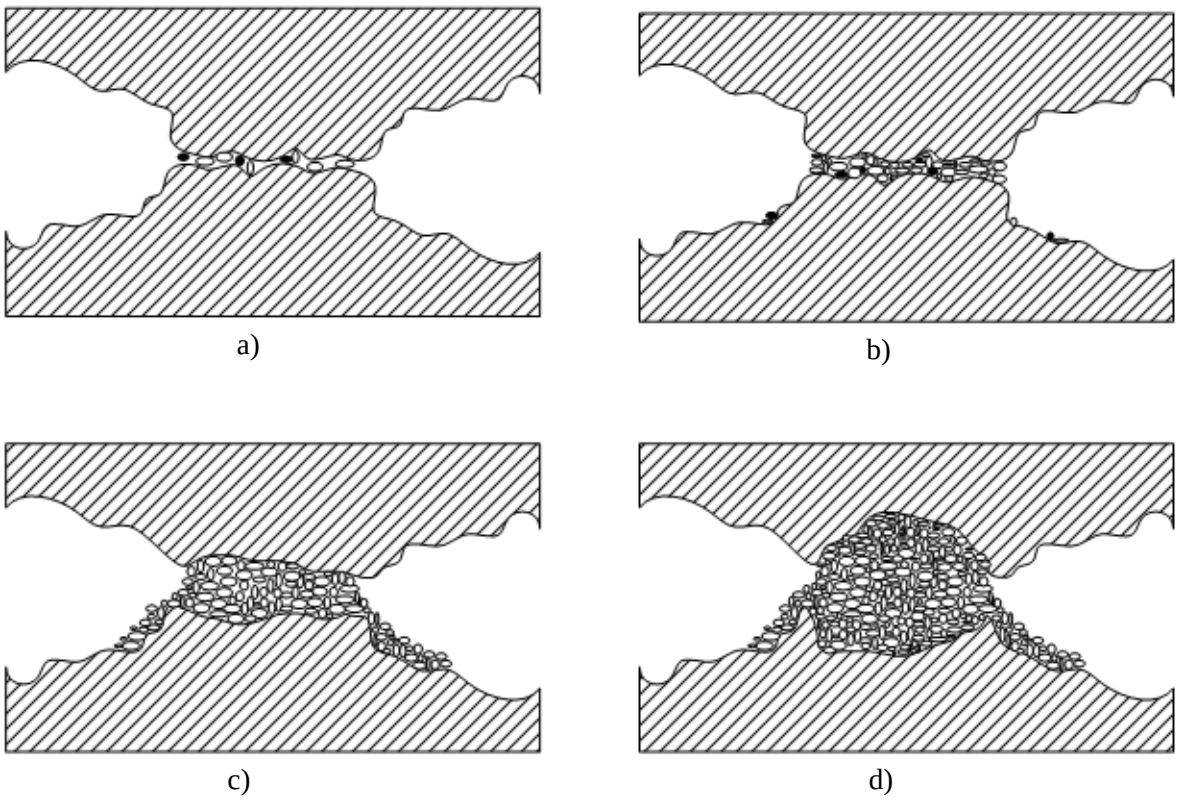

Figure 1.2: Progression of Fretting wear induced damage

Unfortunately the accurate prediction of the fretting wear phenomenon is difficult due to the fact that it strongly depends on the nature of the excitation force and the self induced tribological changes [**4**]. According to Szolwinski [**4**] the complexity of the fretting wear process can be attributed to the following:

- The competition between the wear and fatigue process.

- The presence of sliding and impact motions.
- The friction-induced thermo-mechanical effects resulting from the thermal contact configuration, experienced at the contact interface

The provided 3 step fretting wear mechanism proposed by Waterhouse [**15**] is however not the only explanation of the interactions taking place during fretting wear. The first major contribution to wear investigation in general was made by J.F. Archard in 1953. According to this first wear law the mass of matter detached from a body (*dW)*, per unit time (*dt*), is directly proportional to the product of the applied pressure (*P*) and the sliding speed (*V*) at the contact interface[**14**]. This relation is provided in Equation 1-1.

$$\frac{dW}{dt} = KPV \qquad \text{Equation 1-1}$$

Equality for this relation is given by a "wear coefficient" denoted *K*. For more than fifty years after Archard first proposed this wear law, numerous wear laws have been derived. These wear laws consist of more than a hundred parameters and most of these parameters are derived from Archard's law [**14**]. It is important to note that most of these laws are only applicable for the set of experimental conditions for which they have been established. One of the main differences between fretting and reciprocating sliding wear is the distribution of the wear debris. In the case of reciprocating sliding wear the wear debris are swept out of the wear track and pile up at the ends of the wear track, causing a relatively small amount of debris to interact within the wear track [**16**]. During fretting the wear debris have trouble escaping from the contact interface and become trapped due to the nature of the fretting mechanism as depicted in Figure 1.2. Thus for fretting wear most of the wear debris can only be found by stopping the fretting mechanism and opening the contact. For this reason a wear approach, known as "three body wear" is also used in order to explain the fretting wear phenomenon.

M. Godet was the first to propose the now well known wear concept, the third body approach, during the 1970's [**14**]. In lubricated conditions the third body is injected into the interface in order to lubricate the contact and reduce the wear. During dry conditions the third body consists of the particles detached from the two surfaces of the original contact, acting as dry lubricant. According to Godet [**17**] the third body performs the following three functions:

- Supports the load
- Accommodates the relative velocity experienced at the contact interface
- Protects the surfaces involved by separation, avoiding direct interaction between the original surfaces

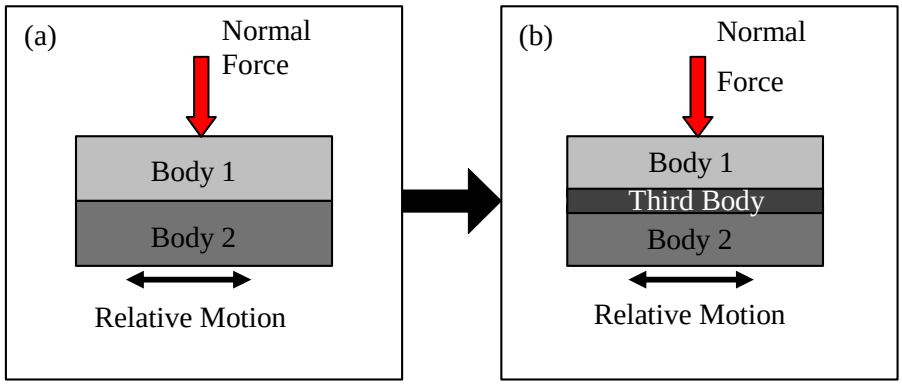

Figure 1.3: progression from conventional two body wear (a) to three body wear (b)

Figure 1.3 provides a simplified schematic of the transition from conventional two body wear to three body wear, introduced by Godet. The presence of the third body causes the two original bodies to no longer be subjected to all the stresses and displacements imposed by the wear mechanism [**14**]. The third body is thus a protective layer, counteracting the surface degradation imposed on the original two bodies. Using the third body approach, the following definition of wear is provided by Fillot et al. [**14**]:

> *"Wear is not only a particle detachement process, but the process in which particles are detached from solids in contact, how they act inside the contact as the third body, and finally how they are removed from the contact."*

During an effort to model this wear phenomenon, Yves Berthier [**18**] developed the simplified tribological circuit provided in Figure 1.4.

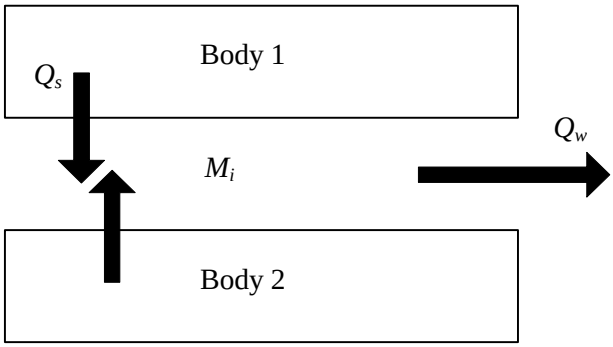

Figure 1.4: Simplified tribological circuit of three body wear [**18**]

The interface between body 1 and body 2 contains a mass of third body material, denoted M_i. The particles that detach from body 1 and body 2 are represented by the source flow (Q_s), while the particles ejected from the interface are represented by the wear flow (Q_w). These parameters were then used to construct the following mass equilibrium equation for the contact interface [**14**]:

$$\frac{dM_i}{dt} = Q_s - Q_w \qquad \text{Equation 1-2}$$

The source flow and wear flow does not directly influence oneanother, but rather modifies the mass of third body particles at the interface. In order to beter understand this interaction refer to the flow diagram in Figure 1.5.

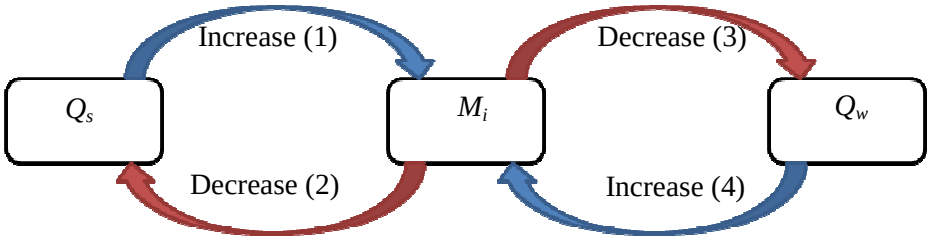

Figure 1.5: Diagram of three body wear interaction

An increase in the source flow (1) will result in an increase in the third body mass. This increase in the third body material layer will ultimately result in a decrease in particle detachment, and consequently a decrease in the source flow (2), in an attempt to establish mass equilibrium. At the same time an increase in the third body material layer will also give rise to the activation of the particle ejection process (3). The ejection of particles from the contact interface results in the decrease of the third body mass. This will ultimately cause the particle ejection process to slow down in order to once again increase the third body mass (4), in an effort to establish mass equilibrium [**14**].

The fretting process is also strongly affected by environmental conditions, in particular atmospheric oxygen and water. According to R.C. Bill [**19**] fretting wear is accentuated in the presence of water and oxygen. It was also discovered the certain inert atmospheres such as nitrogen and argon will suppress the fretting process [**20**]. During a study conducted by Fenner [**21**] it was found that the oxide debris produced during fretting wear experiments, conducted in oxygen, caused a rise in the electrical resistance of the produced oxide layer. When the same experiment was conducted in a nitrogen atmosphere, the resistance remained low until oxygen was introduced, causing a rise in the resistance. In the presence of oxygen the fretting wear process is a combination of abrasive, adhesive and corrosive mechanisms. The fretting wear process is however very different in the absence of oxygen, causing the adhesion mechanism to dominate, because there is no intervening oxide layer to separate the original contact surfaces [**15**]. This will consequently result in a dramatic rise in the coefficient of friction at the contact interface.

It is believed that a change in temperature can affect the fretting process in two ways. Firstly an increase in temperature will cause the rate of oxidation taking place at the contact interface to increase. Secondly a change in the temperature will affect the material properties of the surfaces involved. According to Bill [**22**] fretting wear rates will usually decrease with an increase in temperature. The reason for this is that a rise in temperature will cause a rise in the rate of contact surface oxidation, forming a thick, stable and mechanically strong oxide layer between the contact surfaces. This oxide layer then acts as solid lubricant at the contact interface, preventing direct metal-on- metal contact and reducing the coefficient of friction,

ultimately resulting in less surface damage [**6**]. The oxide layers that form during the fretting process also vary in thickness and are formed at different temperatures, depending on the materials involved [**23**]. A decrease in temperature on the other hand will usually result in an increase in fretting damage [**20**].

In 1985 R.B. Waterhouse [**24**] believed that fretting damage could not be prevented by liquid lubricant, because of the very low sliding speeds associated with the fretting process. A study conducted by Neyman [**25**] however revealed that commercial oils demonstrated large reductions in the fretting wear volume for experiments conducted on dry and lubricated steel surfaces, subjected to fretting conditions. In another study conducted by Qiu [**26**] it was found that simple mineral oil can be effective in reducing fretting wear and friction. Studies also revealed that solid graphite based lubricants are also effective in reducing the effects of fretting [**27**]. In terms fretting wear the function of lubrications are to suppress adhesive and corrosive wear at the contact interface, allowing wear to take place by fatigue-base delamination wear mechanisms [**25**].

A study conducted on several alloyed steel surfaces also revealed that the level of fretting experienced by a contact is not directly related to the hardness of the materials involved [**28**]. In a similar study published within the same year, by some of the same authors, it was revealed that instead of hardness certain properties related to the microstructure of materials have a strong controlling influence on fretting wear rates [**29**]. It is also known that a high degree of surface finish accelerates fretting, resulting in rough surfaces to be preferred for applications known to be prone to fretting induced damage [**30**].

1.4 Fretting Fatigue

Fretting fatigue is a fatigue life reduction phenomenon, resulting from fretting induced actions. Stachowiak [**6**] provided the following definition for this complex phenomenon:

> *"Fretting fatigue is a phenomenon where the surface of a component subjected to alternating bulk stresses is also fretted, resulting in a severe reduction in fatigue life."*

Even though fretting fatigue results in alternating surface stresses on the surfaces of materials, the most important aspect of this phenomenon is the generation of surface micro cracks, as a result of asperity contact. Figure 1.6 provides a schematic representation of surface micro cracks, resulting from fretting actions.

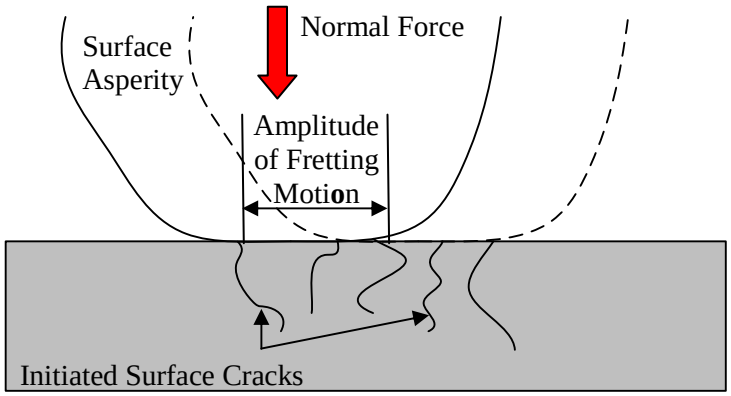

Figure 1.6: Mechanism of surface micro crack initiation generated by fretting [**6**]

According to Bill [**22**] the number of initiated micro cracks will increase with an increase in fretting/slip amplitude. This happens because the tensile surface stresses adjacent to the micro cracks relaxes, forcing the contacting asperity to move a distance that is large compared to the instantaneous crack length in order to initiate another surface crack. According to Collins [**3**] the premature fatigue nuclei generated during fretting fatigue may be caused by any of the following four mechanisms:

- *Abrasive pit-digging action*: This action produces elongated grooves at the fretting interface by abrasive debris and asperities moving under the influence of the oscillatory relative motion. The result of the action is a pattern of tiny elongated grooves in the fretted region. The mechanism and results of the abrasive pit-digging action are illustrated in Figure 1.7. From the figure it is evident that the axes of the tiny elongated grooves are all approximately parallel to one another and in the direction of the fretting motion.

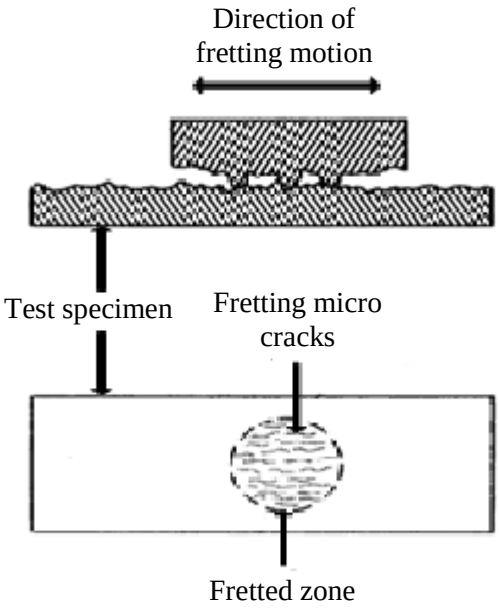

Figure 1.7: Illustration of the stress concentrations and micro-cracks produced by the abrasive pit-digging action [**3**]

- *Asperity-contact micro-crack initiation:* This phenomenon is caused by the contact force resulting between the tip of an asperity on one surface and another asperity on the mating surface as they move back and forth. The result of this phenomenon is repeated contact between the asperity tips, causing cyclic or fatigue stresses in the region of the base of each asperity. It is also possible that the initial contact between the asperity tips will shear off one of the asperities from its base. It is also a distinct possibility that the previously mentioned cyclic or fatigue stresses may give rise to the nucleation of fatigue micro-cracks at the base of each asperity. According to Collins [**3**], the expected result of this mechanism is an array of micro-cracks whose longitudinal axes would generally be perpendicular to the direction of the fretting action.
- *Friction-generated Cyclic Stresses*: When two members undergo fretting motion a compressive stress component is produced in the volume of material that lies ahead of the fretting motion. A tensile stress component in the volume of material that lies behind the fretting motion is also produced. Collins [**3**] further explains that the cause of these stress components is the traction induced friction force between the two members in question. The result of this mechanism is that the volume of material adjacent to each contact zone is subjected to a cyclic stress that contributes to the generation of a field of micro-cracks at these sites. Figure 1.8 provides an illustration of the mechanism and results of the friction-generated cyclic stress mechanism. The direction of the longitudinal axes of friction induced micro-cracks is perpendicular the fretting direction, as shown in the figure.

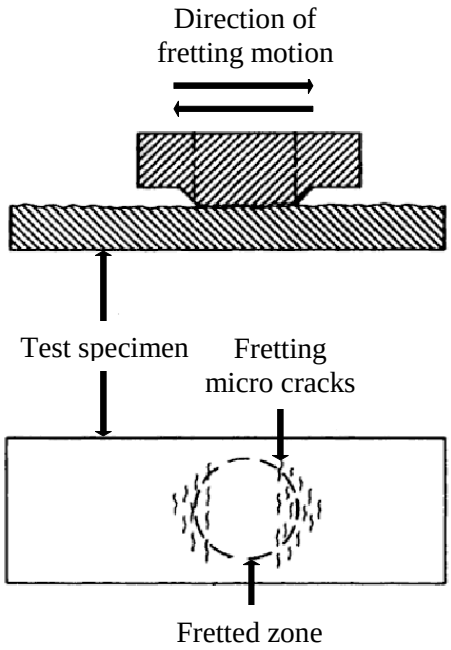

Figure 1.8: Illustration of the stress concentrations and micro-cracks produced by the friction-generated cyclic stress mechanism [**3**]

- *Surface-generated cyclic stresses*: The combination of the normal and traction induced tangential forces, produced at the asperity contact sites of the fretting interface is responsible for a complex multi-axial state of stress. This state of stress is also accompanied by a cyclic deformation field [**3**]. The result of this phenomenon is a subsurface peak shearing stress as well as subsurface crack nucleation sites. The resulting micro-cracks grow parallel to the surfaces at the fretting interface and finally propagate to the surface. A thin sheet of material is thus produced, which eventually separates from the rest of the member in order to form a particle of debris.

Fretting fatigue not only accelerates the initiation of fatigue cracks, but also accelerates the growth of these cracks. One of the main differences between fretting fatigue and fretting wear is that the amplitude of the fretting motion (slip amplitude), resulting in fretting fatigue is much smaller than that of fretting wear [**6**]. According to Waterhouse [**15**] small slip amplitudes result in the formation of strong adhesive bonds between contacting asperities. These adhesive bonds will ultimately produce small fatigue cracks instead of producing wear particles, since the asperities never move far from one another other. Nishoika[**31**] developed the following expression in order to estimate the reduction in the fatigue strength of a component due to fretting:

$$S_{fr} = S_o - 2\mu p_o[1 - e^{(-1/k)}] \qquad \text{Equation 1- 3}$$

During the same study, Nishoika [**31**] also discovered that the abrasive actions resulting from relatively large slip amplitudes during the fretting phenomenon will increase the stress needed in order to initiate fatigue cracks. The reason for this is that the abrasive actions wear away the fatigue cracks at the surface, once initiated. Normally, a certain amount of fretting wear will take place during the initial stages of fretting fatigue. The subsequent fatigue cracks that result from the initial fretting wear process will propagate and eventually lead to the fretting fatigue failure of the component.

1.5 Fretting Regimes

As mention in Section 1.2 fretting wear is sometimes considered to be a special type of reciprocating sliding wear that takes place at very small relative displacements. However, there are enough significant differences in the mechanisms and wear rates involved to warrant the distinction [**16**]. The term fretting regime refers to the category into which any fretting contact is categorized, according to the response of the fretting contact. According to Vingsbo [**32**] there are three main fretting regimes, strongly dependent on the amplitude of relative displacement (slip amplitude). These three regimes, including reciprocating sliding wear are shown in the generalized fretting map depicted in Figure 1.9. Unfortunately the transition values of the different regimes are not known, because these values differ for all types of fretting contacts. According to

Dobromirski [**33**] there might be fifty variables capable of affecting the fretting process and most of these variables are capable of affecting the transition values of the fretting regimes. It is thus impossible to know exactly what combination of normal force and slip amplitude will result in particular fretting regime. Therefore preliminary experimental results are results are used to establish the required normal force and slip amplitude needed to produce a particular fretting regime.

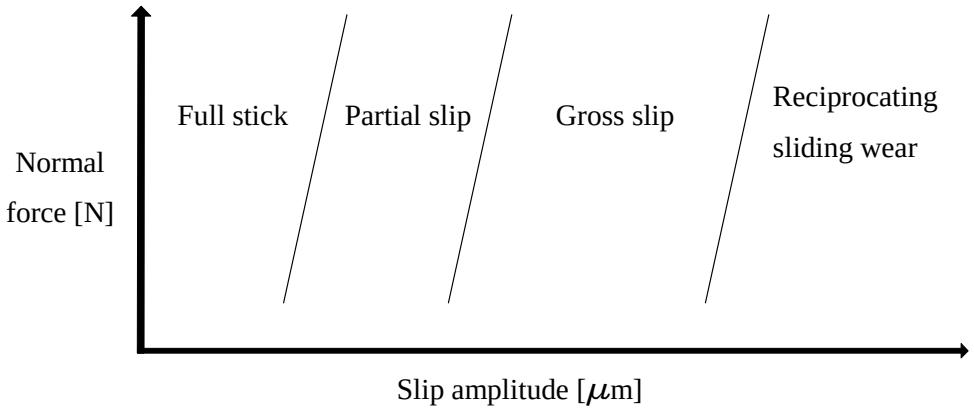

Figure 1.9: Generalized Fretting Map: Normal force versus Slip amplitude

During the ball-on-flat fretting study conducted by Vingsbo [**32**] a variety of fretting experiments were conducted on several material specimens in order to investigate the three fretting regimes. This study forms the basis for the following discussion on these three main fretting regimes.

1.5.1 Full Stick

The first group of fretting experiments was conducted on niobium, at extremely low displacement values. The results of this experiment are provided in Figure 1.10. The micrograph images reveal a wear scar with various individual asperity contacts, including large areas of unaffected material in between. From the images it is also not possible to identify the direction of the fretting motion. According to the authors the linear T-d relation, provided Figure 1.10(a), suggests that the displacement between the contacting surfaces is the result of elastic deformation. During the full stick regime adhesion between contacting asperities dominates, resulting in the plastic shearing of these individual asperities as shown in Figure 1.10(c).

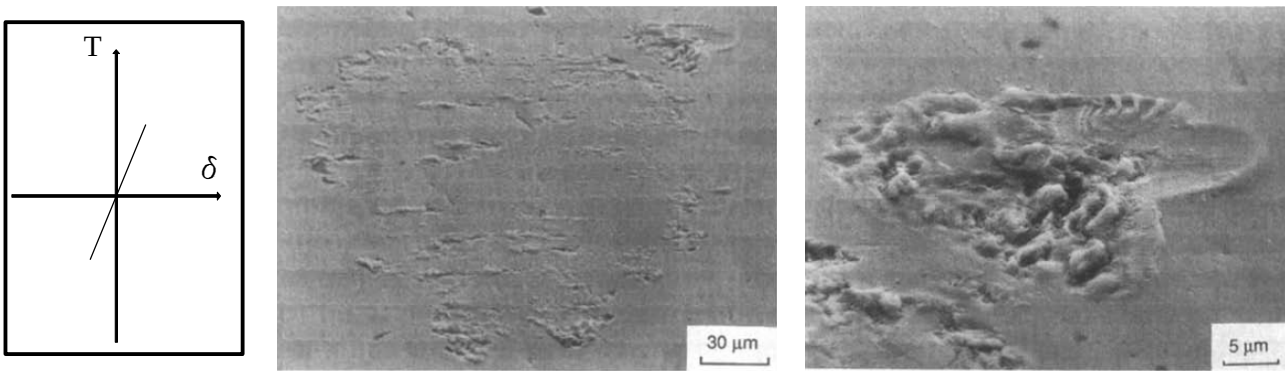

(a) (b) (c)

Figure 1.10: Example a typical recording of tangential force versus displacement amplitude in the full stick fretting regime; b) fretting wear scar of niobium in the full stick fretting regime; c) wear scar in detail [**32**]

From Figure 1.10(c) it is also evident that no shear fracture of the asperities took place, ruling out the possibility of fretting wear [**32**]. The micrograph images do also not reveal any distinct evidence of fatigue or fatigue crack nucleation. It is however important to note that the experiment was not conducted for more than 10^6 cycles. Even though no evidence of fretting fatigue was found, it is believed to occur during the full stick regime [**32**].

1.5.2 Partial/Mixed Slip

The partial/mixed slip regime is the most complex of all the fretting regimes. The reason for this is that it involves surface adhesion, resulting in a mixture of slip and stick taking place throughout the wear track [**16**]. Mindlin [**34**] was the first to discuss the mechanism of partial/mixed slip. This mechanism is described using the contact interface provided in Figure 1.11.

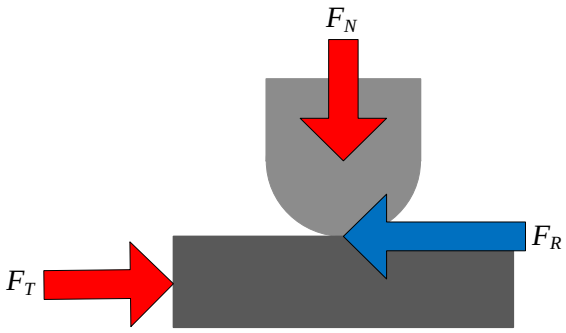

Figure 1.11 Partial slip contact interface

The force resisting motion at the contact interface (F_R) is a function of the normal load (F_N) and the friction coefficient (μ). This resisting force is known as the friction force of the contact interface and is determined using Equation 1-4.

$$F_R = \mu F_N \qquad \text{Equation 1- 4}$$

In order to induce relative tangential motion at the contact interface, the tangential excitation force (F_T) must overcome the fictional force, resulting from the elastic limits of the materials in contact [**34**]. Figure 1.12 provides the pressure distribution of a typical Hertzian contact subjected to partial/mixed slip conditions. This Hertzian contact can consist of a flat material in contact with a ball, a cylinder or an ellipsoid [**16**].

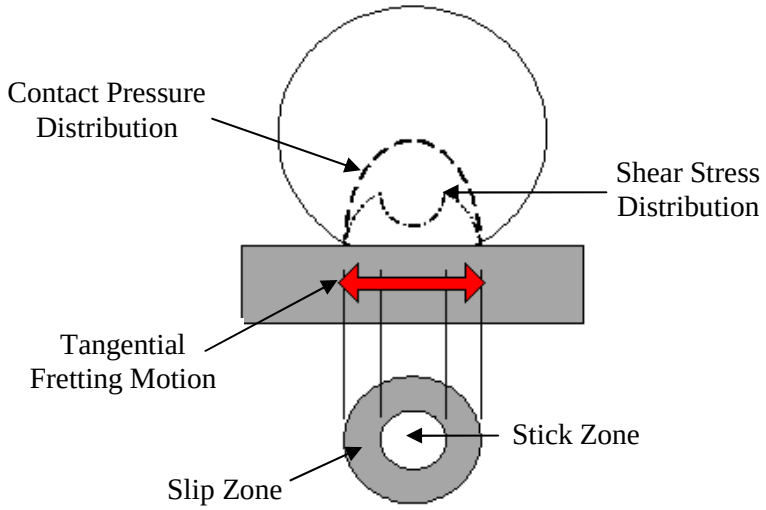

Figure 1.12: Pressure distribution of a typical Hertzian contact subjected to partial/mixed slip

During the second part of the study conducted by Vingsbo [**32**], niobium experienced partial/mixed slip. The results of this part of the investigation are provided in Figure 1.13. The T-δ curve provided in Figure 1.13(a), indicates the traditional transition from elastic to plastic shear. This represents the plastic yield of the asperities as well as the underlying bulk material [**32**]. The T1 and $\delta 1$ values in the figure represent the critical tangential force and slip for the transition from the full stick regime to the partial/mixed slip regime. At these critical values, the applied shear stress is relaxed and slip is introduced [**32**].

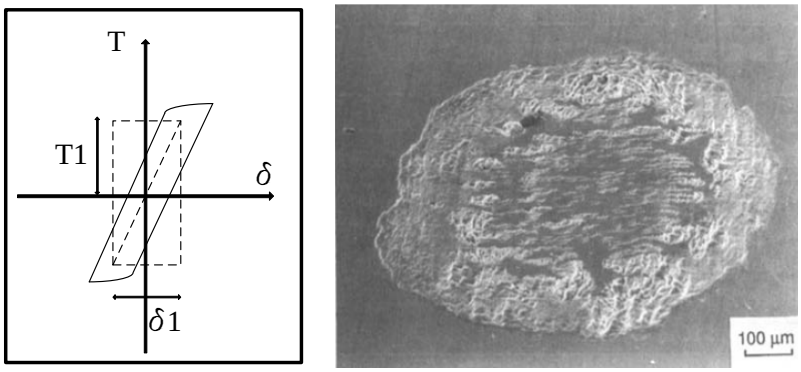

(a) (b)

Figure 1.13: (a)Example a typical recording of tangential force versus displacement amplitude in the full stick fretting regime; (b) fretting wear scar of niobium in the partial/mixed slip fretting regime [**32**]

From Figure 1.13(b) the full stick zone is clearly visible in the middle of the wear scar, with the annular slip zone surrounding it. The surface damage in the full stick zone is similar that of the full stick fretting regime discussed in Section 1.5.1. Surface cracks are also visible at the boundary between the full stick zone and the slip zone. According to the authors this is the region where the highest stresses were generated [**32**]. The slip zone is characterized by severe surface damaged, with small grooves at the edge of the wear scar. This type of wear scar topography is indicative of abrasive wear, caused by wear debris.

1.5.3 Gross Slip

During the final part of the study Vingsbo [**32**] investigated the gross slip fretting regime for AISI 1018 steel. The results of this part of their study are provided in Figure 1.14. According to the authors the sudden drop in the T-d curve, provided in Figure 1.14(a), corresponds to the transition from static to kinetic friction. This is also the transition point to gross slip, resulting in all asperity contacts being broken for every cycle. The micrograph image of the wear scar, provided in Figure 1.14(b), clearly indicates small sliding wear marks in the direction of the induced fretting motion. The detailed image of the wear scar, provided in Figure 1.14(c), provides evidence of severe plastic shearing [**32**].

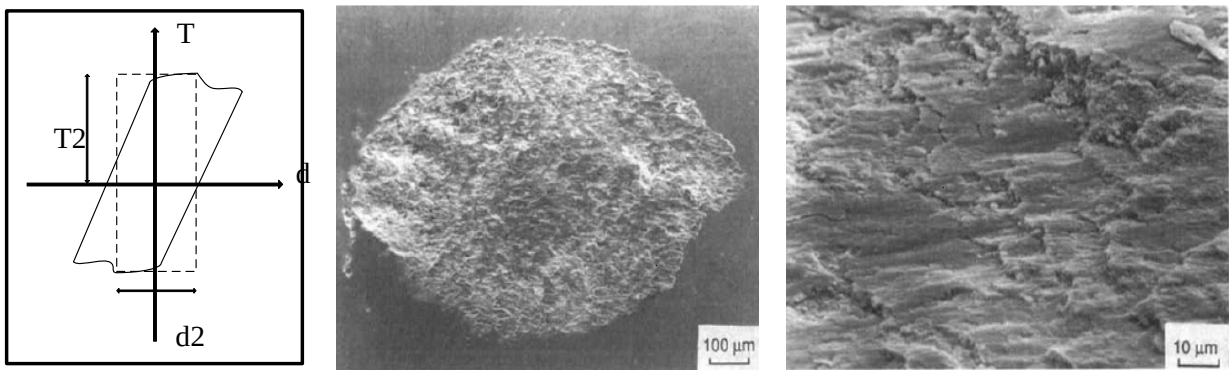

(a) (b) (c)

Figure 1.14(a) Example a typical recording of tangential force versus displacement amplitude in the full stick fretting regime; (b) fretting wear scar of niobium in the partial/mixed slip fretting regime; c) wear scar in detail [**32**]

1.5.4 Reciprocating Sliding Wear

There are several techniques to determine the transition between fretting wear and reciprocation sliding wear. According to a study conducted by Chen [**35**], investigating the volumetric wear rate provides the best method for defining the transition between fretting wear and reciprocating sliding wear. One of the main defining characteristics of reciprocating sliding wear is that the wear volume stays almost constant for different displacement amplitudes, as long as the total sliding distance is kept constant [**36**]. Accordingly the wear coefficients resulting from reciprocating sliding wear will become approximately constant [**32**]. If the

displacement amplitude is reduced below a critical value the volumetric wear rate will decrease proportional to the displacement amplitude [**35**]. This critical value represents the transition point between reciprocating sliding wear and fretting wear, for the specified loading conditions. According to Hager [**16**] the main reason for the occurrence of the transition from fretting wear to reciprocating sliding wear is the change in the surface interactions and debris formation. The debris created through reciprocating sliding wear are swept out of the wear track and pile up at the ends of the wear track, resulting in a relatively small amount of debris that are able to interact with the wear track [**16**].

2 Fretting in Aerospace Applications, a Motivation

2.1 Fretting in Aircraft Turbo Machinery

According to the definition, turbo machinery is a group of machines that exchange energy with a fluid called the working fluid, through shaft rotation. Turbo machinery is a very important part of all gas turbine engines currently in use in the aircraft industry [**37**]. There are basically three distinct groups of turbo machinery in practise. In the first group of machines the fluid path is along the axis of shaft rotation. These machines are called axial-flow turbo machinery [**37**]. In the second group the fluid undergoes a 90° change in angle relative to the axial direction. These machines are known as radial-flow turbo machinery or centrifugal machines [**37**]. The third group is a hybrid of the first two and are known as mixed-flow turbo machinery. Axial-flow compressors and turbines are most widely used in aircraft gas turbine engines. Figure 2.1 provides a simplified schematic of a gas turbine engine, depicting the four main functions performed by the engine.

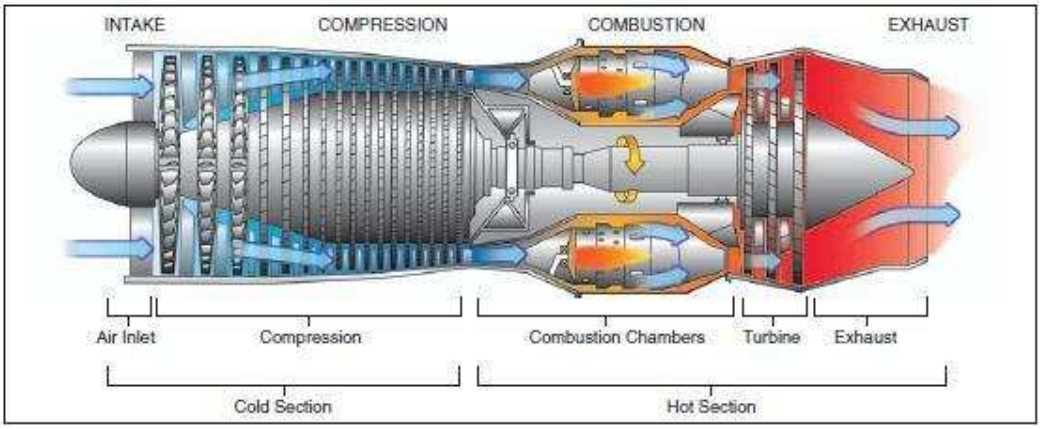

Figure 2.1: Gas turbine engine

Aircraft gas turbine engines operate in extreme and aggressive environments, subjecting the engine components to extreme temperatures and unwanted vibrations [**38**]. However, the competitive nature of the aircraft industry forces the aircraft engine manufacturers to continuously push the envelope in terms of higher thrust and lower fuel consumption. In order for this continuous growth in gas turbine engine technology to be sustainable, each stage in the aircraft engine is required to operate at higher speeds and subsequently higher loads without compromising safety.

Fretting is unfortunately a major problem facing the aircraft industry in terms of reliability, maintenance and consequently safety [**39**]. Fretting in the aircraft industry is so problematic that it often leads to catastrophic failures. According to Mc Veigh [**40**] around one sixth of all in-service high-cycle fatigue problems experienced in United States Air Force engine hardware can be attributed to fretting-induced damage. The

blade and disk connections in turbine engines are common locations for fretting damage to occur [**41**]. Dovetail joints and fir tree joints are the two most popular blade/disk connections in gas turbine engines [**39**]. The rotating disk combined with the air flow through the turbine engine imposes centrifugal forces and slight radial oscillations on the dovetail and fir tree joints. Even though the induced turbine engine vibrations and loading regimes are very complex to explain, authors model these phenomena as a combination of low-frequency high-amplitude cycles and high-frequency low-amplitude cycles [**42**]. The low-frequency high-amplitude cycles are believed to be as a result of the takeoff, landing and major power excursions, while the high-frequency low-amplitude cycles are believed to be caused by in-flight vibrations.

Many authors believe that the fretting damage most often experienced at these interface are attributed to the partial slip fretting regime [**40**], causing a limited amount of interfacial wear. The partial slip will cause localized contact stresses, accelerating the nucleation of fatigue cracks in the near surface material of the affected components. This is however not always the case. According to Hutson [**43**] in-service fretting regimes may overlap, causing the damage resulting from one regime to be obscured by another regime. A study conducted by Fouvry [**44**] revealed that dovetail contacts are subjected to gross and partial slip conditions, causing both wear and crack nucleation to occur. This makes it difficult to identify the in-service transition from one fretting regime to another. The problem is even further worsened by the difficulty involved in detecting fretting fatigue cracks during service. According to Nicholas [**45**] fretting in dovetail joints are recognized as one of the costliest in-service high cycle fatigue damage encountered by the United States Air Force.

As mentioned, dovetail and fir tree joints are some of the most common fretting sites in gas turbine engines. Fir tree joints are preferred for turbines, while dovetail joints are preferred for compressors. Figure 2.2 provide photographs of a typical dovetail- and fir tree joint.

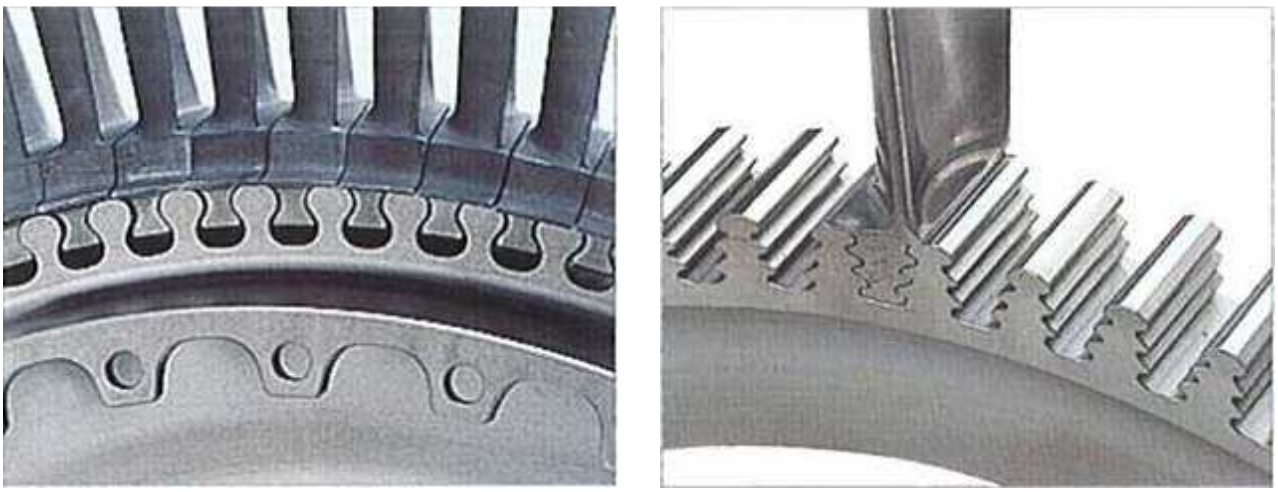

(a) (a)

Figure 2.2: Aircraft engine blade-disk joint – a) dovetail joint; b) fir tree joint

According to Birch [**46**] the two primary blade materials used in the gas turbine engines of military aircraft are titanium based alloys and nickel based super alloys. The nickel based super alloys are usually found in the later, high temperature stages of the turbine engine, because of their suitable strength at high temperatures. Titanium alloys are preferred in the earlier part of turbine engines where the ambient air temperature is not that high, because of the high strength to weight ratio exhibited by these materials. The alpha/beta titanium alloy Ti-6Al-4V is used in a variety of aeronautical applications, with dovetail and fir tree joints being two of the best know of these applications [**41**]. The high strength to weight ratio as well as the corrosion resistance of Ti-6Al-4V is the major reason why this material is used to fabricate dovetail and fir tree joints [**47**]. The material also displays good biocompatibility, making it a very attractive option for prosthetic implants. Unfortunately the material is expensive and exhibits poor tribological properties. It has also been observed that Ti-6Al-4V is very susceptible to damage caused by small alternating sliding conditions, also known as fretting conditions [**41**]. The reason for this is that Ti-6Al-4V is extremely susceptible to wear phenomenon known as galling and produces hard oxide debris that damages the surfaces of the material [**48**].

2.2 Fretting in Aircraft Structural Members

Aircraft structures consist of large variety of mechanical connections and assemblies. Many of these mechanical assemblies consist of contacting components which are nominally fixed with respect to one another. This is unfortunately not always the case. In reality these connections can experience slip as a result of loads imposed across their contact interface [**49**]. This is especially true for aircraft structural connections, because of the harsh operation environments of these connections.

The airframe materials for most commercial and military aircraft manufactured during the 20th century were selected for approximate design lives of 20 to 30 years [**7**]. Global competition and increasing economic constraints have however forced military and commercial aircraft operators to extend the live times of their aircraft. According to Krishnakumar [**7**] the traditional method of aircraft construction involves the use of at least 10000 fasteners, with each of these fastener holes being a potential localized stress concentration point. Therefore each of fastener holes is a potential site for fatigue crack initiation. Thus, in addition to the problem facing aircraft gas turbine engines, fretting is also a major concern in bolted and riveted aircraft structures [**50**]. Most authors also believe that the fretting phenomenon encountered in these contacts is caused by extremely small vibrations and variations in load, resulting in fretting fatigue [**46**].

The operating temperatures in which these bolted and riveted connections are found is often well below -50°C. Consequently one of the most commonly used materials in aircraft structures is the heat treated aluminium alloy known as Al7075-T6. This alloy exhibits a low-specific weight and high strength to weight ratio, as well as high electrical and thermal conductance. During a study conducted by Krishnakumar [**7**] the

fatigue behaviour of Al7075 bolted joints were investigated. The results of the study revealed that fretting played a major role in the fatigue failure of the test specimens. Figure 2.3 provides two images of fatigue failure that occurred during this study, as result of fretting damage. The white arrow in Figure 2.3(b) reveals a surface flaw resulting from fretting.

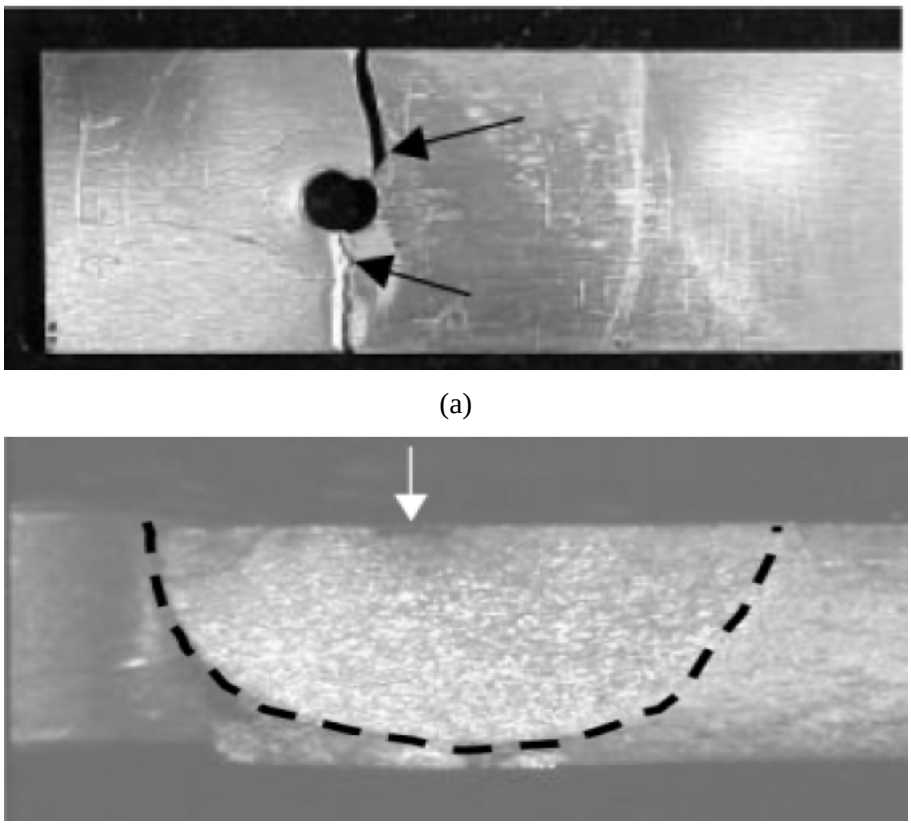

(a)

(b)

Figure 2.3: Experimental fatigue results of Al 7075 bolted joints [**7**]

3 Project Motivation, Scope and Key Questions

3.1 Motivation

Numerous authors have investigated the effects of fretting fatigue on aerospace applications involving Ti-6Al-4V and Al 7075-T6 and their findings have been well documented. Not many authors have investigated the fretting wear of Ti-6Al-4V and Al 7075-T6 in regard to the discussed aerospace applications. According to Paulin et al. [**51**] fretting wear and fatigue mechanisms interact. During an investigation conducted by Fouvry et al. [**52**] it was found that wear damage activated under gross slip conditions can limit fatigue damage by progressively eliminating surface cracks at a faster rate than their growth. Conversely, wear can critically modify the interface geometry of fretting contact interfaces, leading to local over-stressing and can favour cracking phenomena [**4**]. Unfortunately the interaction of fretting wear and fatigue mechanism are extremely complex. Therefore in order to better understand the fretting problem experienced in the aerospace applications discussed in Chapter 2, it is necessary to investigate the fretting wear mechanism taking place at theses contact interfaces.

3.2 Project Scope

This project is aimed at the investigation of the fretting wear phenomenon commonly encountered at two key aircraft contact interfaces, using an in-house developed fretting test apparatus.

3.3 Key Questions

The five key questions derived from the project scope are as follows:

- Is the developed fretting wear test apparatus capable of producing controllable fretting wear conditions?
- Is the fretting test apparatus capable of recreating the actual contact configurations encountered at the two key aircraft contact interfaces?
- What is the effect of the normal force on the fretting wear of the two aircraft alloys encountered at the two key contact interfaces?
- What is the effect of conventionally sintered cemented tungsten carbide on the fretting wear encountered at these interfaces?
- What is the effect of spark plasma sintered cemented tungsten carbide on the fretting wear encountered at these interfaces?

4 Design, Construction and Calibration of a Fretting Test Apparatus

Nomenclature

Symbol	Description	Units
F	Friction force	N
N	Normal force	N
μ	Coefficient of friction	none
μ_d	Coefficient of dynamic friction	none
μ_s	Coefficient of static friction	none
δ	Slip amplitude	μm
n	Data point per fretting cycle	none
c	Cycle number	none
T	Tangential force	N
T_s	Static tangential force per cycle	N
T_d	Dynamic tangential force per cycle	N
N_{avg}	Average normal force per cycle	N

4.1 Introduction

The design, construction and calibration of an entirely new fretting test apparatus formed an intricate part of this study. The most important aspect of any test apparatus or experimental simulator is to replicate the actual scenario and conditions inspected, as closely as possible. Accordingly the most important variables of the scenario in question need to be accurately controlled and monitored. These variables include the normal contact force, tangential contact force, fretting frequency, slip amplitude, environmental conditions and material properties. The test apparatus allows for the accurate control and measurement of these variables, with the exception of the environmental conditions.

The main aim of the design phase of the test apparatus was to keep the entire apparatus as inexpensive as possible, whilst still allowing a large degree of adjustability. The result of this phase is simplistic device providing numerous points of adjustment for alignment and calibration. The device features interchangeable fretting contacts, allowing a variety of fretting contact conditions involving different materials. The chapter thoroughly addresses the theoretical and practical design considerations of the fretting test apparatus. The chapter also discusses the real time data measurement system of the device, including systems developed to

produce data applicable to fretting experimentation. The full capabilities of the fretting test apparatus are thoroughly demonstrated and discussed in Chapter 5.

4.2 Specification Development

The main aim of fretting experimentation is to replicate as closely as possible the actual fretting situation. In most cases it is difficult the reproduce the exact mechanical conditions of the fretting interface in question. Two of the most difficult mechanical conditions to replicate are the loading in the contact and the amplitude of movement [**53**]. The main specifications of fretting testing and test rigs can be divided into the following 4 categories, used to design the fretting test apparatus:

- **Contact configurations:** In most cases the type of test specimen is dictated by the fretting contact configuration to be reproduced by the test apparatus. Historically, the most common of these fretting contacts are cylinder-on-flat and flat-on-flat [**53**]. Another well known fretting contact is the ball/sphere-on-flat. Therefore the fretting test apparatus was designed to reproduce these three fretting contact configurations.
- **Normal force/load**: One of the main research objectives of this study is to investigate the normal force effects on the fretting wear of certain materials. The fretting test apparatus was thus designed to produces a fully adjustable, but controllable normal force at the fretting interface.
- **Fretting frequency**: Fretting experimentation is very time consuming, because most test specimens are required to undergo a large number of fretting cycles. Some scientists have attempted to counteract this problem by altering the slip amplitude. This was however not the best solution, because altering the slip amplitude may also change the fretting mechanism, or result in reciprocating sliding wear. The only other alternative to accelerate fretting experimentation is to increase the fretting frequency [**54**]. Uhlig believed that the oxidation component of fretting is governed by frequency [**55**]. According to this assumption the oxidation component will result in a decrease in the volume of material removed per cycle, caused by an increase in frequency. During a study conducted by Waterhouse it was deduced that the fretting wear rate should only exhibit frequency dependence at low frequencies (less than 17 Hz) [**56**]. It is however important to note that this hypothesis has not been verified by experimental data. During another study conducted by Bryggmann the effect of frequency on the fretting behavior of carbon steel and stainless steel was investigated [**57**]. From the study it as concluded that during low amplitude fretting (corresponding to partial slip conditions), an increase in frequency lead to an increase in the rate of fretting fatigue and fretting corrosion. This is due to the increase in both the temperature and the interfacial strain rate associated with an increase in frequency. Bryggmann also concluded that during high amplitude fretting (corresponding to gross slip conditions), the mechanisms of material removal and wear rates were to a lesser extent affected by the frequency [**57**]. By considering this information a frequency range of 10 – 2000 Hz was chosen for the fretting test apparatus.

- **Slip amplitude:** The amplitude of relative motion (or slip amplitude) at the fretting interface is one of the deciding factors in establishing a particular fretting regime [**35**]. If the slip amplitude is very small it is likely that partial slip and consequently a combination of fretting wear and fretting fatigue will take place. At large slip amplitudes reciprocating sliding wear will take place. It is thus important to have a general idea of what slip amplitude is needed in order to produce a specific fretting regime. Throughout history authors have attempted to find specific slip amplitudes for the transition between fretting to reciprocating sliding wear. This is however a very complicated matter because most fretting experiments are different in terms of experimental variables, material characteristics and environmental conditions. Ohmae [**36**] suggested that the transition takes place at 300 µm. This value was also supported by Vingsbo [**32**]. During a study conducted by L. Toth [**58**] a transition value of 50 µm was suggested. It is important to note that these suggested transition values are peak-to-peak values, thus equalling double the slip amplitudes. This study is however aimed at investigation fretting wear and gross slip is thus the required fretting regime. For this reason a peak-to-peak slip value range of 70 – 100 µm was decided upon for the fretting test apparatus. However, the generation of smaller slip amplitudes should also be possible. This was decided in order to produce a more complete test apparatus, capable of not only producing fretting wear conditions, but also fretting fatigue conditions. For this reason the peak-to-peak slip amplitude range was increased to a range of 5-100 µm.

4.3 Fretting Test Apparatus

A system engineering approach was implemented during the design phase of the fretting test apparatus. Accordingly, the test apparatus represents the system as a whole, and consists of five subsystems. Each of the five subsystems was developed to perform a cardinal function. The five subsystems and their functions are provided in Table 4.4.1.

Table 4.4.1: Functional overview of the subsystems of the fretting test apparatus

Subsystem	**Function**
Structural Subsystem	Provide a solid, but adjustable base structure for the test apparatus.
Actuation Subsystem	Cause controllable vibrations in order to induce the required fretting motion at the fretting contact interface.
Specimen Holder Subsystem	Provide a rigid housing platform for the flat specimens to be tested and also provide a location for the fretting interface.
Force Application Subsystem	Apply an adjustable and controllable normal force at the fretting contact interface.
Measurement Subsystem	Real-time measurement of the fretting variables.

As in most major systems, the test apparatus cannot operate in the absence of one or more of the subsystems. Figure 4.1 provides a system diagram of the fretting test apparatus, depicting the five subsystems as well as the system boundaries of each subsystem. The figure also shows the fretting interface as well as the critical connections between the subsystems, depicted by the numbered arrows. From the figure it is clear that the Structural Subsystem is connected to all the other subsystems of the test apparatus. As mentioned in Table 4.4.1, the Structural Subsystem is responsible for providing a rigid, but fully adjustable base for the entire test apparatus, and thus provides the primary connection points for all the other subsystems. The Specimen Holder Subsystem is responsible for providing a platform for the flat test specimens to be tested. This means that during operation the fretting interface is located within the Specimen Holder Subsystem, making it the centre point of the test apparatus.

The Actuation Subsystem is connected between the Structural Subsystem and the Specimen Holder Subsystem in order to create the fretting motion. This motion is translated to the fretting interface via the Specimen Holder Subsystem. The Force Application Subsystem is also connected to the Structural Subsystem and houses the second test specimen, in order to complete the fretting interface. It is important to note that the Force Application Subsystem is not directly connected to the Specimen Holder Subsystem. It is however connected to one half of the fretting interface, similar to the Specimen Holder Subsystem.

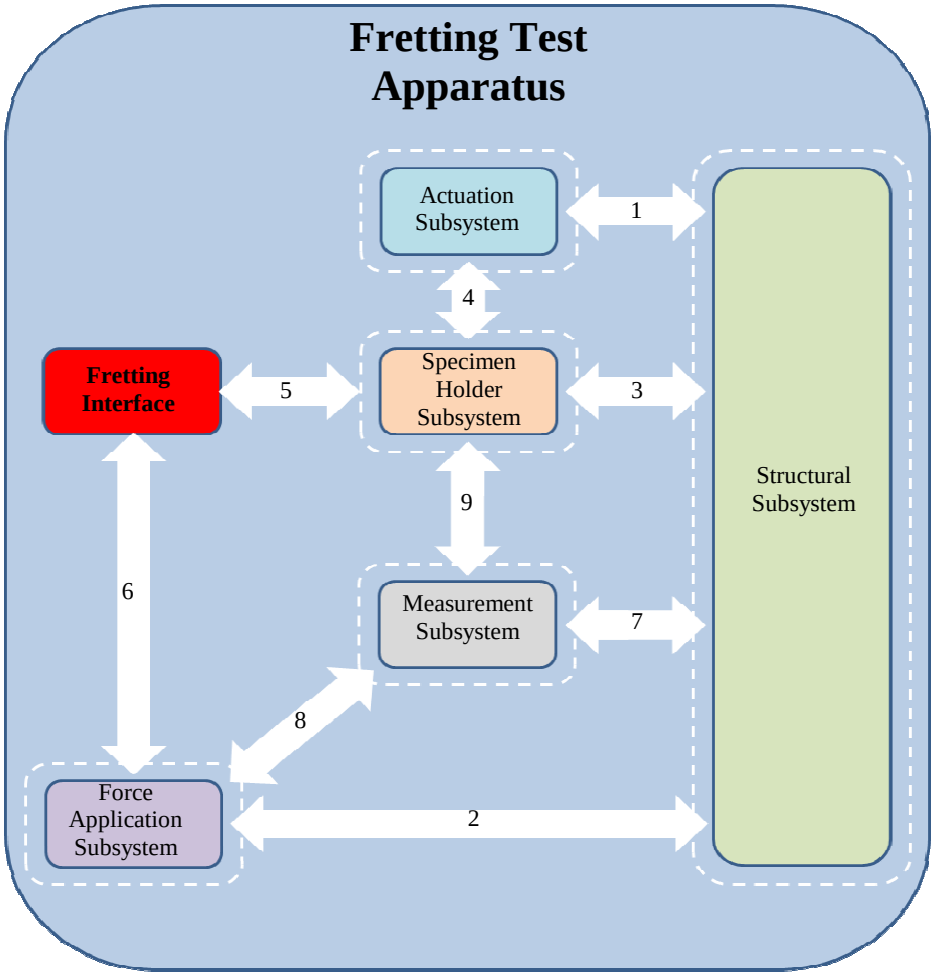

Figure 4.1: System diagram of the fretting test apparatus

The Measurement Subsystem, responsible for the real-time measurement of the fretting variables is connected to the Specimen Holder Subsystem, Structural Subsystem and the Force Application Subsystem. All the connections and subsystem depicted in Figure 4.1 are discussed in the rest of this chapter.

4.3.1 Actuation Subsystem

During the concept evaluation phase of the project several actuation methods were considered. The three main methods evaluated were:

- *Mechanical actuation*: Most of the earlier fretting test setups were driven by methods of mechanical actuation. These setups were usually made up of one or more motors, driving a series of linkages. Precise control is however problem when considering mechanical actuation. The reason for this is that even though the rotation motion provided by the motor can be precisely controlled, the resulting fretting motions created are dependent on the linkages involved. Extremely accurate and expensive tolerances are required in order to produce the micro meter fretting displacement needed, using linkages. Another possible problem might be the fretting actually taking place between the components of the mechanical actuation system, because all the components of the system will be in constant relative motion in relation to one another. For these reasons mechanical actuation was ruled out.

- *Electrodynamic actuation*: Most electrodynamic actuation methods include using an elsctrodynamic shaker module. These models are however usually very large and extremely expensive machines. Producing the specified fretting displacement range at the specified frequency range using electrodynamic actuation is also virtually impossible. For these reasons elctrodynamic actuation was also ruled out.

- *Piezoelectric actuation*: Piezoelectric actuators utilize natural or man-made crystals in order create displacements. These actuators are capable of producing sub micrometer displacements at extremely high frequencies. After evaluating several piezoelectric actuation possibilities it was concluded that a piezoelectric actuator would indeed be capable of producing the specified fretting displacement range at the specified fretting frequency. For these reasons it was decided to use a piezoelectric actuator as the driving force for the Actuation Subsystem.

In 1880 Jacques and Pierre Currie discovered the following two characteristics [**59**]:

1. *When certain crystals are subjected to mechanical forces these crystals are electrically charged. The tension and compression generated voltages were of opposite polarity and these voltages were also proportional to the applied forces.*

2. *When the same crystals were exposed to an electric field they experienced an elastic strain, and lengthened or shortened according to the polarity of the electrical field, and in proportion to the strength of the field.*

These two extraordinary behaviors were respectively labeled the piezoelectric effect and the inverse piezoelectric effect. The piezoelectric effect is currently being used in sensing equipment for measuring a variety of physical variables including accelerometers, force transducers and displacement transducers. The inverse piezoelectric effect is currently being utilized in precision motion and positioning applications as well as in medical instrumentation. Quartz and tourmaline were originally used as piezoelectric materials, but since the mid 1960's man-made piezoelectric ceramics were prepared using metallic oxides [**59**].

The piezoelectric actuation system chosen was supplied by the German based company PI (Physik Instrumente), an industry leader in piezoelectric technology. The piezoelectric actuator is called the PI P-842.60 Preloaded Piezo Actuator. The most important technical data of the actuator is provided in Table 4.4.2 [**60**].

Table 4.4.2: PI P-842.60 Preloaded Piezo Actuator technical data

Technical Data	**Value**
Open-loop travel for 0 to 100 V	90 µm
Maximum pushing capability	800 N
Maximum pulling capability	300 N
Resonant frequency	6 kHz
Mass	86 g
Length	127 mm

From the data provided in Table 4.4.2 it is clear the actuator is more than capable of meeting the specified requirements in terms of fretting frequency and slip amplitude, discussed in Section 4.2. It is however important to note that the actuator must be able to produce the 90 µm travel at a minimum frequency of 10 Hz, according to specification. The actuator therefore requires an input signal varying between o and 100 V at a minimum frequency of 10 Hz. Providing an input signal capable of meeting this requirement is however no easy feat. It was therefore decided to use a custom made signal amplification unit, manufactured by PI. The unit consists of one PI E-501 Modular Piezo Controller and one PI E-504 Amplifier Module. The important technical data of the signal amplification unit is provided in Table 4.4.3 [**61**].

Table 4.4.3: Technical data of the signal amplification unit consisting of one PI E-501 Modular Piezo Controller and one PI E-504 Amplifier Module

Technical Data	**Value**
Number of output channels	1
Control input voltage range (DC)	-2 to 12 V
Output voltage range (DC)	-30 to 130 V
Peak output power	280 W
Average output power	100 W
Maximum power consumption	30 W

From the data provided in Table 4.4.3 it is clear that the amplification unit is more than capable of providing the piezoelectric actuator with the input signal that it requires in order to perform according to specification. Figure 4.2 provides a photograph of both the piezoelectric actuator and the signal amplification unit.

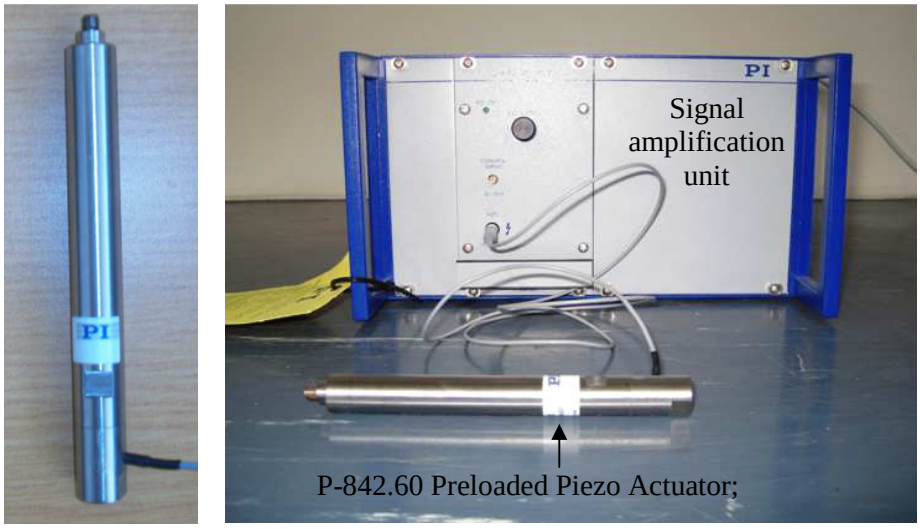

(a) (b)

Figure 4.2: PI (Physik Instrumente) piezoelectric actuation system consisting of: a) P-842.60 Preloaded Piezo Actuator; b) signal amplification unit connected to the actuator

The signal amplification unit also requires a signal to amplify and therefore the signal source of the Actuation Subsystem is provided by a signal/wave generator. To protect the signal amplification unit and the actuator, the signal provided by the signal generator has to be calibrated first, using an oscilloscope. System protection is however not the only function performed by the oscilloscope. The signal amplitude and frequency, which is directly related to the slip amplitude and fretting frequency provided by the actuator needs to be checked before the signal is provided to the signal generator, using the oscilloscope. Figure 4.3 provides a photograph of the entire Actuation Subsystem.

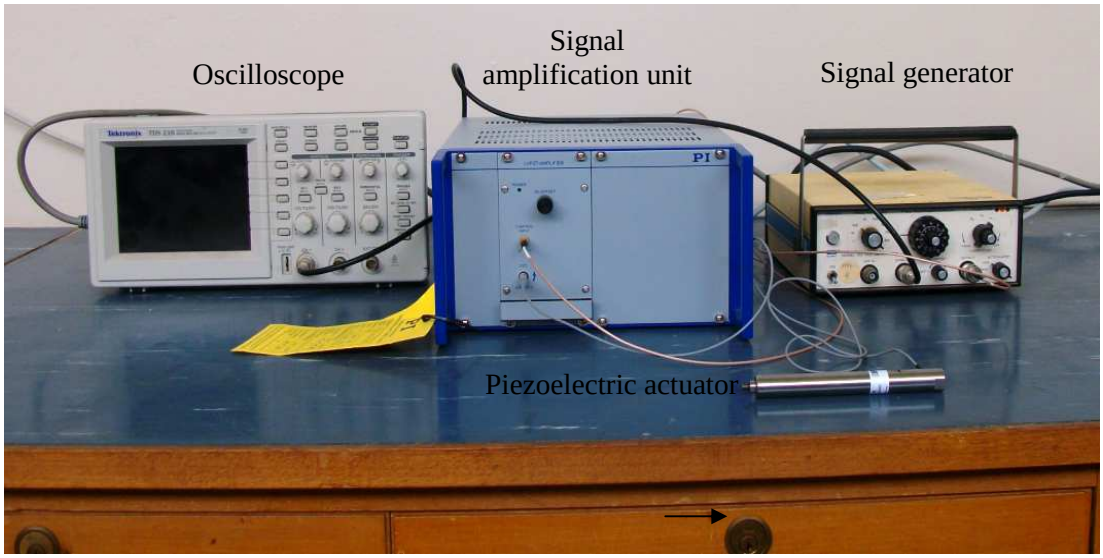

Figure 4.3: Actuation Subsystem

The subsystem utilizes open-loop control in order to create the fretting motions of the test apparatus. The open loop control of the subsystem is explained by the actuator open-loop control circuit provided in Figure 4.4.

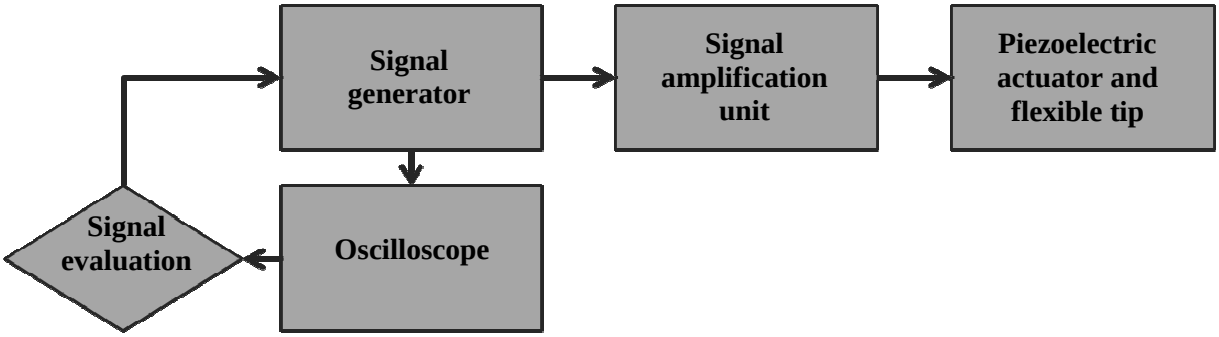

Figure 4.4: Actuator Open-loop control circuit

The open-loop control process of the Actuation Subsystem starts off by connecting the signal generator to the oscilloscope in order to evaluate the source signal produced by the signal generator. The signal properties evaluated are the signal shape, peak-to-peak voltage, signal frequency and the RMS voltage value of the signal. These properties are then modified until the perfect source signal is provided by the signal generator. When the source signal evaluation and modification is complete the signal generator output is connected to the input terminal of the signal amplification unit, using a special coaxial cable. The signal amplification unit then amplifies the signal and provides it to the piezoelectric actuator using another specialized coaxial cable fixed to the actuator. The Actuation Subsystem is connected to both the Structural Subsystem and the Specimen Holder Subsystem, as depicted in Figure 4.1. Both of the connection points of the Actuation Subsystem are located on piezoelectric actuator. The connection between the actuator and the Structural Subsystem, depicted by connection 1 in Figure 4.1, is a threaded M8 connection, connecting the back of the piezoelectric actuator to the structural subsystem. The connection between the actuator and the Specimen

Holder Subsystem, depicted by connection 4 in Figure 4.1, is threaded M5 connection between the tip of the piezoelectric actuator and the Specimen Holder Subsystem.

4.3.2 Specimen Holder Subsystem

The Specimen Holder Subsystem is responsible for housing the flat test specimens, but during operation the fretting interface is also located within the subsystem. From Figure 4.1 it is clear that Specimen Holder Subsystem is directly and/or indirectly connected to all of the other subsystem of the fretting test apparatus. This aspect was a key aspect during the design of the subsystem, seeing that the subsystem provides four direct and/or indirect connection points with the other subsystems. The subsystem was also designed to accommodate the fretting motion, seeing that the fretting interface is located within the subsystem during operation.

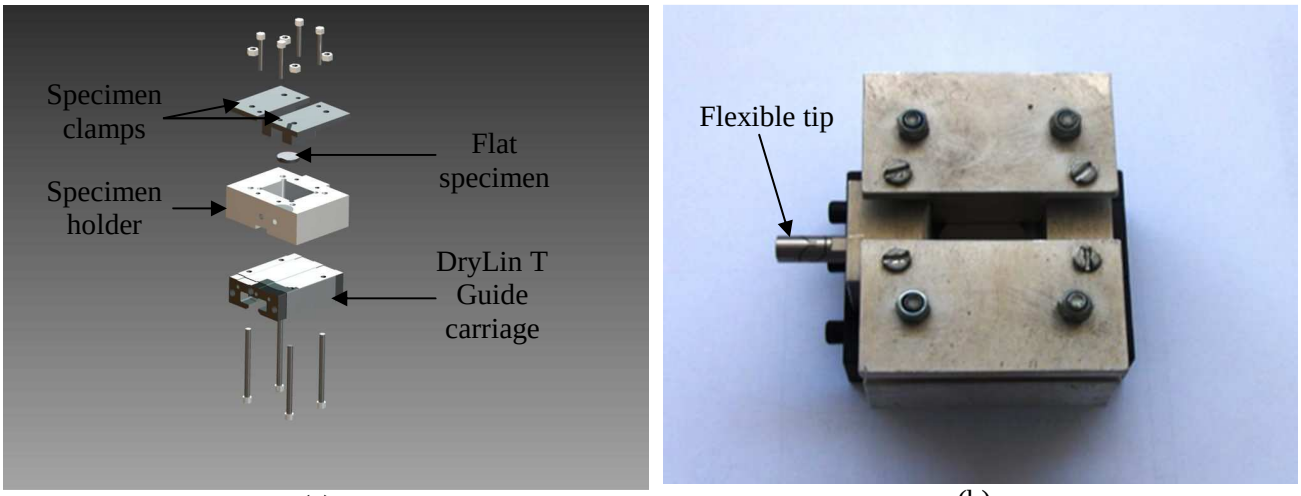

Figure 4.5: Specimen Holder Subsystem - (a) components; (b) assembly

Figure 4.5 provides a model of the Specimen Holder Subsystem components as well as a photograph of fully assemble subsystem. The base of the subsystem is a DryLin T Guide carriage (dry linear bearing carriage). The function of the carriage is to facilitate the fretting motion transferred from the Actuator Subsystem to the Specimen Holder subsystem, via the protective P-176.50/60 flexible tip connected to the piezoelectric actuator. The flexible tip is also a product of PI (Physik Instrumente) and is responsible for protecting the piezoelectric ceramic of the actuator against any induced bending forces. The carriage also forms part of connection 3 depicted in Figure 4.1, between the Specimen Holder Subsystem and a DryLin T Guide rail (Dry linear bearing rail), located on the Structural Subsystem. The specimen holder and the two specimen clamps depicted in Figure 4.5 were manufactured from aluminium in order to ensure that the Specimen Holder Subsystem is light as possible. The reason for this is to ensure that the weight of the subsystem would not influence the fretting motion created by the Actuation Subsystem.

The Specimen Holder Subsystem was designed to house flat specimens with minimum diameter or length of 18 mm and a maximum diameter or length of 35 mm. In order to correctly assemble the subsystem, the specimen is place in the middle of the specimen holder and then firmly clamped by the two specimen clamps. The four M5 bolt and nut couples in Figure 4.5 are used to connect the DryLin T Guide carriage to the specimen holder. These bolt and nut couples are however also used to perform the clamping action, in order to firmly clamp the specimen to the specimen holder, via the two specimen clamps. The four M4 bolts perform a secondary clamping action by connecting the specimen clamps to the specimen holder. The reason for the two phase clamping action is to firmly connect the specimen to the Specimen Holder Subsystem. This ensures that no relative motion will take place between the components involved, while the subsystem and the specimen is executing the fretting motion. Connection 5 depicted in Figure 4.1 represents the indirect connection between the Specimen Holder Subsystem and the Force Application Subsystem. This connection is termed indirect because it takes place via the fretting interface. This interface and consequently connection 5 is discussed in detail in Section 4.3.5. The Specimen Holder Subsystem is also connected to the Measurement Subsystem, corresponding to connection 9 in Figure 4.1. This connection is however discussed in detail in Section 4.4.

4.3.3 Force Application Subsystem

The Force Appliaction Subsystem is responsible for the application of a fully adjustable and controllable normal force at the fretting interface. The subsystem is also responsible housing the second test specimen, in order to complete the fretting interface. To complete these cardinal functions the subsystem was designed to consist of two parts (subassemblies), connected to the structural subsystem a different connection points. Figure 4.6: Force Actuation Subsystem provides two photographs, showing the two subassemblies that combine to form the Force Application Subsystem.

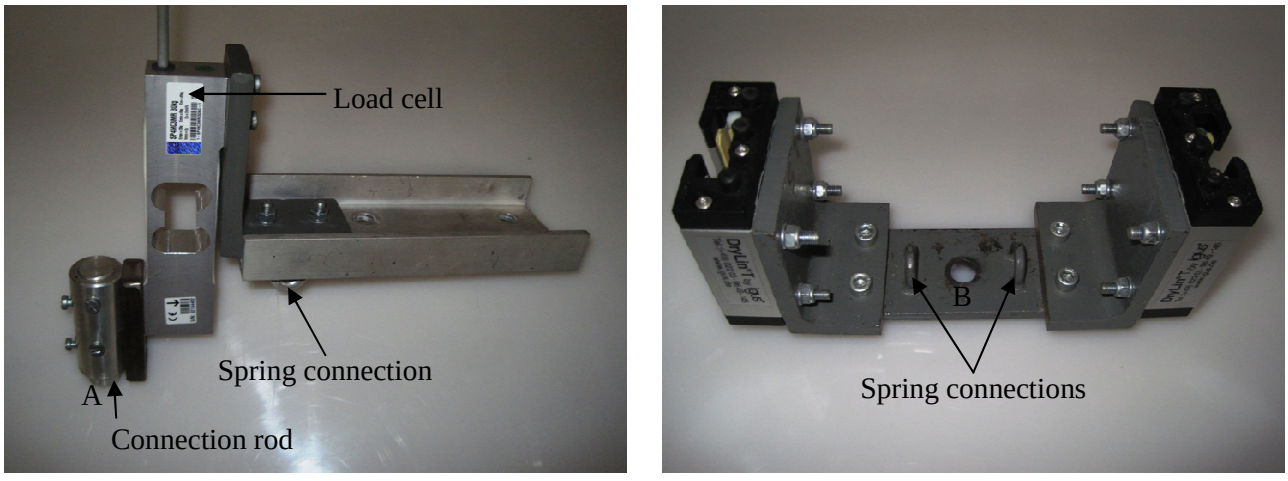

(a) (b)

Figure 4.6: Force Actuation Subsystem

The first subassembly shown in Figure 4.6(a) is directly responsible for housing the second test specimen. The connection rod shown in the figure is responsible for connection the second specimen to the rest of the Force Application Subsystem. Point A in the figure provides the location of the point where the second specimen is connected to the connection rod. The connection rod is connected to the subsystem by 6 separate M5 bolts, in order to ensure that no relative motion is able to take place between any of the components of the subsystem, including the second specimen. The subassembly in Figure 4.6(a) is also directly connected to the Structural Subsystem via four bolted connections. One 30 kg single point load cell, manufactured by HBM, forms part of the structure of this subassembly. This load cell also forms part of the measurement system of the fretting test apparatus and is discussed in full detail in Section 4.4.

A photograph of the second subassembly of the Force Application Subsystem is provided in Figure 4.6(b). This subassembly is also connected to the Structural Subsystem at three individual points. The first of these points is point B in the figure and connects to the structural subsystem via an M12 bolt, known as the force screw. The subassembly also contains DryLin T Guide carriages that connect to two DryLin T Guide rails, located on the Structural Subsystem. During operation the two subassemblies of the Force Application subsystem are directly connected by two extension springs. These spring connections are also provided in Figure 4.6. The two extension springs are directly responsible for the creation, control and adjustment of the normal force. The springs were manufactured from steel by Capewell Springs, according to the design specifications provided in Table 4.4.4. A Photograph of the two extension springs are provided in Figure 4.7.

Table 4.4.4: Extension spring design specifications

Specification	**Value**
Wire diameter	1.5 mm
Outside Diameter	18.5 mm
Number of coils	10
Free length	70 mm
Spring rate	1.02 N/mm

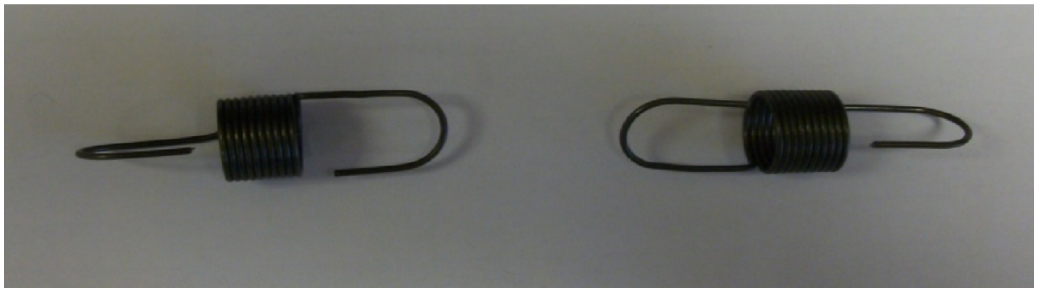

Figure 4.7: Extension springs

4.3.4 Structural Subsystem

According to Waterhouse internal vibration and resonance are extremely troublesome for fretting test rigs [**53**]. The best methods for counteracting these problems are the use of threaded connections and anti-fret lubricant. For this reason no welded connection were used during the design of the Structural Subsystem. All the connections in the subsystem are bolted connections, utilizing high tensile bolts and nuts. Figure 4.8 provides three photographs of the Structural Subsystem.

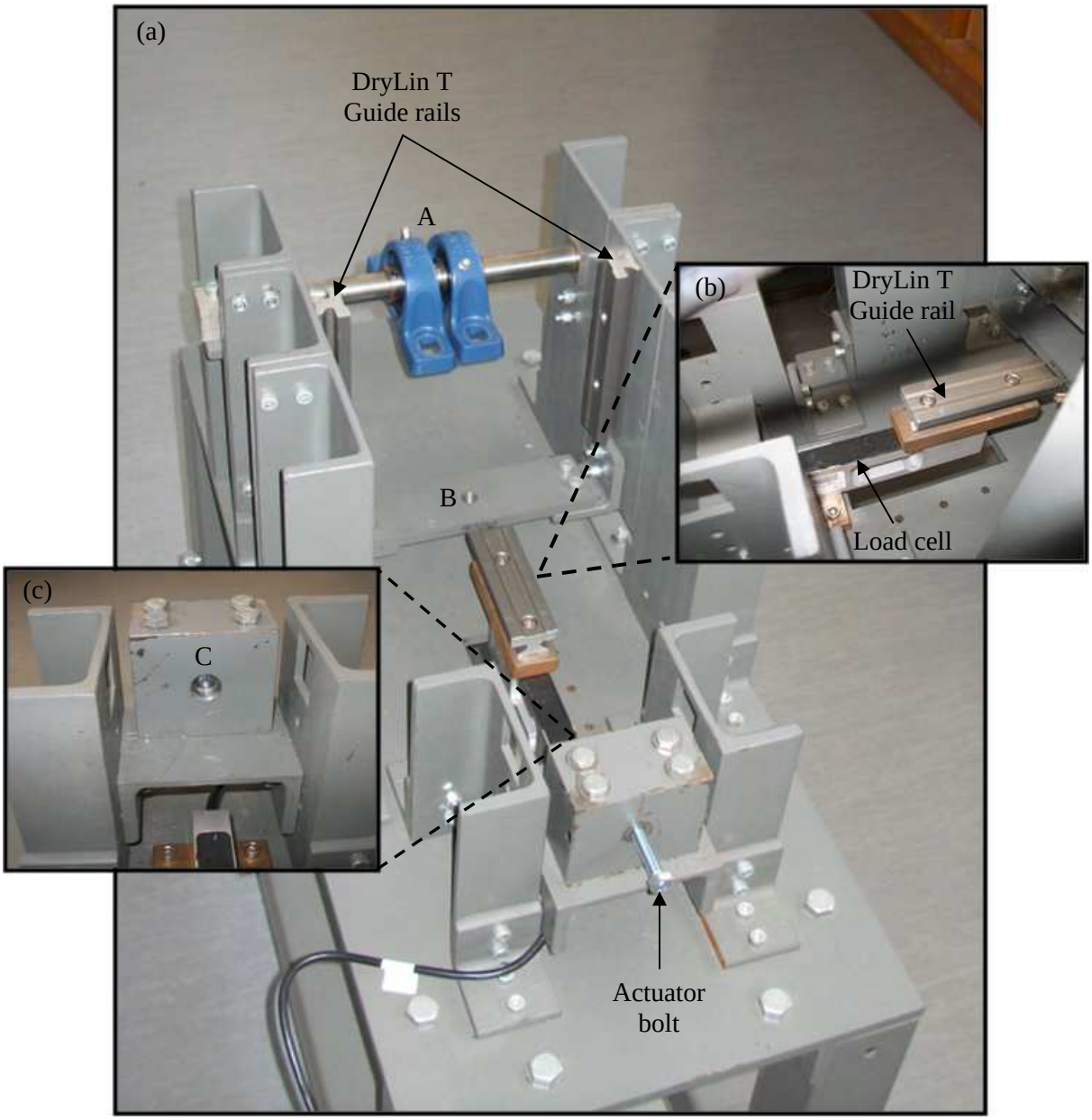

Figure 4.8: Structural Subsystem

The Structural Subsystem is connected to all the other subsystem of the fretting test apparatus. Point C in Figure 4.8(C) provides the connection point between the Actuation Subsystem and the structural subsystem. This connection corresponds to connection 1 depicted in Figure 4.1. In order to complete this connection a

M8 actuator bolt is used to firmly bolt the back of the piezoelectric actuator to the Structural Subsystem. Figure 4.8(b) shows the connection between the Specimen Holder Subsystem and the Structural Subsystem, via the DryLin T Guide rail in the figure and the DryLin T Guide carriage in Figure 4.5. This connection represents connection 3 in Figure 4.1. The load cell shown in Figure 4.8(b) also forms part of the Measurement Subsystem, thus representing connection 7 in Figure 4.1.

The Structural Subsystem connects to the Force Application Subsystem using three different connections. The first of these connections is between the two 20mm SKF bearing, located at point A in Figure 4.8(a), and the first subassembly of the Actuation Subsystem in Figure 4.6(a). The second connection is between the two DryLin T Guide rails, shown in Figure 4.8(a), and the two DryLin T Guide carriages of the second subassembly of the Force Application Subsystem in Figure 4.6(b). The third connection is facilitated by the Force Screw mentioned in Section 4.3.3. For this connection the Force Screw is connected between point B in Figure 4.8(a) and point B in Figure 4.6(b), in order to adjust and control the normal force applied by the Force Application Subsystem.

4.3.5 Fretting Interface

The fretting interface is the indirect connection between the Specimen Holder Subsystem and the Force Application Subsystem. Each fretting interface created by the fretting test apparatus consists of two test specimens. Figure 4.9 provides a photograph of the test specimens manufactured in order to complete the three main fretting interfaces discussed in Section 4.2.

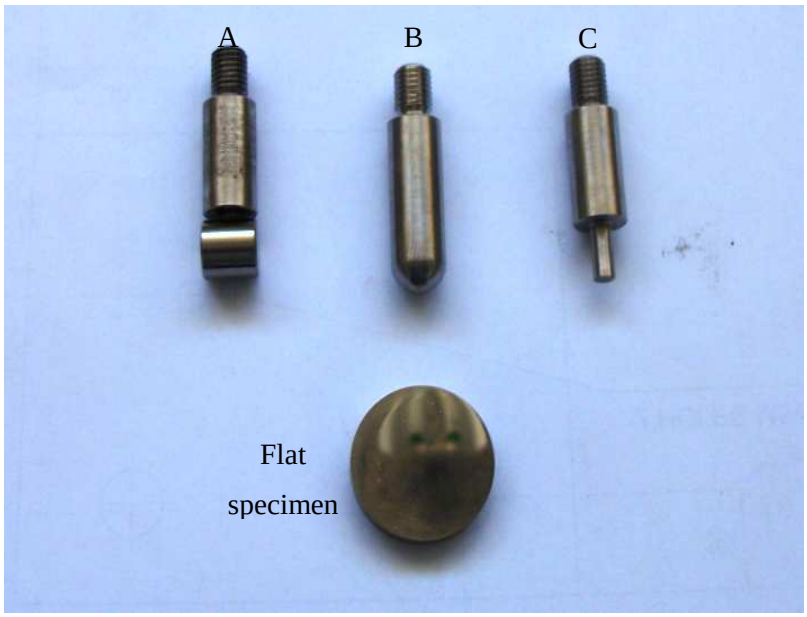

Figure 4.9: Test Specimens

The flat specimen in the figure is clamped within the Specimen Holder Subsystem, while the specimen A, B and C connects to the connection rod of the Force Application Subsystem shown in Figure 4.6(a). Specimen

A in the figure consists of a mounting pin and a cylindrical specimen that combines with flat specimen to create a cylinder-on-flat fretting contact. Specimen B combines with the flat specimen to create a sphere/ball-on-flat fretting contact. Finally, Specimen C combines with the flat specimen to create a flat-on-flat fretting contact. Figure 4.10(a) provides a photograph of the fully assembles fretting test apparatus, with the fretting interface provided in Figure 4.10(b).

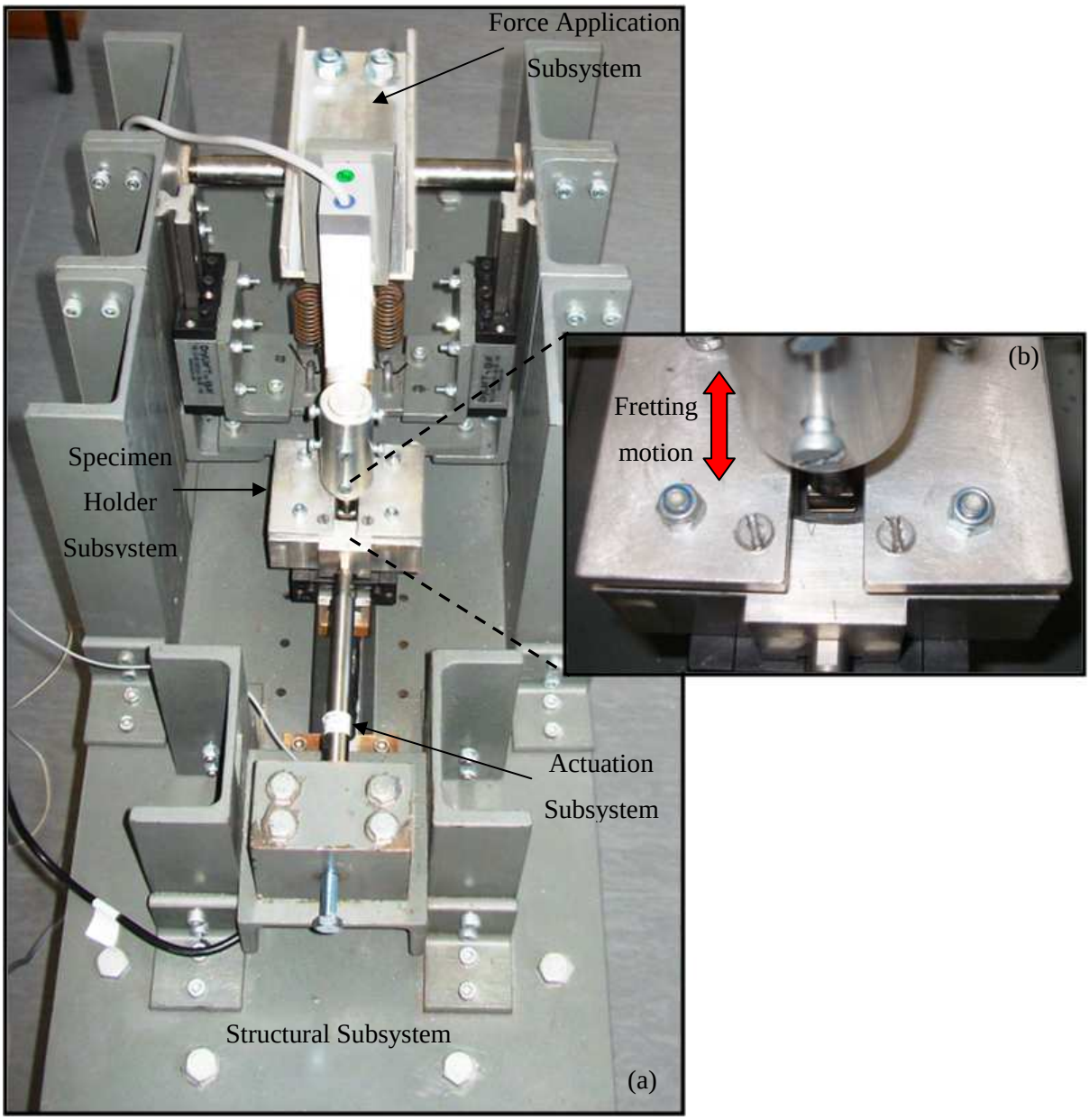

Figure 4.10(a) Assemble fretting test apparatus; (b) fretting interface

The fretting interface in Figure 4.10b) is a cylinder-on-flat fretting contact, subjected to a fretting motion in the tangential direction with respect to the cylindrical Specimen.

4.4 Measurement of Key Parameters and Data Acquisition

Measurement and data acquisition is extremely important during fretting experimentation and is the responsibility of the Measurement Subsystem. According to Dobromirski there may be 50 different variables that affect the fretting process [**33**]. Many of these variables have been investigated over past five decades. The variables that have been investigated in laboratories include [**33**]:

- Temperature
- Hardness of the contact surfaces
- Contact Pressure
- Normal force
- Slip amplitude
- Coefficient of friction
- Tangential Force
- Contact area
- Frequency of vibration
- Number of cycles
- Ambient atmosphere
- Atmospheric pressure
- Humidity
- Lubricants
- Material characteristics
- Material microstructure
- Metallurgical compatibility
- Size effect
- Corrosion susceptibility
- Surface roughness

Unfortunately most literature reports and articles vary in their assessment of the influence of these variables. According to Dobromirski there is also no standardized testing procedure for fretting experimentation [**33**]. Therefore most authors decide which variables to measure, based on the outputs needed to complete their investigation. In order to qualitatively investigate and control the fretting wear process, for this particular study, it was established that the following list of outputs were needed:

- Normal force data
- Tangential force data
- Fretting frequency data
- Slip amplitude data
- Coefficient of friction information
- Wear scar images (microscopy and SEM)

In order to measure the normal force and tangential force it was decided to use two 30 kg single point load cells. Normally load cells would not be used for dynamic force measurement, and dedicated force transducers would be used instead. Unfortunately budgeting considerations did not allow the use of dedicated force transducers. Single point loads cells are however more than capable of producing reliable force measurements, as long as the kilogram values provided by the loads cells are converted to Newton using the

universal gravitational acceleration value. The load cell responsible for measuring the normal force is a Tedea Huntleigh Model 1042 30 kg single point load cell, and it forms part of the Structural Subsystem. The location of this load cell is provided in Figure 4.8(b) and it is directly connected to the base plate of the Structural Subsystem by 2 M6 bolts, and indirectly connected to the DryLin T Guide rail, via a mounting plate and two more M6 bolts. In order to eliminate any errors the load cell is located as close to the connection point between the Structural Subsystem and the Specimen Holder subsystem as possible. This means that any force exerted by the DryLin T Guide carriage of the Specimen Holder Subsystem on the rail will be directly measured by the load cell, without the interference of any additional components. The second load cell is a HBM SP4C3 30 kg single point load cell. This load cell is responsible for measuring the tangential force exerted by the flat specimen, mounted within the Specimen Holder Subsystem, on the second specimen connected to the Force Application Subsystem. Figure 4.5(a) provides the location of this load cell. From the figure it is clear that the load cell is located as close to specimen 2 as possible. This was done in order to eliminate any errors caused by additional components between the fretting interface and the load cell.

One Endevco Model 256HX Isotron Accelerometer was chosen for the measurement of the fretting frequency and the slip amplitude. The reason for this is that a single accelerometer is capable of measuring both of these parameters simultaneously. The 256HX is a small piezoelectric accelerometer, designed specifically for performing vibration measurements on small structures. The accelerometer is mounted using a stud and is light weight (4g), in order to minimize any mass loading effects. The Specimen Holder Subsystem provides the connection point for the accelerometer, as close to the fretting interface as physically possible. Figure 4.11(a) provides a photograph of the components of the accelerometer, while Figure 4.11(b) provides a photograph of the accelerometer connected to Specimen Holder Subsystem.

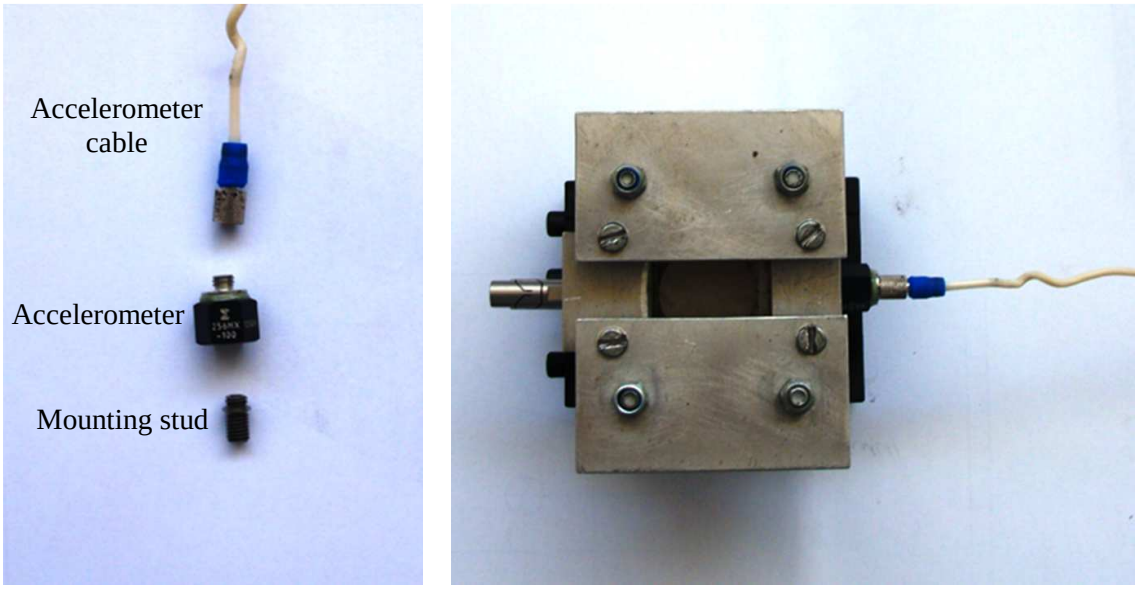

(a) (b)

Figure 4.11: (a) Components of the Endevco Model 256HX Isotron Accelerometer; (b)Connection between the accelerometer and the Specimen Holder Subsystem

The Measurement Subsystem also contains a HBM QuantumX MX410 - 4-Channel Universal Amplifier. The universal amplifier is an extremely important part of the Measurement subsystem and is responsible for performing the following 4 functions:

- Capture the analog signals provided by the two load cells and the accelerometer.
- Amplification of the captured analog signals.
- Conversion of the amplified analog signals to digital signals.
- Direct digital communication with the computer in order to provide real-time visualizations of the measured data.

Table 4.4.5 provides some important technical data regarding the HBM QuantumX MX410 - 4-Channel Universal Amplifier.

Table 4.4.5 Technical data of the HBM QuantumX MX410 - 4-Channel Universal Amplifier [**62**]

Technical Data	**Value**
Number of individually configurable inputs	4
Number of analog outputs	4
Maximum sampling rate	19.2 kHz
DC supply voltage	10 V to 30 V

Figure 4.12 provides a photograph of the universal amplifier. The universal amplifier also offers a variety of connection possibilities in order to facilitate communication between the amplifier and any computer. The connection utilized for this study is the direct Ethernet connection. This connection as well as the connections between the universal amplifier and rest of the equipment is shown in Figure 4.12.

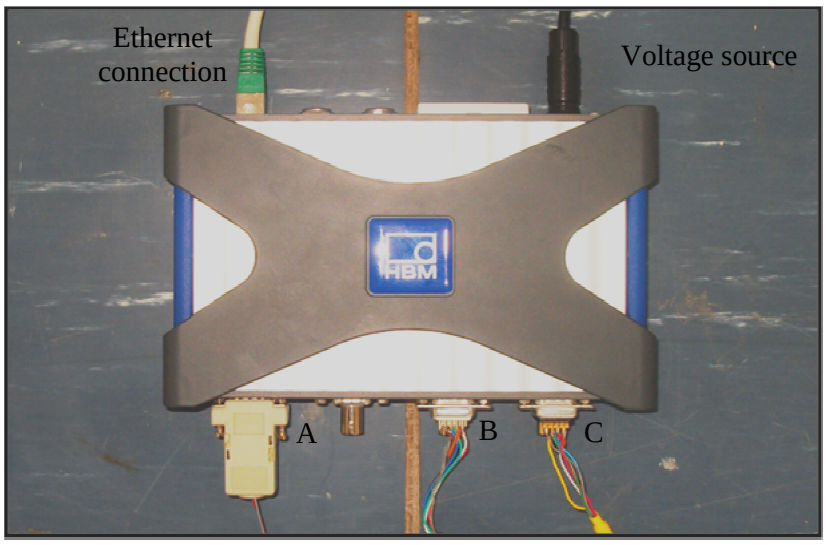

Figure 4.12: HBM QuantumX MX410 - 4-Channel Universal Amplifier

Point A in the figure is connection between the accelerometer and the universal amplifier, while points B and C are the connected between the two load cells and the universal amplifier. The software used in order to capture the experimental data is a specialized data acquisition and processing software package, provided by HBM especially for the QuantumX series of universal amplifiers. The name of the software package is catmanEasy-AP (version 3.1). Figure 4.13 prides a screen shot of the visualization of the measured data provided by the catmanEasy-AP software. The data depicted in the Figure 4.13 represent data recorded during a calibration experiment of the fretting test apparatus. Graph B in the figure represents the normal force (in kg) measured by the load cell in Figure 4.8(b). Graph C in the figure represents the tangential force (in kg) measured by the load cell in Figure 4.6(a).

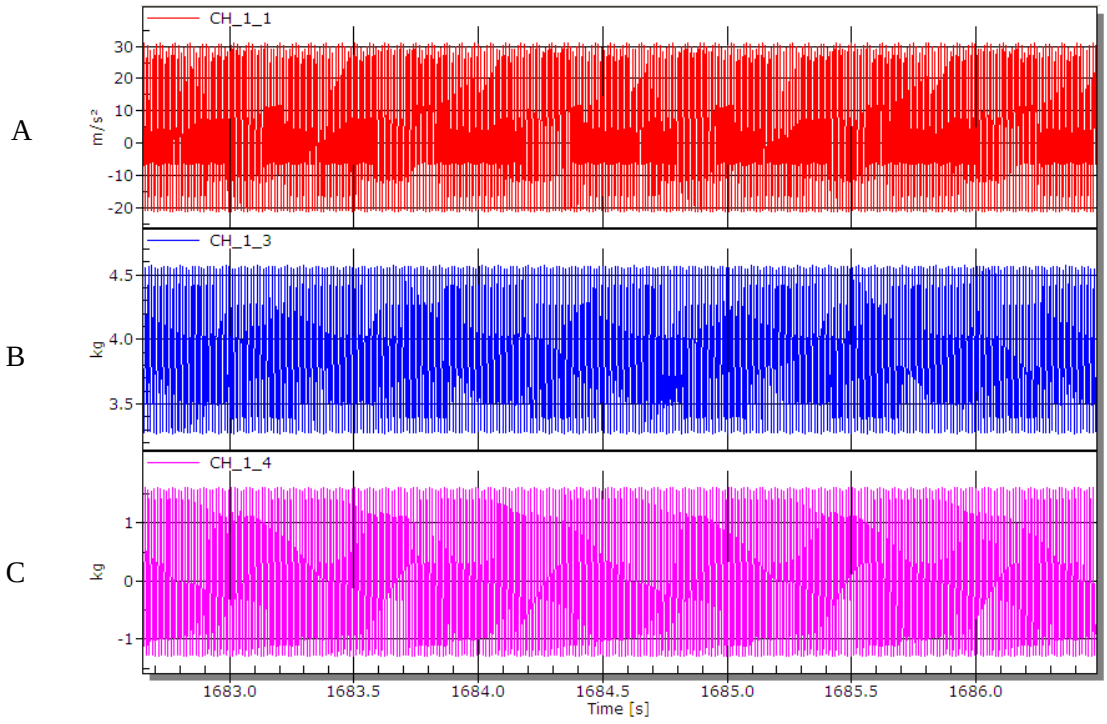

Figure 4.13: CatmanEasy-Ap (version 3.1) visualization

Graph A in Figure 4.13 represents the acceleration data measured at the fretting interface. The data produced is in the form of acceleration, measured in m/s^2 or g (gravitational acceleration). It is however possible to convert such acceleration signals into a frequency signals as well as displacement signals, using certain mathematical means. The mathematical means used in order to perform these conversions is known as Fourier Transforms.

4.5 Determination of Friction Coefficients

Hutchings defines the force known as friction as the resistance experienced by one body when moving over another body [**2**]. In 1699 Amontons discovered the following two empirical laws of sliding friction [**2**]:

1. Friction is proportional to the normal load
2. The friction force is independent of the area of the contact

In 1785 Coulomb added the following third law to the list:

3. The friction force is independent of the sliding velocity

The fist law of friction can be expressed by Equation 4.1. The second and third laws of friction have not been explored the detail, compared to the first law. The friction force needed to initiate sliding is usually greater than the friction force needed to maintain it [**2**]. Accordingly, the coefficient of static friction is greater than the coefficient of dynamic friction. In order to understand this statement in terms of fretting, refer to the schematic provide in Figure 4.14.

$$F = \mu N \qquad \text{Equation 4.1}$$

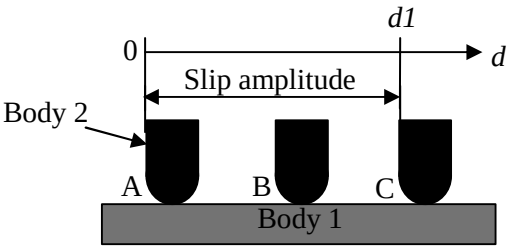

Figure 4.14: Fretting related friction schematic

The schematic in Figure 4.14 represents a simple fretting contact, consisting of two bodies in contact. Body 1 represents a stationary body, while Body 2 is subjected to fretting motion (or slip). The figure also depicts the path of Body 2 for each fretting cycle that the contact is subjected to. At the start and the end of each cycle Body 2 is located at point A. Halfway through each cycle the Body 2 is located at point C. Point A and point C therefore present the two points where the fretting motion changes direction, making these the two

points of static friction for each cycle. At point B in the figure Body 2 is in motion. At this point Body 2 is subjected to dynamic friction. Equation 4.2 and Equation 4.3 provides the mathematical description of the coefficient of friction per fretting cycle.

$$\mu = \mu_d \quad \text{for} \quad 0 < d < d1 \qquad \text{Equation 4.2}$$
$$\mu = \mu_s \quad \text{for} \quad d = 0 \text{ and } d = d1 \qquad \text{Equation 4.3}$$

For the purpose of this study, information regarding the coefficient of friction for each experiment is of the utmost importance. It was therefore decided to use either the coefficient of static friction or the coefficient of dynamic friction, depending on which of these produced the highest value per cycle, consequently influencing the fretting contact the most. In order to decide between the two coefficients, several preliminary experiments were conducted. A data processing program was also written in Matlab in order to process the normal and tangential force data provided by the two load cells into graphical representations of the average static coefficient of friction and the dynamic coefficient of friction. The name of the program is "static_vs_dynamic" and it is provided in APPENDIX B. The determination of the average static and dynamic tangential force for each fretting cycle is explain using the tangential force distribution of a generic fretting experiment, provided in Figure 4.15.

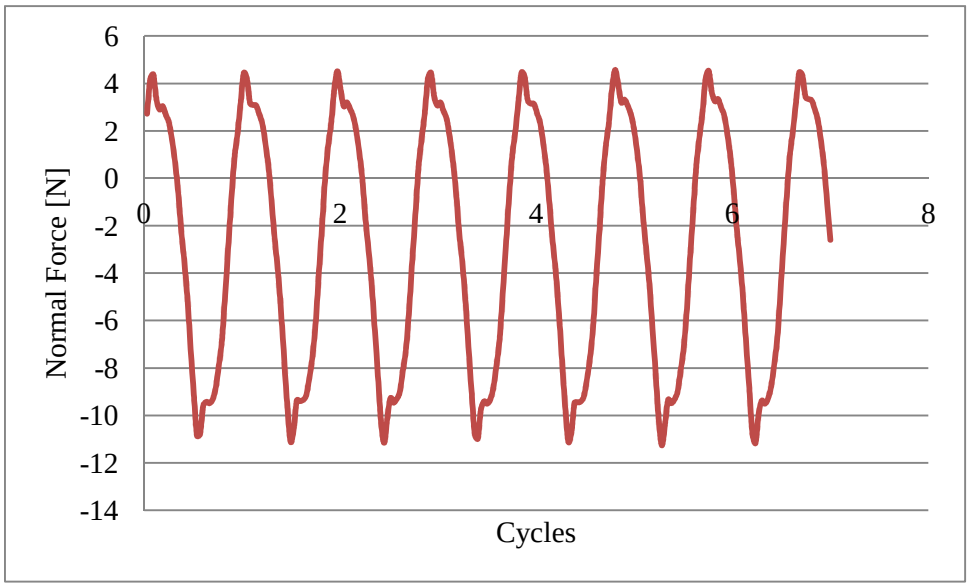

Figure 4.15: Tangential force distribution of a generic fretting experiment

Consider that each fretting cycle consists of *n* measured data points, containing a minimum and maximum value. These minimum and maximum values correspond to the two points of static friction, per fretting cycle. The data processing procedure starts off by dividing the entire data set *x(i)*, containing a total of *i* data points, into *m* separate data vectors consisting of n data points each. Each of the created vectors represents a fretting cycle. This is done using Equation 4.4.

$$T(c) = \left[x\left((c-1)*n+1\right);\ x\left((c-1)*n+2\right); \ldots;\ x\left((c-1)*n+n\right)\right] \qquad \text{Equation 4.4}$$

with $c = 1; 2; \dots; m$

T(c) represents each cycle vector created. The next step is to determine the average between the two static friction force values for each cycle, using Equation 4.5. The average dynamic tangential force for each fretting cycle is determined using Equation 4.6.

$$T_s(c) = \frac{max(T(c)) + |min\,(T(c))|}{2} \qquad \text{Equation 4.5}$$

$$T_d(c) = \frac{\sum|T(c)|}{n} \qquad \text{Equation 4.6}$$

In order to generate coefficient of dynamic and static friction data, the normal force data also needs to be processed. In order to do so the entire normal force dataset *y(i)* is also divided into normal force cycle vectors, in a similar manner to the one used for the tangential force. This is done using Equation 4.7.

$$N(c) = \left[y\big((c-1)*n+1\big);\ y\big((c-1)*n+2\big); \dots;\ y\big((c-1)*n+n\big)\right] \qquad \text{Equation 4.7}$$
with $c = 1; 2; \dots; m$

N(c) represents each cycle vector created. The next step is to determine the average normal force per cycle, using Equation 4.8.

$$N_{avg}(c) = \frac{\sum|N(c)|}{n} \qquad \text{Equation 4.8}$$

The average coefficient of dynamic and static friction vectors, according to the first law of friction, is then determined using Equation 4.9 and Equation 4.10 respectively.

$$\mu_d\,(c) = \frac{T_d(c)}{N_{avg}(c)} \qquad \text{Equation 4.9}$$

$$\mu_s\,(c) = \frac{T_s(c)}{N_{avg}(c)} \qquad \text{Equation 4.10}$$

The results obtain from the preliminary experiments were very conclusive. Accordingly, the coefficient of static friction was higher than the coefficient of dynamic friction for all of the experiments. Figure 4.16 provides the comparative coefficient of friction graph between the static- and dynamic fiction coefficients for one of the preliminary fretting experiments between a Ti-6Al-4V ball and a Inconel 718 flat.

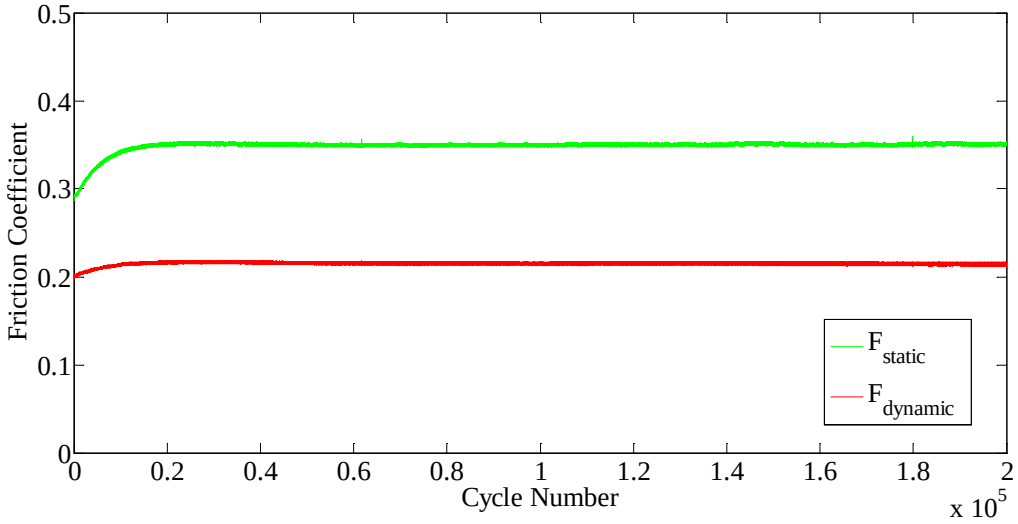

Figure 4.16: Coefficient of friction graph for a Ti-6Al-4V ball on Inconel 718 flat fretting experiment subjected to: normal force = 40N; slip amplitude = 80 μm; frequency = 40Hz

From the figure it is clear that the coefficient of static friction was much higher than that coefficient of dynamic friction. It was therefore decided to only consider the coefficient of static friction data for the formal experimental study, discussed in Chapter 5. This was because the static friction was the highest for all the experiments and consequently had largest effect on the contact interface.

5 Experimental Study

5.1 Introduction

The developed fretting test apparatus described in the previous chapter was used to perform the experimental study described in this chapter. Upon completion of the test apparatus a series of preliminary test were performed in order to refine and calibrate the apparatus. The general outline of the entire experimental study of the project is presented in Figure 5.1.

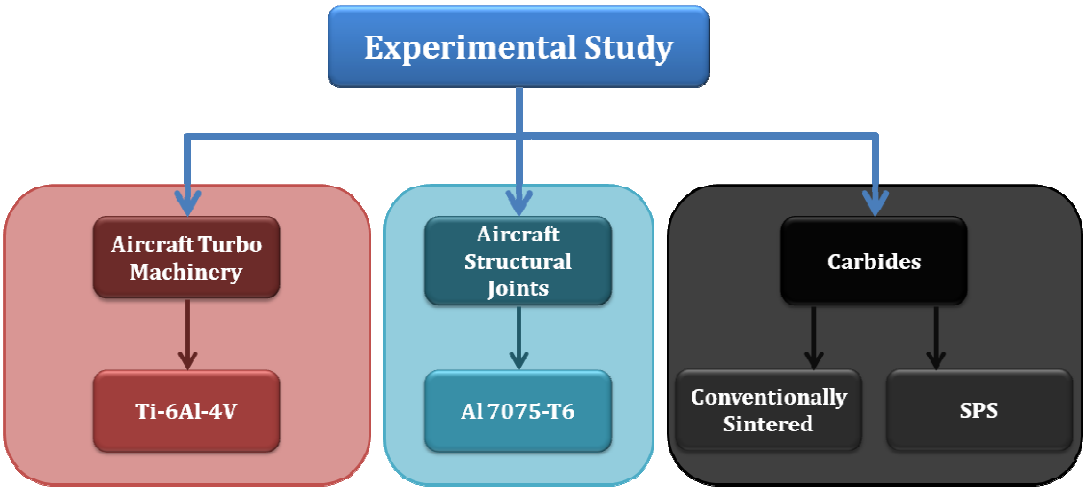

Figure 5.1: Outline of experimental study

The experimental study is divided into three main sections, depending on application to the aerospace industry. The first of these applications is fretting wear encountered in aircraft turbo machinery. This application was discussed in Chapter 3 and the material investigated was the titanium alloy Ti-6Al-4V. The second application is fretting wear encountered in the riveted joints of aircraft structures. The material investigated in this section was the aluminium alloy Al7075-T6. The third and final part of the experimental study investigates fretting wear of cemented tungsten carbide. Two materials were investigated in this section. The first material was conventionally sintered cemented tungsten carbide, while the second material was cemented tungsten carbide sintered by a specialized process known as Spark Plasma Sintering (SPS).

5.2 Fretting wear in Aircraft Turbo Machinery

This section discusses the fretting wear investigated for Ti-6Al-4V dovetail- and fir tree joint contact interfaces, as discussed in Chapter 3. In order to thoroughly investigate the possible fretting wear at these joints it was important to identify all the possible fretting contact configurations. Figure 5.2 provides a model of a typical dovetail joint, also providing the possible fretting contact interfaces, as well as the possible fretting motions that can take place at each of these interfaces.

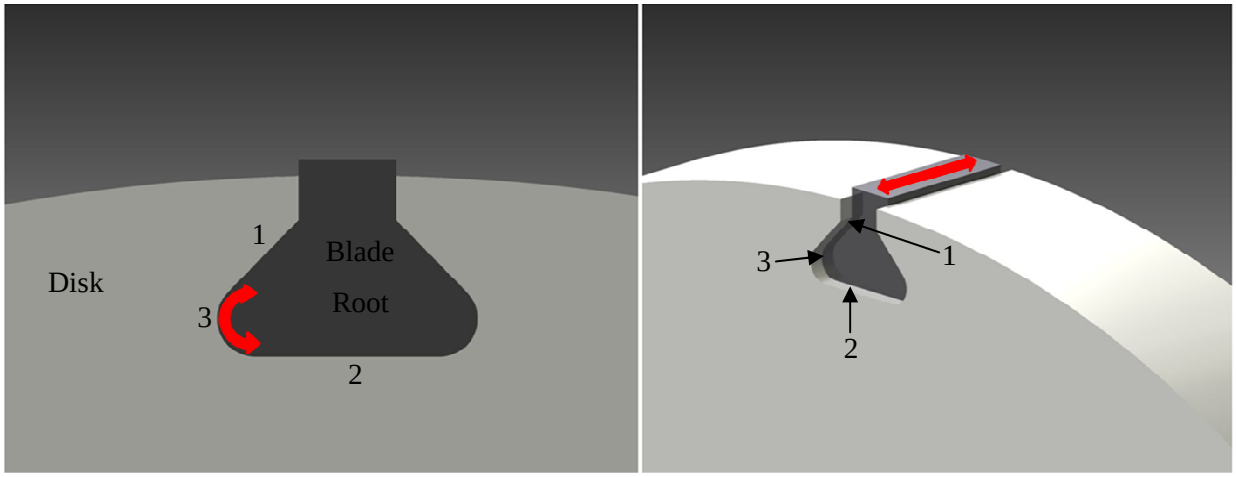

(a) (b)

Figure 5.2: Fretting contact interfaces encountered in a typical dovetail joint for a) slight angular motion; b) axial motion.

Figure 5.2 reveals three possible fretting contacts. These three contacts represent the three well known fretting contacts, provided in Figure 5.3. The fretting contact provided in Figure 5.3(a) is a cylinder-on-flat contact subjected to a normal force and a tangential fretting motion. This type of fretting contact can occur at point 3 in Figure 5.2, when subjected to the slight angular fretting motion depicted by the red arrow in Figure 5.2(a). The fretting contact provided in Figure 5.3(b) is the same as the contact provided in Figure 5.3(a), but in this case the fretting motion is in the axial direction. This type of fretting contact can also occur at point 3 in Figure 5.2, but as a result of the axial motion depicted by the red arrow in Figure 5.2(b). The third and final possible fretting contact is a flat-on-flat contact subjected to a normal force and fretting motion. This type of fretting contact can take place at point 1 and point 2 in Figure 5.2, as a result of both axial and slight tangential fretting motions.

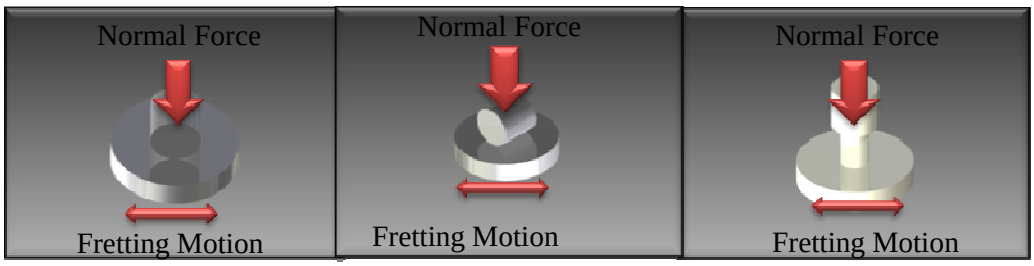

(a) (b) (c)

Figure 5.3: Possible fretting contacts resulting from a typical dovetail joint: a) cylinder-on-flat subjected to tangential motion; b) cylinder-on-flat subjected axial motion; c) flat-on-flat

Figure 5.4 provides a model of a typical fir tree joint, providing the possible fretting contact interfaces as well as the possible fretting motions that can take place at these interfaces. The figure reveals two possible fretting contacts. These two contacts are the same as the first two fretting contacts discussed for the typical dovetail joint. The fretting contact provided in Figure 5.3(a) can occur at points 1 to 5 in Figure 5.4, when subjected to the slight angular fretting motions depicted by the three red arrows in Figure 5.4(a). The fretting

contact in Figure 5.3(b) can also occur at points 1 to 5 in Figure 5.4, but as a result of the axial fretting motion depicted by the red arrow in Figure 5.4(b).

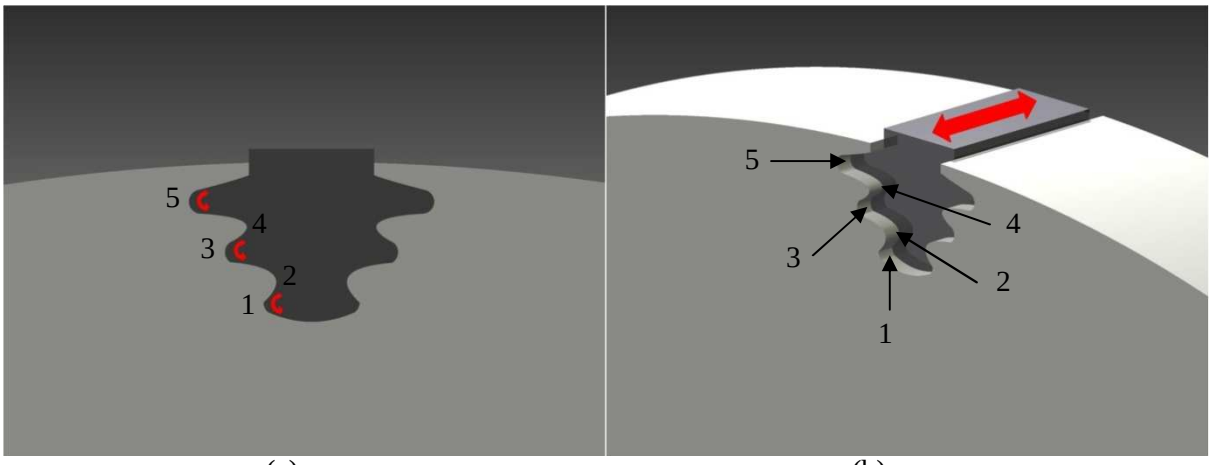

(a) (b)

Figure 5.4: Fretting contact interfaces encountered in a typical fir tree joint for a) slight angular motion; b) axial motion.

After identifying the three possible fretting contact configurations that can possibly occur at dovetail- and fir tree joints the experimental procedure for the Ti-6Al-4V applications was developed. The developed procedure is represented by the diagram provided in Figure 5.5.

The fretting wear investigation Ti-6Al-4V was divided into three main categories, according to the fretting contact configurations provided in Figure 5.3. The developed fretting test apparatus discussed was then used to conduct the experiments for each of the contact configurations. The experimental procedure for each contact was conducted for 10^5 and 2×10^5 cycles. For each of the two fretting cycle categories, three fretting wear experiments were conducted at a normal force of 40N, 30N and 20N respectively. After completing the three experiments for 10^5 cycles and 2×10^5 cycles, the worst case scenario in terms of fretting wear was identified per fretting contact. After identifying the worst case scenario per fretting contact, each of the worst case experiments was run for an extended period of 10^6 cycles.

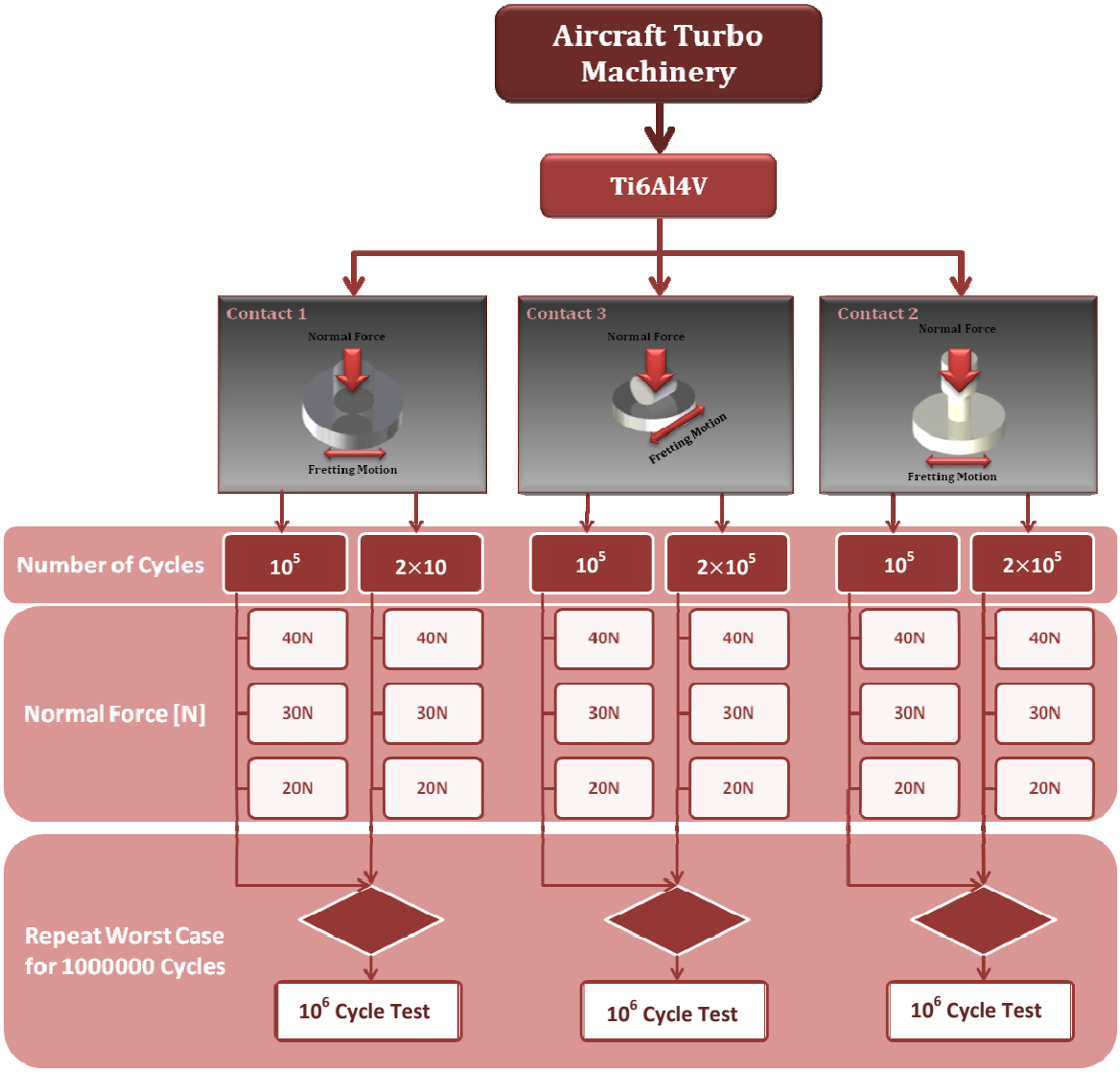

Figure 5.5: Experimental procedure for Ti-6AL-4V Aircraft Turbo Machinery Applications

Table 5.1: Mechnical properties of Ti-6Al-4V at room temperature [**63**,**64**]

Mechanical property	**Ti-6Al-4V**
Hardness [GPa]	2.96 – 3.46
Density [g/cm^3]	4.43
Fracture Toughness [MPa.m$^{1/2}$]	75
Modulus of Elasticity [GPa]	113.8

Table 5.2 Composition of Ti-6Al-4V [**65**]

Ti	**Al**	**V**	**Fe**	**Si**	**C**	**N**	**H**	**O**
Balance	5.5– 6.8	3.5– 4.5	0.3	0.15	0.1	0.05	0.015	0.15

The mechanical properties and the composition of Ti-6Al-4V are provided in Table 5.1 and Table 5.2. All Fretting experiments were conducted at a peak-to-peak slip amplitude of 100 µm and a constant fretting

frequency of 80 Hz. The contact interfaces investigated were also not lubricated and were subjected to the surrounding ambient atmosphere, and consequently normal atmospheric conditions.

5.2.1 Cylinder-on-Flat Contact Subjected to Tangential Motion

After completing the fretting wear experiments for the Ti-6Al-4V cylinder-on-flat fretting contact subjected to tangential motion, the coefficient of static friction for the 2×10^5 cycle experiments were calculated. The program used to process the experimental data was discussed in Chapter 4 and is provided in APPENDIX B. The resulting coefficient of static friction graphs for 40N, 30N and 20N are provided in Figure 5.6. From the figure it is clear that the three graphs in the figure exhibit the same basic trends, and the normal force had a significant influence of the coefficient of static friction, resulting in an increase in the coefficient when the normal force was decreased.

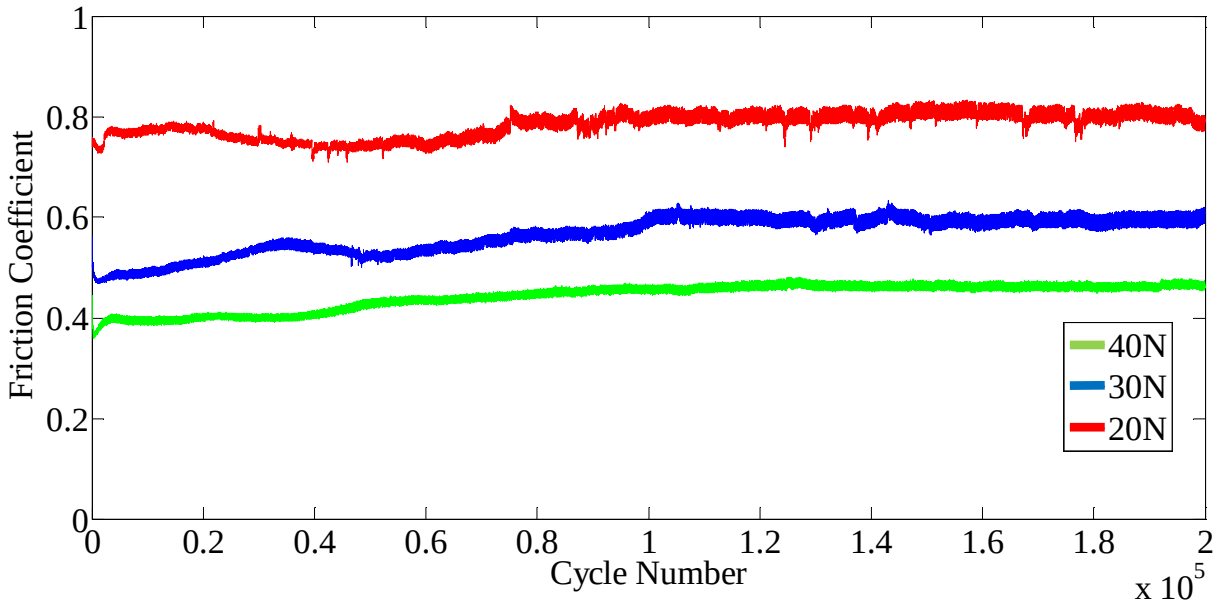

Figure 5.6: Coefficient of friction for Ti-6Al-4V cylinder on Ti-6Al-4V flat subjected to tangential motion [Frequency = 80Hz, Slip (peak-to-peak) = 100 µm; Cycles = 2×10^5]

In order to better understand the above stated conclusion, optical microscopy was used to investigate the wear scars located on the flat test specimens. The microscope used was an Olympus GX51 inverted optical microscope. The microscope images were generated using the Analysis 5.0 (Build 1210) Olympus Soft Imaging Solutions GmbH software package. The microscope images of three wear scars are provided in Figure 5.7. The wear scars in the figure seem to be small starch marks in the direction of the fretting motion, indicated by red arrow in each image. Further investigation of the three wear scars also revealed the width and consequently the severity of the wear scars increased with a decrease in the normal load. This was to be expected, because a lower normal load will result in less adhesion and more slip at the contact interface, constituting abrasion driven abrasion wear phenomena. This causes the individual asperity contacts to be broken, resulting in larger wear scar areas. It is therefore assumed that more asperity interaction will take

place at lower normal loads. Combining this assumed result with the information from the coefficient of static friction graphs in Figure 5.6 revealed the following:

The fretting wear of the cylinder-on-flat Ti-6Al-4V fretting contacts, subjected to tangential motion was increased by a decrease in the normal force.

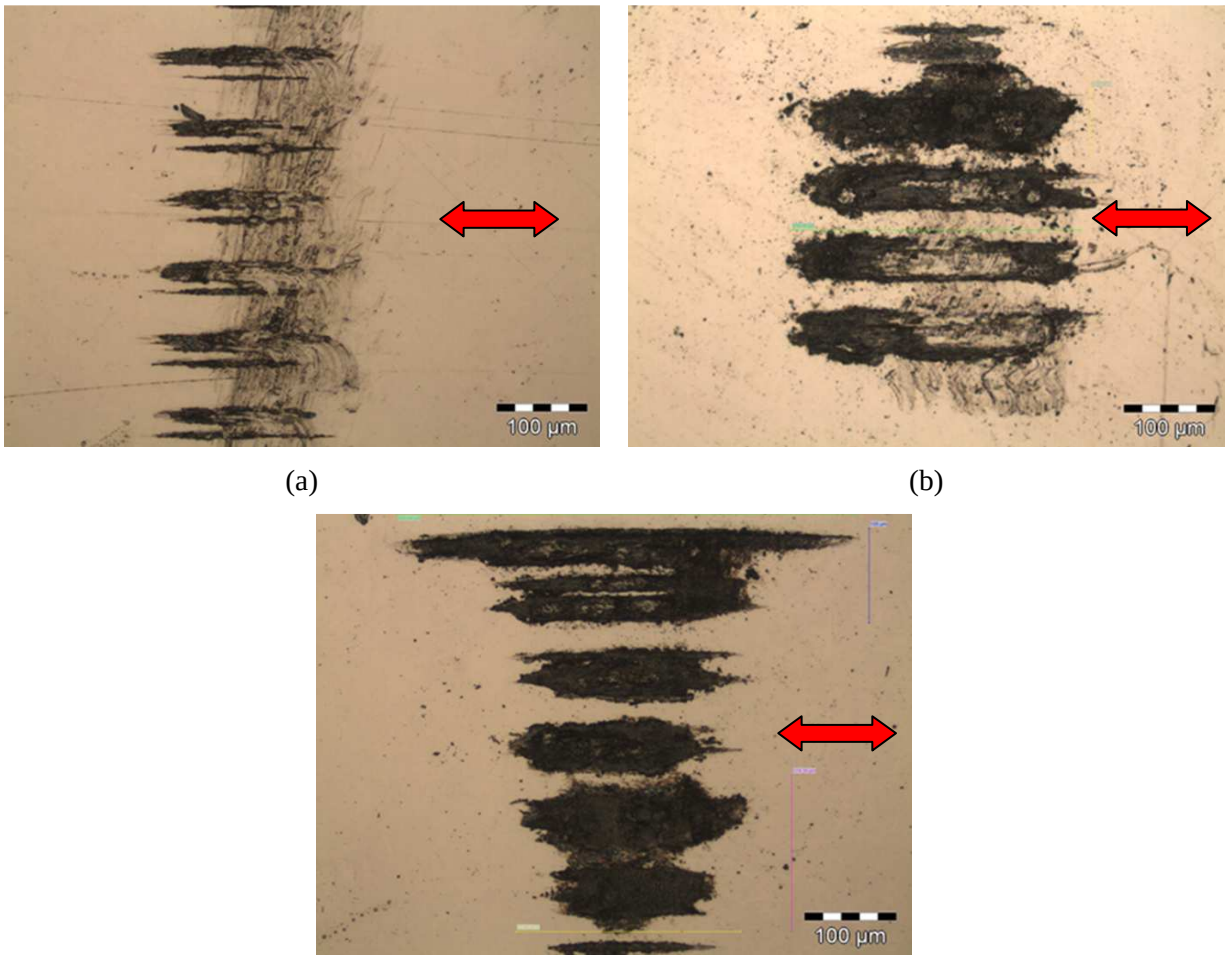

(a) (b)

(c)

Figure 5.7: Optical microscope images of cylinder-on-flat Ti-6Al-4V fretting contacts, subjected to tangential motion and a normal load of: a) 40N; b) 30N; c) 20N, for 2×10^5 fretting cycles

5.2.2 Cylinder-on-Flat Contact Subjected to Axial Motion

Upon the completion of the fretting wear experiments for the Ti-6Al-4V cylinder-on-flat fretting contact subjected to axial motion, the coefficient of static friction for the 2×10^5 cycle experiments were also calculated. Figure 5.8 provides the coefficient of static friction graphs for this set of experiments.

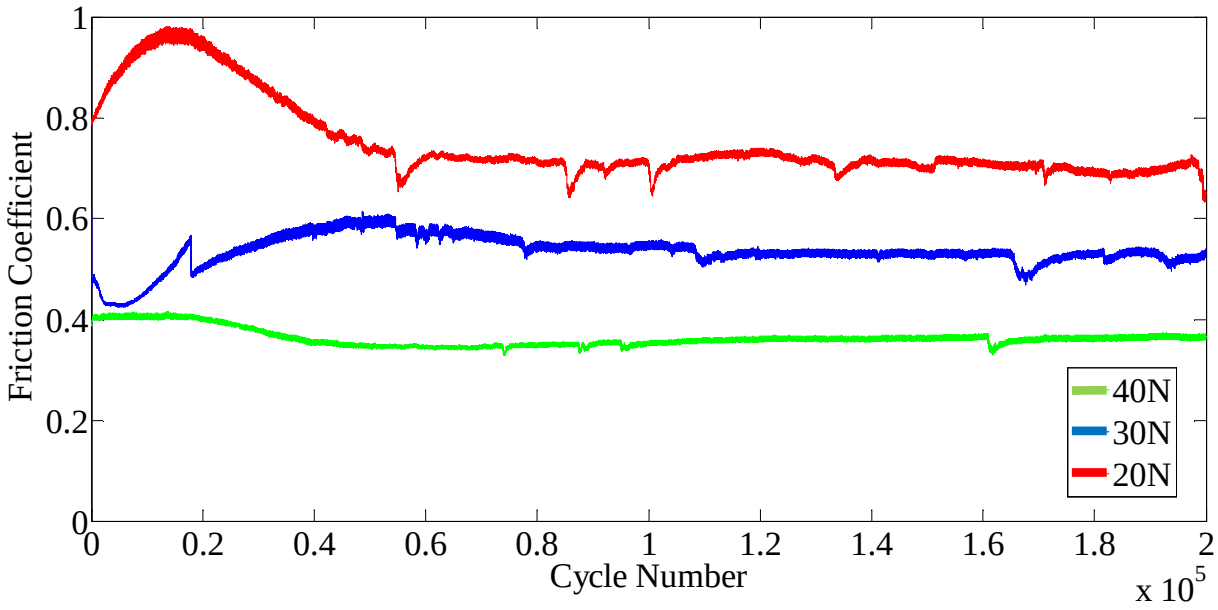

Figure 5.8: Coefficient of friction for Ti-6Al-4V cylinder on Ti-6Al-4V flat subjected to axial motion [Frequency = 80Hz, Slip (peak-to-peak) = 100 µm; Cycles = 2×10^5]

Form the figure it is clear that all three experiments reached a peak friction coefficient value within the first 10^5 cycles. After the peak value was reached the friction coefficients of all three experiments decreased to a fairly stable value, still producing slight variations. From the figure it is evident that the coefficient of static friction was increased by a decrease in the normal force, at the fretting interface. The difference between the peak value and the steady state value observed for the 20N experiment was large, compared to the other two experiments. This accentuates the effect of the lower normal force on the friction at the contact interface.

From the shape of all three the graphs provided in Figure 5.8 it seems that most of the wear and interaction occurred at the start of each experiment. It seems that during this aggravated wear stage enough wear debris accumulates in order to self lubricate the contact. At this stage the wear phenomenon will normally change from conventional two-body wear to three body wear, with the accumulated wear debris forming the third body in the middle of the contact. It is possibly this phenomenon that caused the drop in the coefficient of static friction that as observed for all three experiments. The optical microscope images of the three wear scars are provided in Figure 5.9.

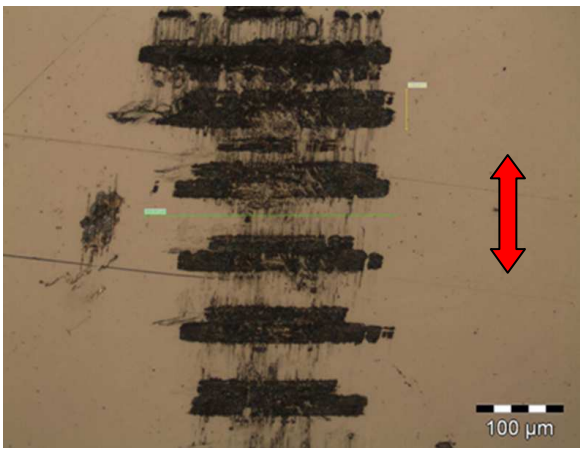

(a)

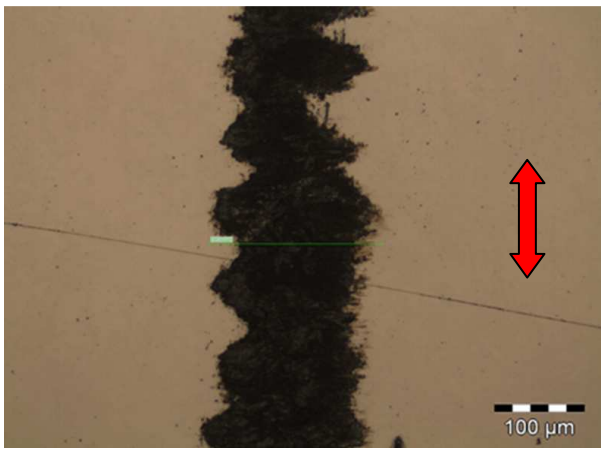

(b)

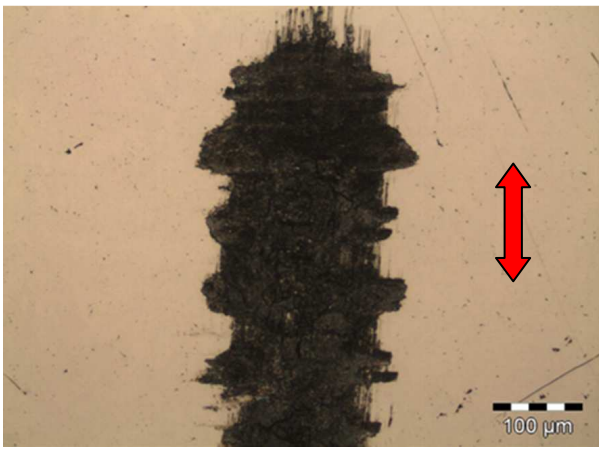

(c)

Figure 5.9: Optical microscope images of cylinder-on-flat Ti-6Al-4V fretting contacts, subjected to axial motion and a normal load of: a) 40N; b) 30N; c) 20N, for 2×10^5 fretting cycles

The wear scars in Figure 5.9 also seem to be small scratch mark in the direction perpendicular to the direction of the fretting motion, indicated by the red arrows. By comparing the three images in the figure it becomes clear that the area of the wear scar was increased by a decrease in the normal force. The wear scar produced by the 40N normal load looks almost similar to the wear scars of the previous set of experiments discussed in Section 5.2.1. Decreasing the normal load from 40N to 30N produced a continuous wear scar, with no gaps or individual scratch marks. From the figure it is also clear that the wear scar produced by the 20N normal load is the most severe of the three, in terms of area. This information, along with the information from the coefficient of static friction in Figure 5.8 revealed that:

> *The fretting wear of the cylinder-on-flat Ti-6Al-4V fretting contacts, subjected to axial motion was increased by a decrease in the normal force.*

5.2.3 Flat-on-Flat Contact

The experiments conducted for the flat-on-flat fretting contact configuration produced similar results compared to the first two sets of experiments, with the coefficient of static friction graphs provided Figure 5.10.

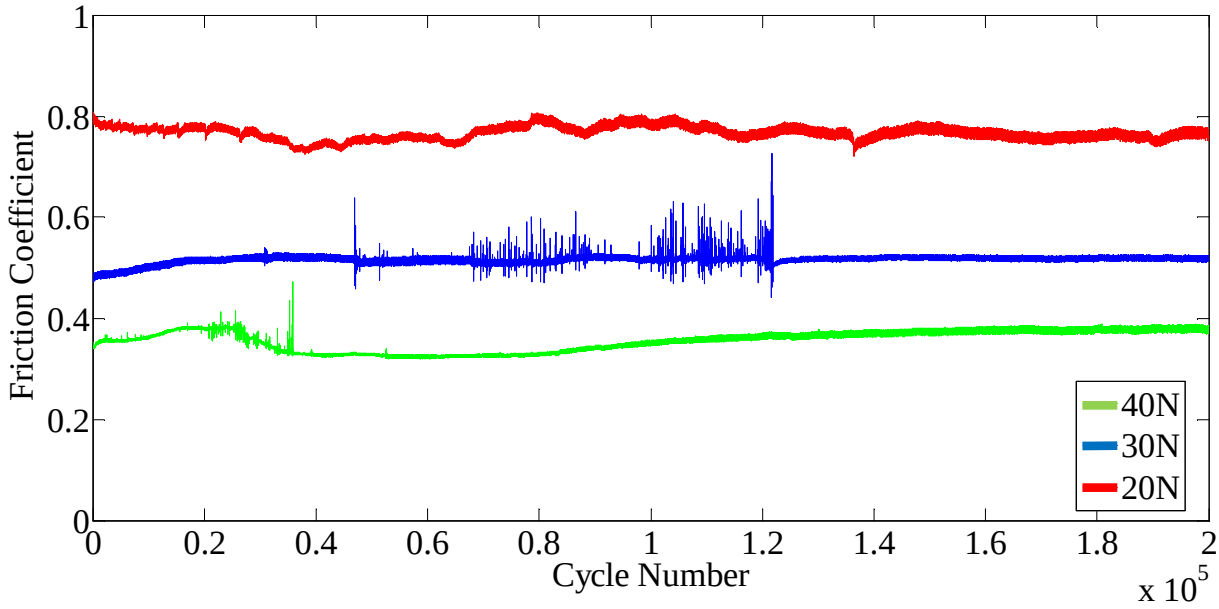

Figure 5.10: Coefficient of friction for Ti-6Al-4V cylinder on Ti-6Al-4V flat subjected to axial motion [Frequency = 80Hz, Slip (peak-to-peak) = 100 µm; Cycles = 2×10^5]

From the figure it is apparent that a steady state in the coefficient of static friction of all three experiments was reached much faster than in the other two sets of experiments. It is also clear the coefficient of static friction was increased by a decrease in the normal force. The optical microscope images of the wear scars are provided in Figure 5.11.

Once again the red arrows in Figure 5.11 indicate the direction of the fretting motion. From the figure it is also apparent that the wear scar area was increased by a decrease in the normal force. This information is supported by the coefficient of static friction graphs in Figure 5.10. Combining the information from Figure 5.10 and Figure 5.11 revealed the following:

> *The fretting wear of flat-on-flat Ti-6Al-4V fretting contact, was increased by a decrease in the normal force.*

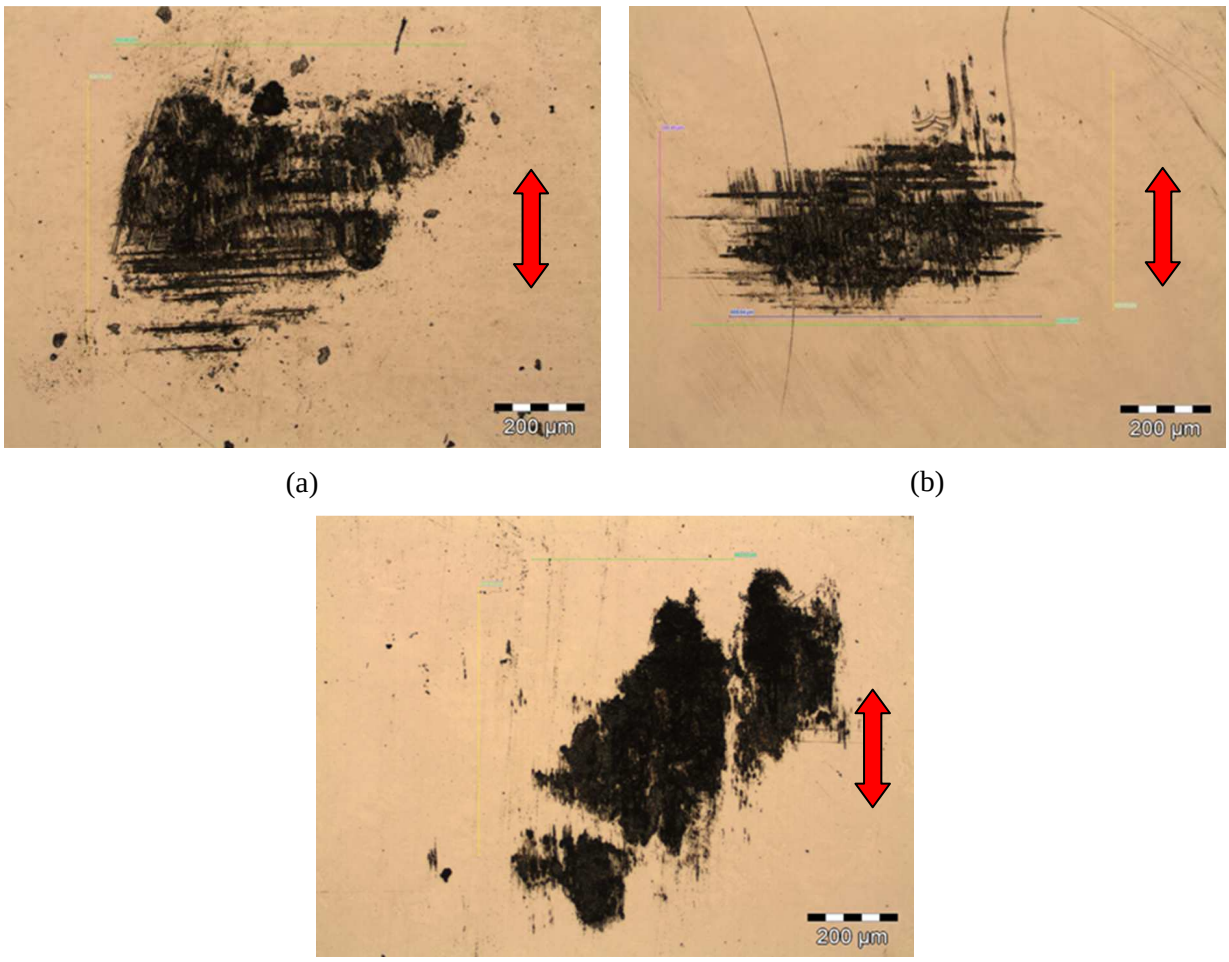

(a) (b)

(c)

Figure 5.11: Optical microscope images of flat-on-flat Ti-6Al-4V fretting contacts subjected to a normal load of: a) 40N; b) 30N; c) 20N, for 2×10^5 fretting cycles

The results of the three sets of experiments correspond to result found in a study conducted by Shen [**66**]. During this study the fretting wear behaviour of greased steel wires was investigated. According to the results the friction coefficient at the contact interface of the greased steel wires was also increased by a decrease in the normal force.

5.2.4 Extended Fretting Wear Experiments

In order to complete the experimental procedure presented in Figure 5.5, the most severe fretting wear cases for each contact configuration needed to be identified by analysing the results from each contact. The analysis revealed that the fretting wear encountered at a normal load of 20N was the worst for all three fretting contacts.

The first extended (10^6 cycle) fretting wear experiment conducted was the cylinder-on-flat Ti-6-Al-4V fretting contact subjected to tangential fretting motion, and a normal force of 20N. The coefficient of static friction graph of this experiment is provided in Figure 5.12. Unfortunately the computer used to capture the

data was only capable of capturing data for a maximum of 2×10^5 cycles at a time, before the data had to be saved. The time needed to save the data corresponded to the time taken to complete 25000 fretting cycles. This is the reason for the four gaps in the graph provided in Figure 5.12.

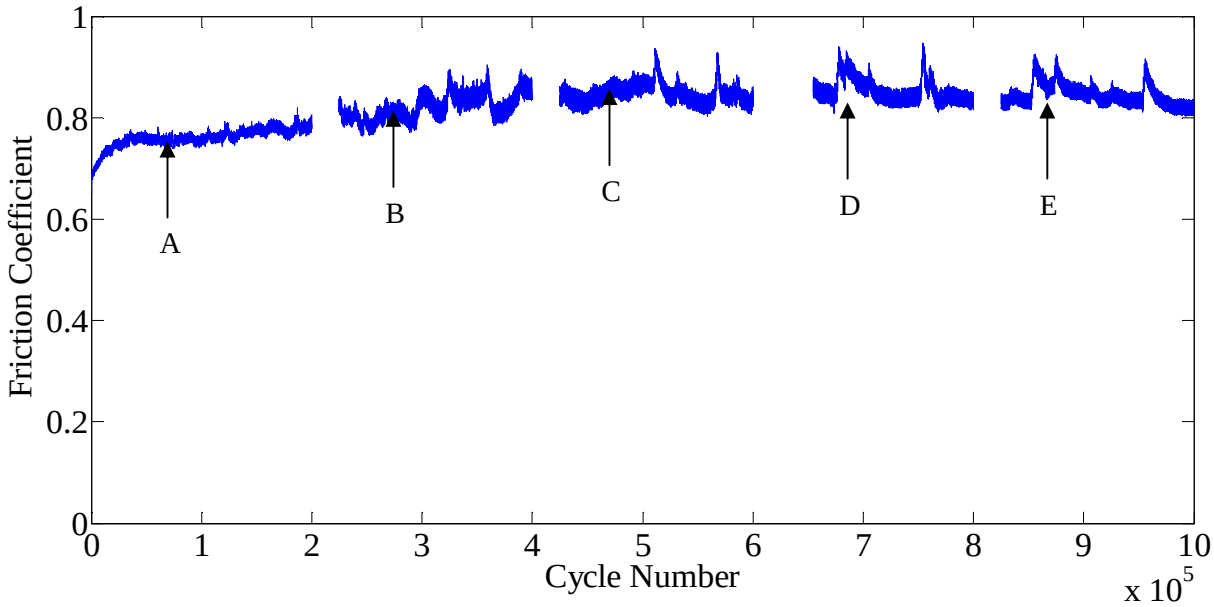

Figure 5.12: Coefficient of friction for Ti-6Al-4V cylinder on Ti-6Al-4V flat subjected to tangential motion [Frequency = 80Hz, Slip (peak-to-peak) = 100 µm; Cycles = 10^6]

The first 2×10^5 cycles of the graph in Figure 5.12 are similar to the 20 N graph provided in Figure 5.6. Both of these graphs start of a value close 0.7 and steadily rise to value of 0.8, with no spikes or extreme variations. This provides a clear indication relating to the repeatability of the fretting test apparatus as well as the experimental procedure. After 2×10^5 cycles the friction coefficient becomes less stable, producing several small peaks. One reason for the slight variations after 2×10^5 cycles might be that the three body wear particles, produced during the initial fretting cycles are trapped within the wear track. These trapped particles may have been acting as solid lubricant, ensuring that the coefficient never rises very far above the 0.8 value for very long. It is however important to note that these trapped particles consist of oxidized wear debris, interacting with both of the Ti-6Al-4V surfaces. Some of these debris might have been relatively large compared to the contact surface, and had to be broken into smaller debris by the fretting process. It is this additional interaction that might be the reason for the spikes in the coefficient of friction after the first 2×10^5 cycles.

Figure 5.13 provides the five tangential/friction force versus slip amplitude graphs for the fretting cycles at points A, B, C, D and E in Figure 5.12. These graphs are also known as the hysteresis loops of these respective cycles [**16**]. The first thing to note from Figure 5.13 is that all five the hysteresis loop have the same quasi-rectangular shape. According to numerous authors [**32**,**16**] this quasi-rectangular shape is an indication of gross slip, and subsequently fretting wear. This evidence provides the first clear indication that the developed fretting test apparatus was indeed functioning according to specification, and is able to produce gross slip.

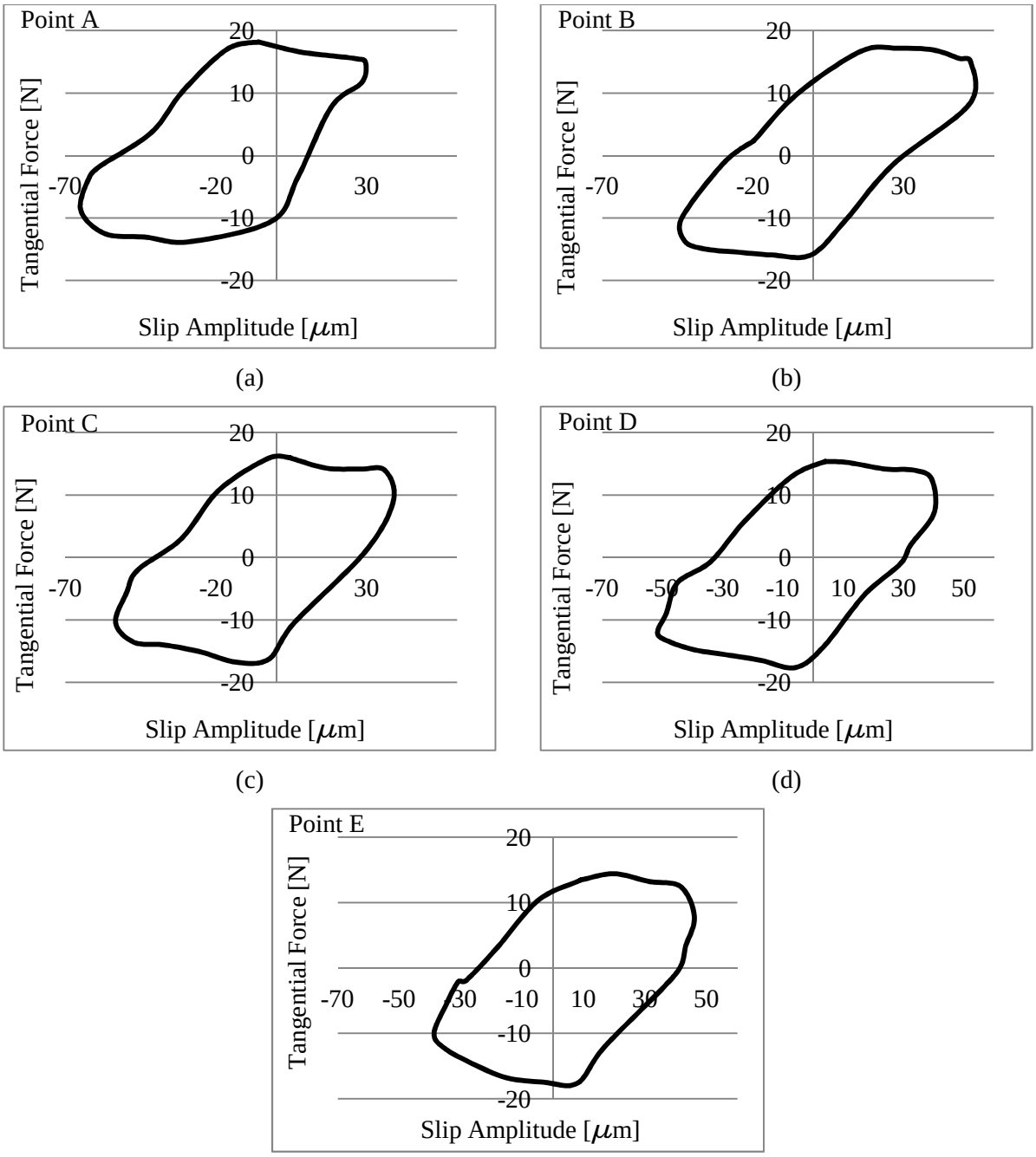

Figure 5.13: Tangential force versus slip amplitude for the cylinder-on-flat Ti-6Al-4V fretting contact subjected to tangential motion, taken at: (a) 10^5 cycles; (b) 3.125×10^5 cycles; (c) 5.125×10^5 cycles; (d) 7.125×10^5 cycles; (e) 9.125×10^5 cycles

It is also important to note that the energy lost by the system is represented by the area within each of the hysteresis loops [**16**]. This loss of energy is thus primarily due to friction. By considering Figure 5.13 as well as Figure 5.12 it was assume that the most severe interfacial interaction and energy loss occurred between cycle 2×10^5 and cycles 8×10^5.

All the fretting wear scars of the extended part of the experimental study were evaluated using a ZEISS EVO MA15 scanning electron microscope (SEM). Figure 5.14 provides the SEM image of the wear scar of the Ti-6Al-4V flat specimen. The red arrow in the figure indicates the direction of the fretting motion. From the figure it is evident that the width of the wear scar decreases from the top to the bottom of the image. The reason for this is that one of the flat ends of the Ti-6Al-4V cylinder was located at the bottom of the wear scar. The bottom of the wear scar thus represents one of the edges of the fretting contact region.

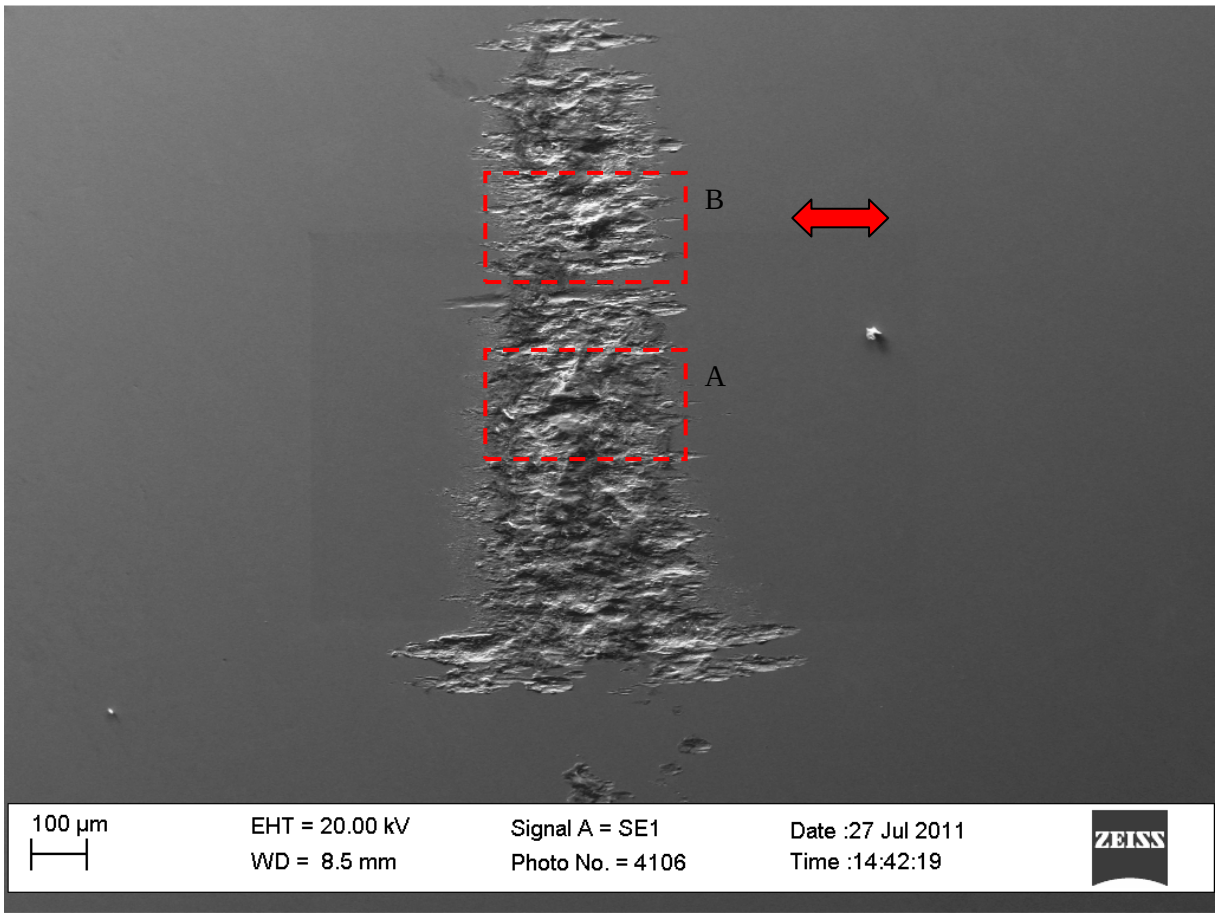

Figure 5.14: SEM image of the wear scar on the flat Ti-6Al-4V specimen produced by the cylinder-on-flat Ti-6Al-4V fretting contact subjected to tangential motion

Severe plastic deformation of the flat surface is also visible in the direction of the fretting motion. Area A and area B depicted by the two dashed red boxes in Figure 5.14 represent two areas of interest that were identified. In order to gain more insight into the wear mechanisms involved, the SEM was used in order to evaluate these two areas of interest even further. The Magnified SEM images of area A and area B are provided in Figure 5.15(a) and Figure 5.16(a) respectively. A quantitative EDX (energy dispersive X-ray spectroscopy) analysis was also performed on the magnified wear scar images in Figure 5.15(a) and Figure 5.16(a). The results of the analysis are provided in Figure 5.15(b) and Figure 5.16(b). The function of the Quantitative EDX analysis is to calculate percentage of each chemical element present in the SEM image, with respect to the total area of the image.

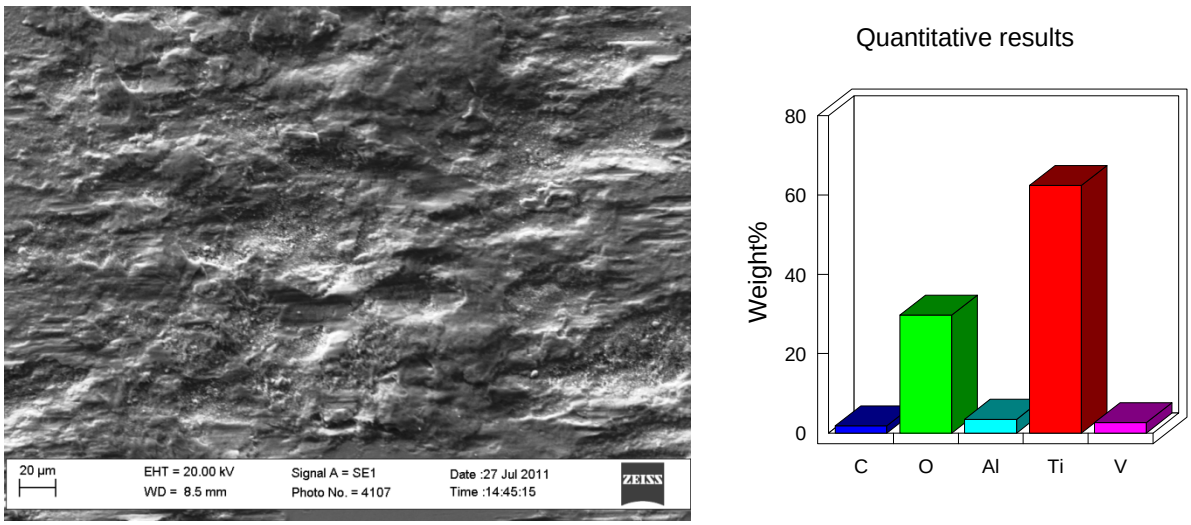

(a) (b)

Figure 5.15: SEM image and EDAX analysis results taken at area A in Figure 5.14: (a) SEM image; (b) quantitative EDX analysis from image

From the evaluation of the SEM image in Figure 5.15(a) it was concluded that this part of the wear scar was predominantly subjected to abrasive wear mechanisms, because it is clear the a large degree of plastic deformation had taken place. Consequently the wear scar consists of numerous asperities that have been sheared off as a result of the gross slip. The numerous dark patches in the wear scar also indicate that material was removed from the surface. Material removal was however not the net result of the wear mechanism. The EDX analysis of the image, provided in Figure 5.15(b), reveals that a large area of the wear scar area consists of oxygen (O). This is because of the rapid oxidation associated with fretting wear [**15**].

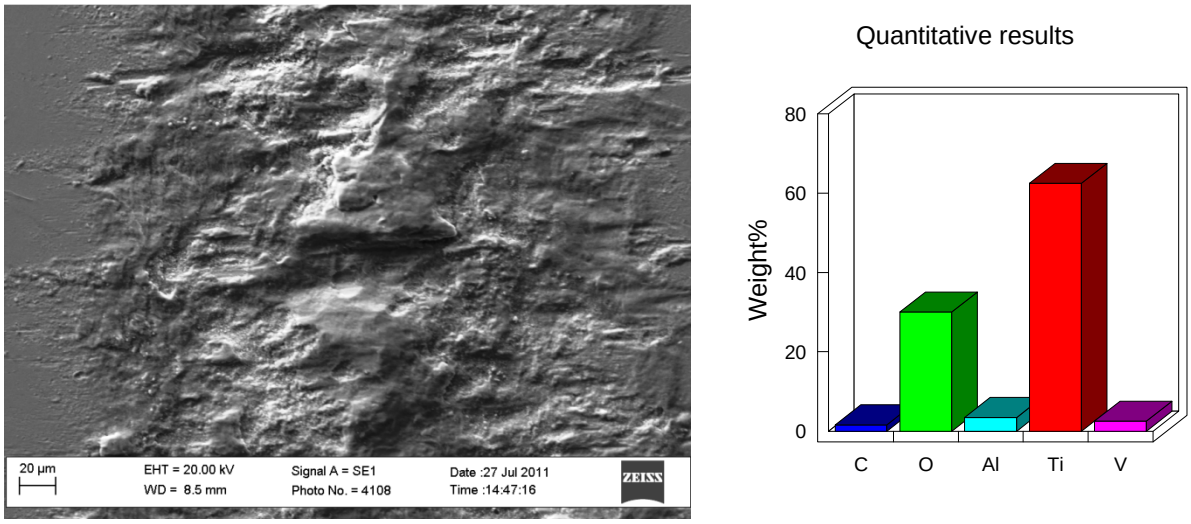

(a) (b)

Figure 5.16: SEM image and EDX analysis results taken at area B in Figure 5.14: (a) SEM image; (b) quantitative EDX analysis from image

The magnified SEM image and EDX analysis of area B produced fairly similar results, compared to the results of area A. The image also indicates that a large amount of plastic deformation had taken place, resulting in large amounts of material removed from the surface. The EDX analysis also revealed that a large degree of oxidation had taken place. Figure 5.16(a) also shows that material transfer had taken place between the cylinder and the flat, resulting in the accumulation of material and wear debris in the middle of the wear scar. Table 5.3 provides a summary of the quantitative EDX analysis performed on the entire wear scar (Figure 5.14) and the two area of interest (Figure 5.15(a) and Figure 5.16(a)).

Table 5.3 Summary of the three quantitative EDX analyses performed on the fretting wear scar of the cylinder-on-flat Ti-6Al-4V fretting contact subjected to tangential motion

	Weight%				
Spectrum	**Ti**	**O**	**Al**	**V**	**Total**
Figure 5.14	90.9783	0	5.3708	3.650898	100
Figure 5.15	62.42727	31.50838	3.475489	2.588871	100
Figure 5.16	62.4772	31.59951	3.409212	2.514073	100

The results of extended cylinder-on-flat Ti-6Al-4V fretting contact subjected to axial motion as well as the flat-on-flat Ti-6Al-4V fretting contact are provided in Section B.1 of APPENDIX B.

5.3 Fretting Wear of Aircraft Structural Joints

This section discusses the investigation of riveted structural joints of aircraft, in terms of fretting wear. The material investigated in this section is the aluminium alloy Al 7075-T6, as discussed in Chapter 3 and Chapter 4. In order to identify possible fretting wear at these joints the same procedure discussed in Section 5.2 was used. Figure 5.17 provides a model of a typical riveted structural joint of an aircraft, providing the possible fretting contact interfaces as well as the fretting motions that can take place at these interfaces.

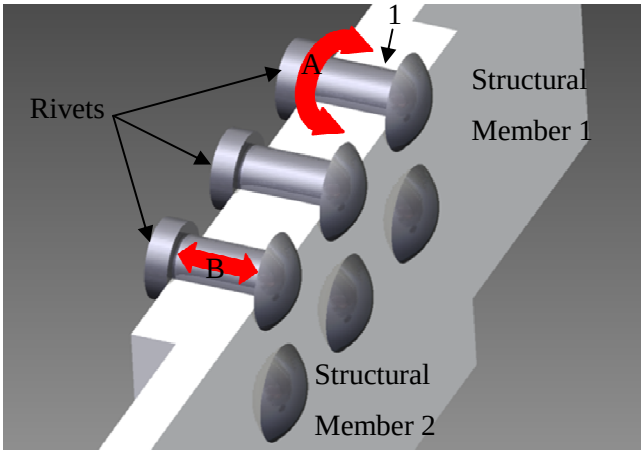

Figure 5.17: Model of the fretting contact interfaces and fretting motions encountered in a typical riveted aircraft structural joint

Evaluating Figure 5.17 reveals one possible fretting contact that can possibly subjected to two different fretting motions. Motion A in the figure represents slight angular motion at contact 1. This possibility can be represented as a cylinder-on-flat fretting contact subjected to tangential motion. The second possibility can be represented as cylinder-on-flat fretting contact subjected to axial motion, represented by motion B in Figure 5.17. For the purpose of the experimental study these two contacts were represented by Figure 5.3(a) and Figure 5.3(b) respectively. The experimental procedure used fo the Al7075-T6 experiments was similar to the procedure discussed for the Ti-6Al-4V experiments. The difference between the two procedures is that only the two fretting contact configurations are present in Figure 5.17.

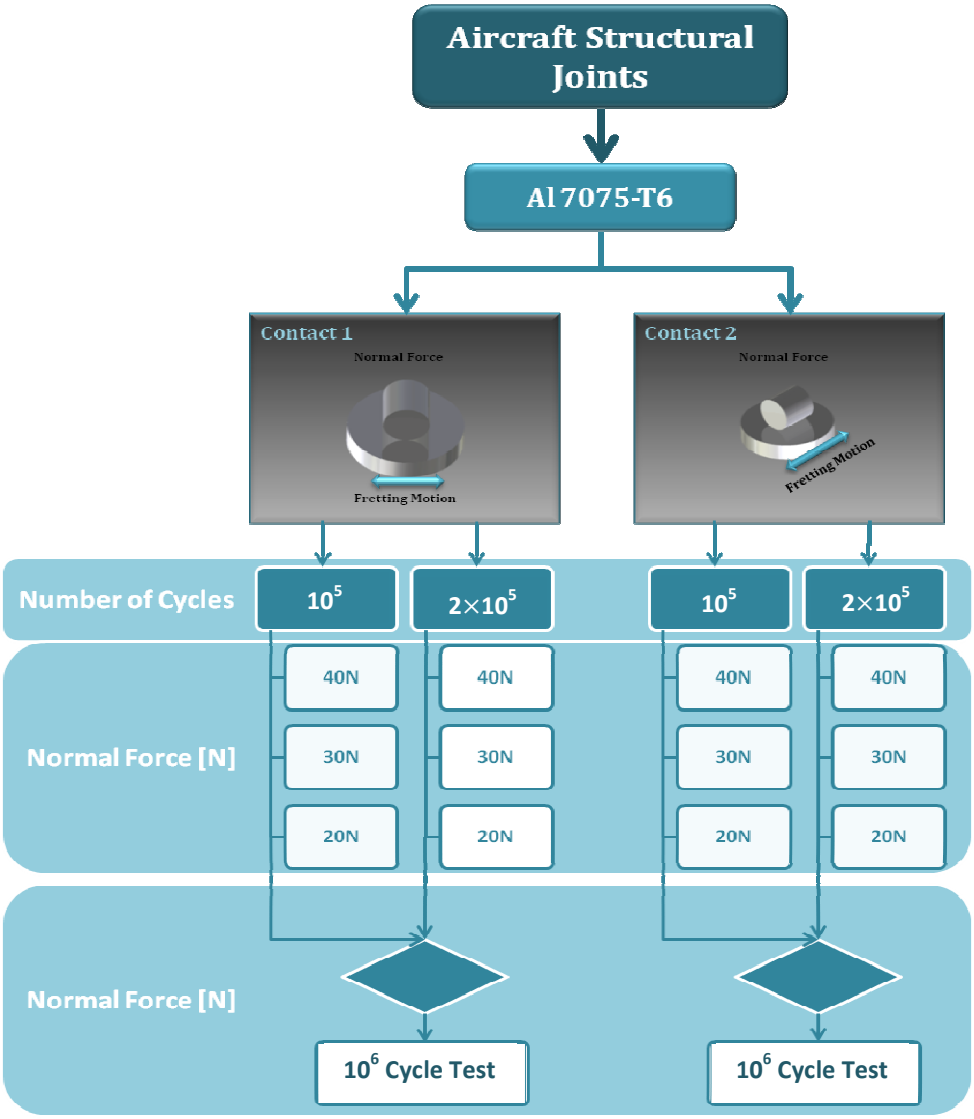

Figure 5.18: Experimental procedure for the Al7075-T6 riveted structural joint application

The mechanical properties and the composition of Al7075-T6 are provided in Table 5.4 and Table 5.5.

Table 5.4: Mechanical properties of Al7075-T6at room temperature [**67**]

Mechanical property	**Al7075-T6**
Hardness [GPa]	1.72
Density [g/cm^3]	2.81
Fracture Toughness [MPa.m$^{1/2}$]	29
Modulus of Elasticity [GPa]	71.7

Table 5.5 Composition of Al7075-T6 [**68**]

Weight%								
Zn	**Mg**	**Cu**	**Fe**	**Si**	**Ti**	**Mn**	**Cr**	**Al**
5.36	2.7	1.6	0.29	0.07	0.05	0.05	0.02	Bal

5.3.1 Cylinder-on-Flat Contact Subjected to Tangential Motion

Figure 5.19 provides the coefficient of static friction graphs of the 2×10^5 cycle fretting wear experiments conducted for Al7075-T6 cylinder-on-flat contacts, subjected to tangential motion. The three graphs in the figure are for the 40N, 30N and 20N experiments respectively. From the figure it is clear that a change in the normal force once again significantly influenced the coefficient of static friction. Accordingly the coefficient of static friction was increased by a decrease in the normal force.

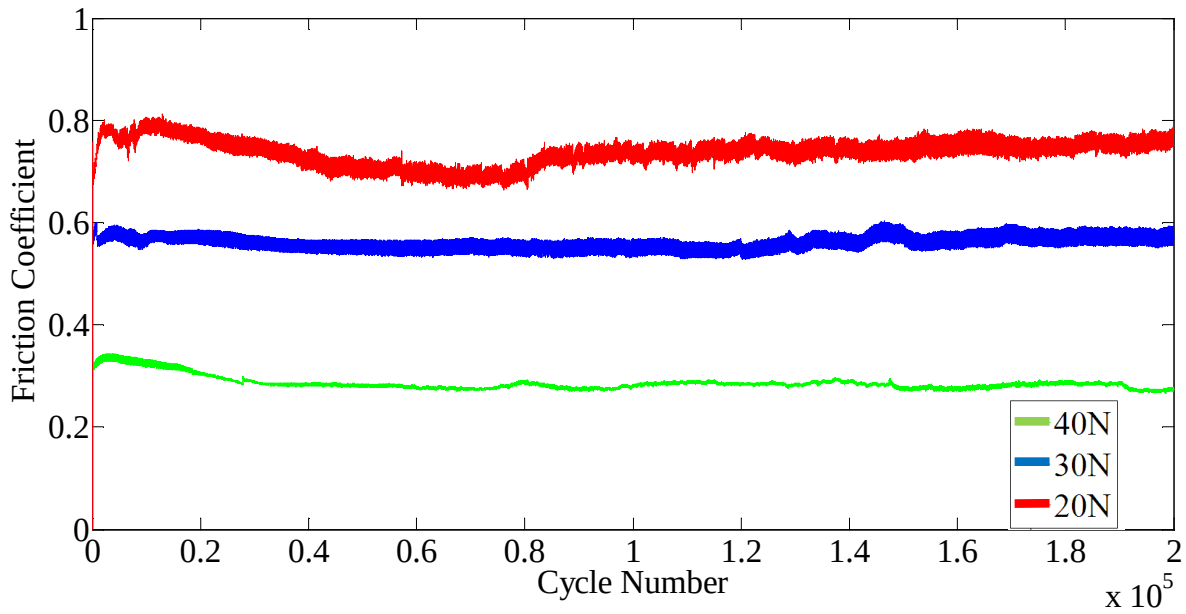

Figure 5.19: Coefficient of friction for Al7075-T6 cylinder on Al7075-T6 flat subjected to tangential motion [Frequency = 80Hz, Slip (peak-to-peak) = 100 µm; Cycles = 2×10^5]

Figure 5.20 provides the optical microscope images of the three fretting wear scars located on the flat test specimens. The red arrows in the figure indicate the direction of the fretting motion. Investigation of the three wear scars revealed that the width and consequently the severity of the wear scars increased with a

decrease in the normal force. Combining this result with the information from the coefficient of static friction graph in Figure 5.19 revealed the following:

> *The fretting wear of cylinder-on-flat Al7075-T6 fretting contacts subjected to tangential motion was increased by a decrease in the normal force.*

This result corresponds to the result concluded form the experiments performed on the Ti-6Al-4V cylinder-on flat fretting contacts, subjected to similar experimental conditions. It is however important to note that the Al7075-T6 wear scars seem more severe in terms of shape, width and discoloration. However, the friction coefficients of Al7075-T6 experiments stabilized at similar values compared to the Ti-6Al-4V experiments. This indicates that the Al7075-T6 fretting contacts produced more severe wear scars than the Ti-6Al-4V fretting contacts, but at similar friction levels.

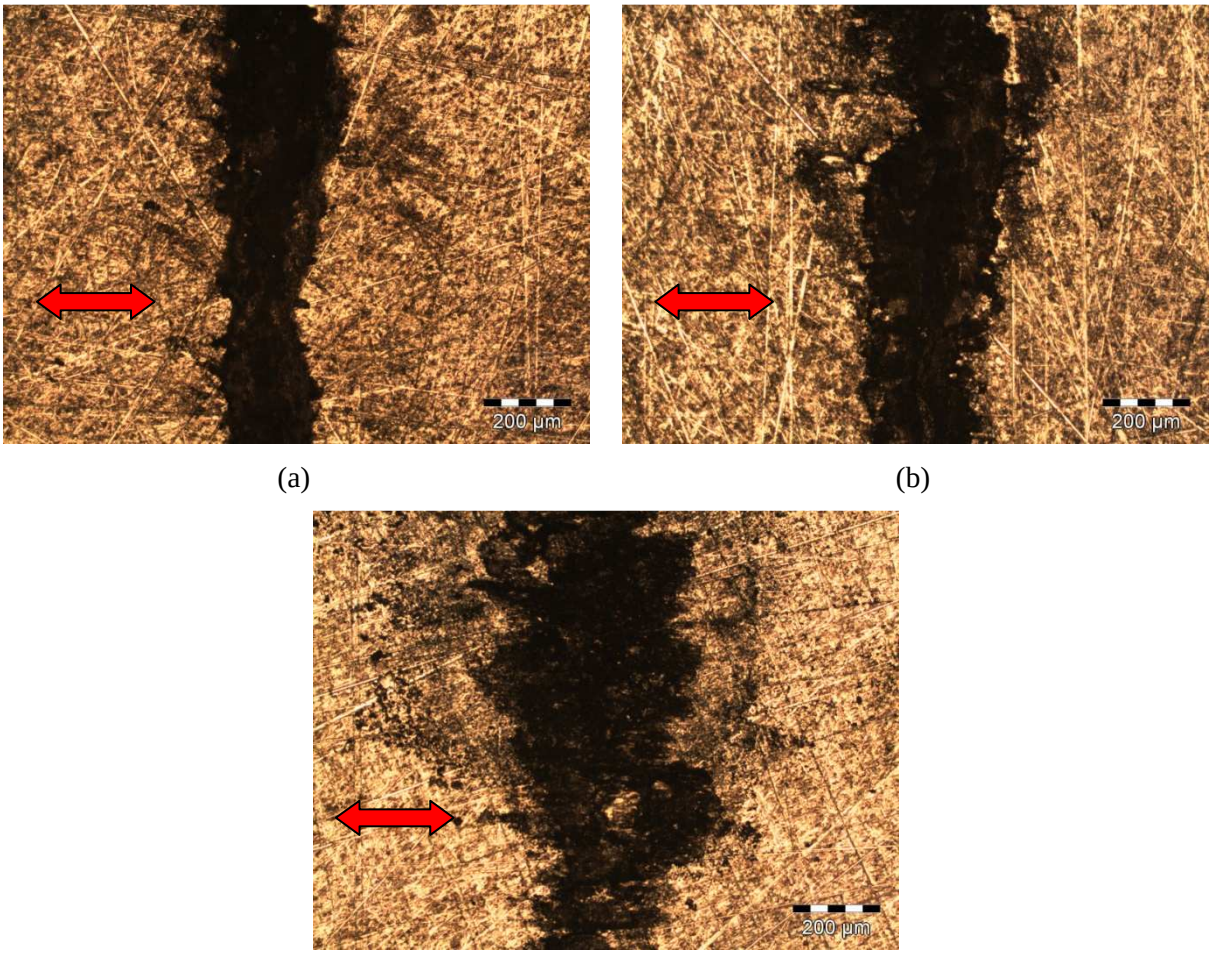

(a) (b)

(c)

Figure 5.20: Optical microscope images of cylinder-on-flat Al7075-T6 fretting contacts, subjected to tangential motion and a normal load of: a) 40N; b) 30N; c) 20N, for 200000 fretting cycles

5.3.2 Cylinder-on-Flat Contact Subjected to Axial Motion

Upon the completion of the fretting wear experiments for the AL7075-T6 cylinder-on-flat fretting contacts subjected to axial motion, the coefficient of static friction for the 2×10^5 cycle experiments were also calculated. The three graphs of the friction coefficients are provided in Figure 5.21. From the figure it is once again apparent that the coefficient of friction was increased by a decrease in the normal load.

The optical microscope images of the wear scars located on the flat test specimens are provided in Figure 5.22, with the red arrows in the figures indicating the direction of the fretting motion. The images also revealed that the width and consequently the severity of the wear scars were increased by a decrease in the normal force. The reason for this is that more asperity interaction and slip had taken at the lower normal force, allowing more asperity contacts to be broken and consequently resulting in more severe wear scars. Combining this result with the information from the coefficient of static friction graph in Figure 5.21 revealed the following:

> *The fretting wear of cylinder-on-flat Al7075-T6 fretting contacts, subjected to axial motion was increased by a decrease in the normal force.*

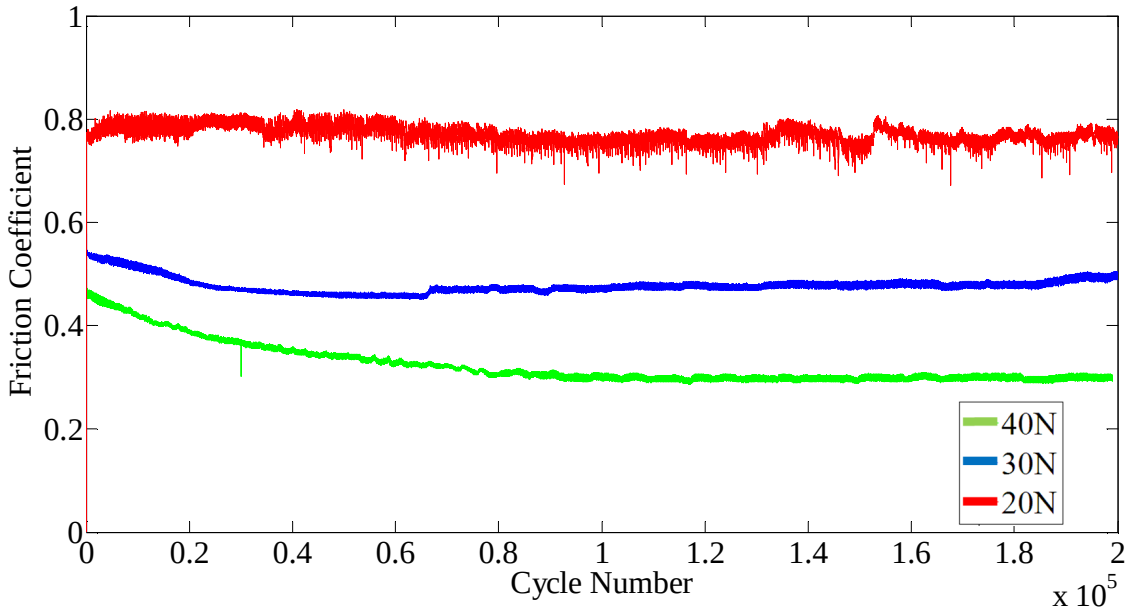

Figure 5.21: Coefficient of friction for Al7075-T6 cylinder on Al7075-T6 flat subjected to axial motion [Frequency = 80Hz, Slip (peak-to-peak) = 100 µm; Cycles = 2×10^5]

Comparing the Al7075-T6 wear scars in Figure 5.21 with the Ti-6Al-4V wear scars in Figure 5.9 also indicates that the Al7075-T6 fretting contact produced more severe wear scars in terms of shape, width and discoloration. A comparison between the static friction coefficient graphs of both sets of experiments also revealed the fairly similar steady state friction coefficients were produced. This once again indicates that the Al7075-T6 fretting contacts produced more severe wear scars than the Ti-6Al-4V fretting contacts, at similar friction levels.

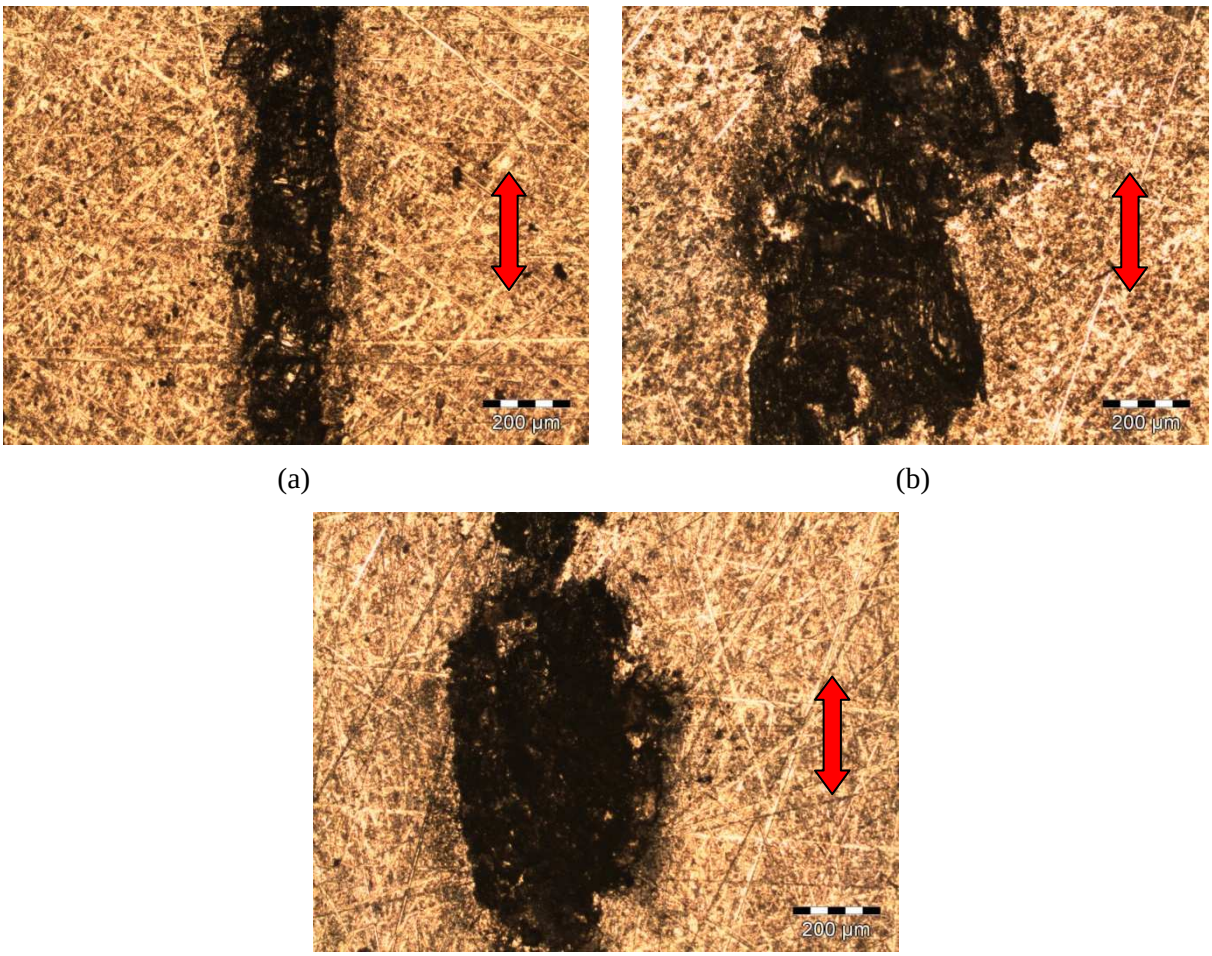

(a) (b)

(c)

Figure 5.22: Optical microscope images of cylinder-on-flat Al7075-T6 fretting contacts, subjected to tangential motion and a normal load of: a) 40N; b) 30N; c) 20N, for 2×10^5 fretting cycles

5.3.3 Extended Fretting Wear Experiments

In order to complete the experimental procedure presented in Figure 5.18, the most severe fretting wear cases for each contact configuration were identified by analysing the results from each contact. According to the evaluation the most severe fretting wear and highest friction coefficients were produced by a normal force of 20N for both of the fretting contacts. It was therefore decided to repeat the 20N experiments for both fretting contact configurations for 10^6 cycles. The coefficient of static friction graph of the cylinder-on-flat Al7075-T6 fretting contact, subjected to axial motion is provided in Figure 5.23. The graph is divided is divided into five sets of recorded data, similar to the Ti-6Al-4V graph in Figure 5.12.

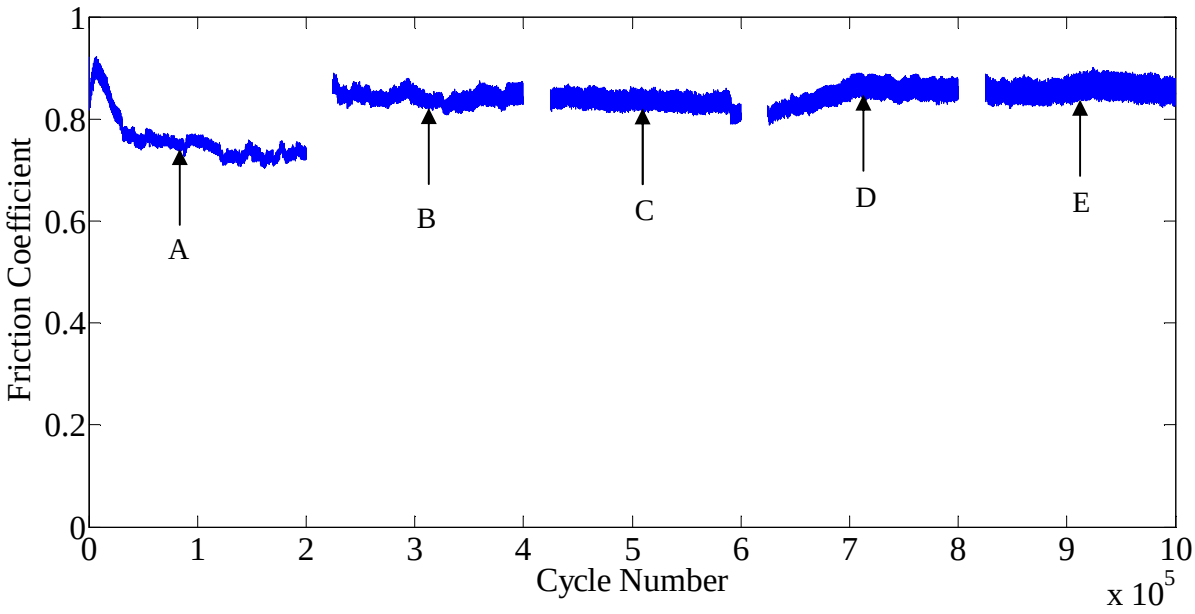

Figure 5.23: Coefficient of friction for cylinder-on-flat AL7075-T6 fretting contact subjected to axial motion [Normal force = 20N, Frequency = 80Hz, Slip (peak-to-peak) = 100 μm; Cycles = 10^6]

During the first 2×10^5 cycles the friction coefficient reached a peak value of 0.92 and the dramatically dropped to a value of 0.74. During the first data saving sequence (between 2×10^5 cycles and 2.25×10^5 cycles) the coefficient rose to a value 0.85, and remained fairly stable for the remainder of the experiment. A possible reason for the sudden increase in the friction coefficient might be that the aluminium oxide wear debris is harder than the aluminium alloy. It is important to note that after the value 0.85 was reached, no considerable spikes in the friction coefficient were observed. This indicates that a friction steady state was reached and it continued for the remainder of the experiment.

Figure 5.24 provides the hysteresis loops for the fretting cycles at points A, B, C, D and E in Figure 5.23. These five loops all have the same quasi-rectangular shape, indicating that gross slip and subsequently fretting wear had taken place. This can however only be confirmed by using SEM analysis in order to investigate the wear scar in detail.

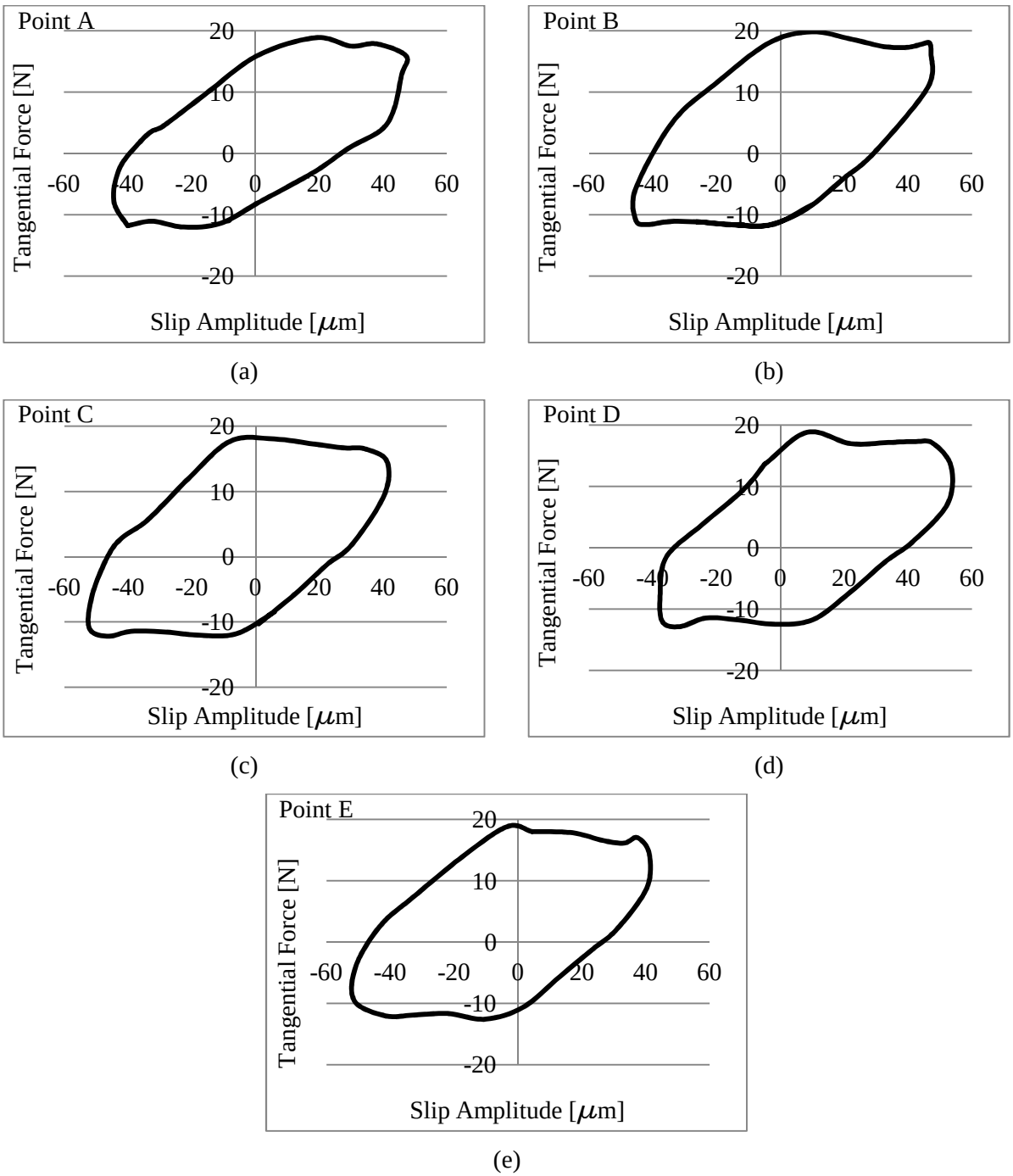

Figure 5.24: Tangential force versus slip amplitude for the cylinder-on-flat Al7075-T6 fretting contact subjected to axial motion, taken at: a) 10^5cycles; (b) 3.125×10^5 cycles; (c) 5.125×10^5 cycles; (d) 7.125×10^5 cycles; (e) 9.125×10^5 cycles

According to the information provided in Figure 5.24 it is clear the lowest tangential/friction force and slip amplitude values were recorded at point A in Figure 5.23, corresponding to the lowest recorded friction coefficient. The hysteresis loop of the cycle at point A is also the smallest of the five loops in Figure 5.24. This indicates that the least amount of friction energy was dissipated during this stage of the experiment [**16**]. The hysteresis loops for the rest of the experiment remained fairly similar, indicating that a relatively constant amount of friction energy was dissipated.

Figure 5.25 provides the SEM image of the wear scar of the Al7075-T6 flat specimen. The red arrow in the figure indicates the direction of the fretting motion. The wear scar indicates that severe plastic deformation had taken place at the contact interface. In order to gain more insight into the nature of the deformation two areas of interest on wear scar were identified. These two areas are depicted by area A and area B, enclosed by the dashed red boxes in the figure.

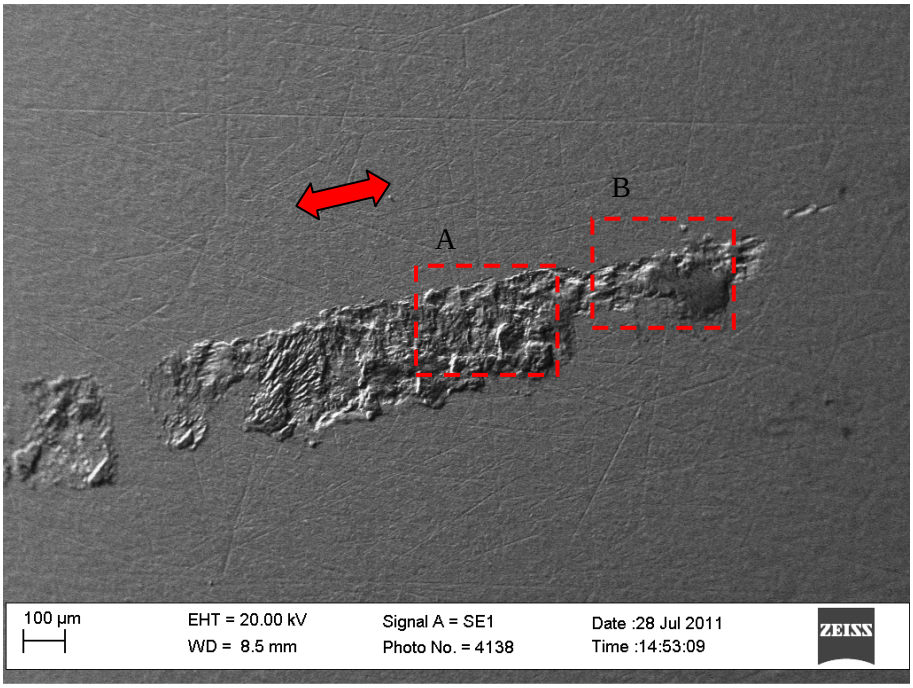

Figure 5.25: SEM image of the wear scar on the flat Al7075-T6 specimen produced by the cylinder-on-flat Al7075-T6 fretting contact subjected to axial motion

Figure 5.26 provides the magnified SEM image of area A as well as the quantitative EDX analysis of this image. The surface in the image was subjected so sever plastic shearing. Numerous craters of varying sizes are visible where material was removed in the form of wear debris. The quantitative EDX analysis indicates that the surface contains nearly the same amount of oxygen as aluminium. It is therefore safe to deduce that large degree of oxidation had taken place. The topography of surface also indicates that some material was added to the wear scar. This might be as a result of the third body material that was trapped within the contact during the experiment. The high temperature caused by friction, as well as the adhesive nature of the fretting wear mechanism might have caused some of the third body material to adhere to the wear scar. The third body material encountered during fretting wear will usually consists of accumulated oxide debris, causing high levels of oxygen to be observed at the contact interface.

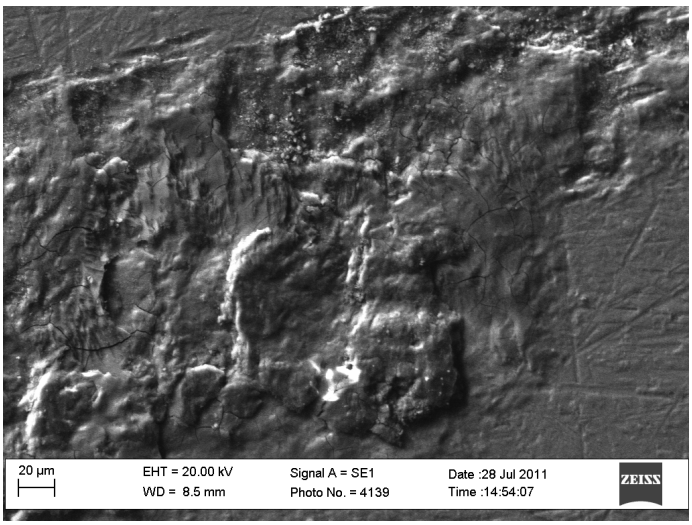

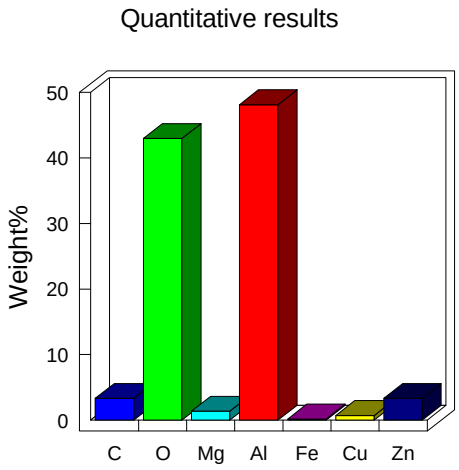

(a) (b)

Figure 5.26: SEM image and quantitative EDX analysis of area A in Figure 5.25: (a) SEM image; (b) quantitative EDX analysis from image

The magnified SEM image and quantitative EDX analysis of area B are provided in Figure 5.27. From the image extensive plastic deformation is also visible, especially towards the edge of the wear scar. The wear scar also indicates that material had been added at several points throughout the scar. In the bottom half of the wear scar small cracks are visible. This part of the wear scar also shows signs of delamination, causing the part of the surface to dislocate as a result of the propagation of the several small surface cracks.

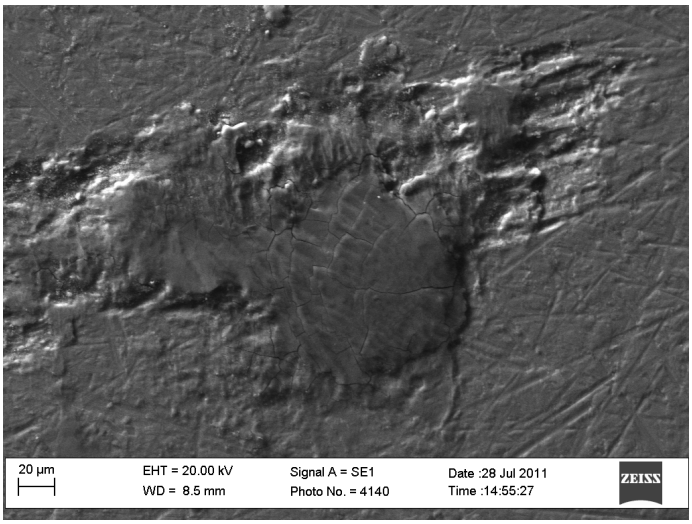

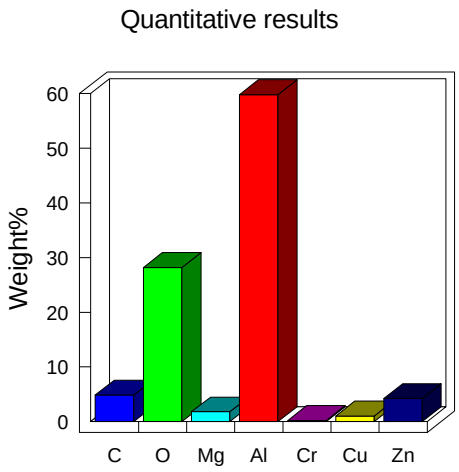

(a) (b)

Figure 5.27: SEM image and quantitative EDX analysis of area B in Figure 5.25: (a) SEM image; (b) quantitative EDX analysis from image

Table 5.6 provides a summary of the two quantitative EDAX analyses provided in

Table 5.6: Summary of the quantitative EDX analyses in Figure 5.26 and Figure 5.27.

	Weight%							
Figure	**Al**	**O**	**C**	**Zn**	**Mg**	**Cu**	**Cr**	**Total**
Figure 5.26	48.125	42.981	3.315	3.318	1.355	0.7186	0.1875	100
Figure 5.27	59.779	28.185	4.829	4.196	1.787	1.019	0.20499	100

The results of extended cylinder-on-flat Al7075-T6 fretting contact subjected to tangential motion are provided in Section B.2 of APPENDIX B.

5.4 Cemented Carbides

Cemented carbides are a group of extremely had and wear-resistant refractory composite materials, consisting of hard carbide particles bound together by a ductile and tough metallic binder matrix [**69**]. Tungsten carbide (WC) is one the most commonly used cemented carbides in industry, while the metallic binder used will usually consist of cobalt (Co), nickel (Ni) or iron (Fe). The combination of toughness, hardness and wear resistance provided by cemented carbides explains the extensive use of these composites in applications where excellent mechanical properties and tribological characteristics are required. These applications include high speed cutting tools, punches, dies, forming tools and machine parts to only name a few [**69**,**70**].

The endurance, mechanical and environmental requirements of aerospace contact applications exceeds the limits of available lubrication and wear-reduction technologies [**71**]. Advances in the field of tribology have however produced carbides that exhibit low friction, low wear and high hardness [**72**]. WC-Co cemented carbides have been used in jet engines as coatings for parts such as fans and high pressure compressors [**73**]. The WC-Co coatings are very efficient in applications involving metal alloys, in particular titanium alloys, because of the following:

- The high wear resistance of the tungsten carbide.
- Adequate fracture toughness provided by the cobalt binder matrix.
- The high adherence of the coatings on the titanium substrates.

The WC-Co coatings also retain low-temperature ductility, including high temperature oxidation resistance over the large temperature range, experienced in aerospace applications. For these reasons it was decided to include the fretting wear investigation of cemented carbides in this study. This section is therefore aimed at investigating the fretting wear behaviour of cemented carbides in the same two aerospace applications discussed in section 5.2 and section 5.3.

5.4.1 Conventionally Sintered Cemented Tungsten Carbide

The conventionally sintered cemented tungsten carbide used for the fretting wear experiments was WC-10wt%Co. This material was used as flat test specimens in all the conducted fretting wear experiments. The reason for this is the fact that cemented carbides are extremely difficult to machine, and flat disk like specimens were the easiest to manufacture. These carbides are so difficult to machine that Electron Discharge Machining (EDM) is used for this purpose. The mechanical properties a of WC-10wt%Co at room temperature are provided in Table 5.7.

Table 5.7: Mechanical properties of WC-10wt%Co at room temperature

Mechanical property	**WC-10wt%Co**
Density [g/cm^3]	14.57±0.4
Hardness [GPa]	16.96±0.21
Fracture Toughness [Mpa.m$^{1/2}$]	9.87±0.01

The WC-10wt%Co flat specimens were involved in five extended fretting wear experiments. The experimental parameters of these five experiments were exactly the same as for extended Ti-6Al-4V and Al7075-T6 experiments. Table 5.8 provides a summary of all the materials involved, as well as the contact conditions of these five experiments.

Table 5.8: Summary of the WC-10wt%Co fretting experiments

Experiment number	**Specimen 1**	**Specimen 2**	**Motion**
1.1	WC-10wt%Co flat	Ti-6al-4V cylinder	Tangential motion
1.2	WC-10wt%Co flat	Ti-6al-4V cylinder	Axial motion
1.3	WC-10wt%Co flat	Ti-6al-4V flat	Tangential/axial motion
1.4	WC-10wt%Co flat	Al7075-T6 cylinder	Tangential motion
1.5	WC-10wt%Co flat	Al7075-T6 cylinder	Axial motion

Figure 5.28 provides a graph of the coefficient of static friction for the Ti-6Al-4V cylinder on WC-10wt%Co flat fretting contact subjected to tangential motion.

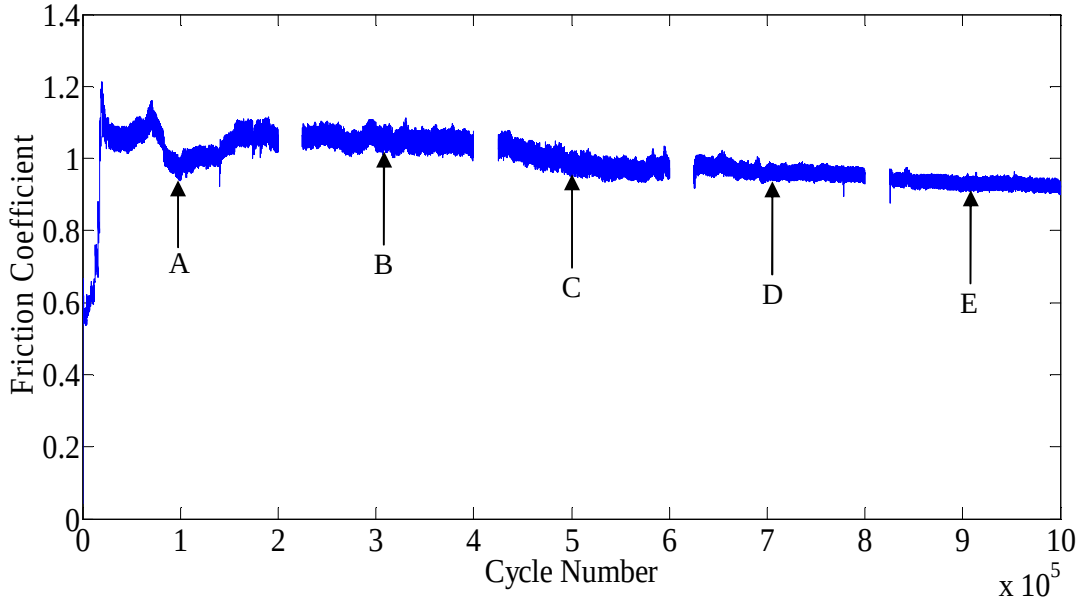

Figure 5.28: Coefficient of friction for a Ti-6Al-4V cylinder on a WC-10wt%Co flat fretting contact subjected to tangential motion [Normal force = 20N, Frequency = 80Hz, Slip (peak-to-peak) = 100 μm; Cycles = 10^6]

From Figure 5.28 it is clear the largest variation in the coefficient of static friction occurred during the first 2×10^5 cycles. The friction coefficient started off at a value of 0.6 at reached a peak value of 1.21 with the first 20000 cycles, after which it decreased to a value of 1.06. The behavior of the coefficient was much less erratic during the final 8×10^5 cycles of the experiment. From the figure it is clear that the coefficient steadily decreased from 1.06 to a value of 09.2, during this period. Comparing Figure 5.28 with any of the friction coefficient graphs previously discussed revealed that the friction during this particular experiment was much higher in comparison. Determining reasons for this from Figure 5.28 is impossible, and therefore additional experimental results were used in order to explain this phenomenon.

Figure 5.29 provides the five hysteresis loops for the fretting cycles at points A, B, C, D and E in Figure 5.28. Even though all five of these loops look a little different, they still all have a quasi-rectangular shape, indicating gross slip and consequently fretting wear. The hysteresis loops indicate that the most friction energy was dissipated during the first 4×10^5 cycles of the experiment. This might have been caused by the occurrence of three body wear. Accordingly the most wear and the highest friction occurred at the start of the experiment, while the asperities of both surfaces were still in contact. As the experiment continued the three body particles resulting from the abrasive wear mechanisms might have separated the asperities of the two surfaces, acting as a solid lubricant. It was therefore decided to attempt to verify this assumption using SEM analysis.

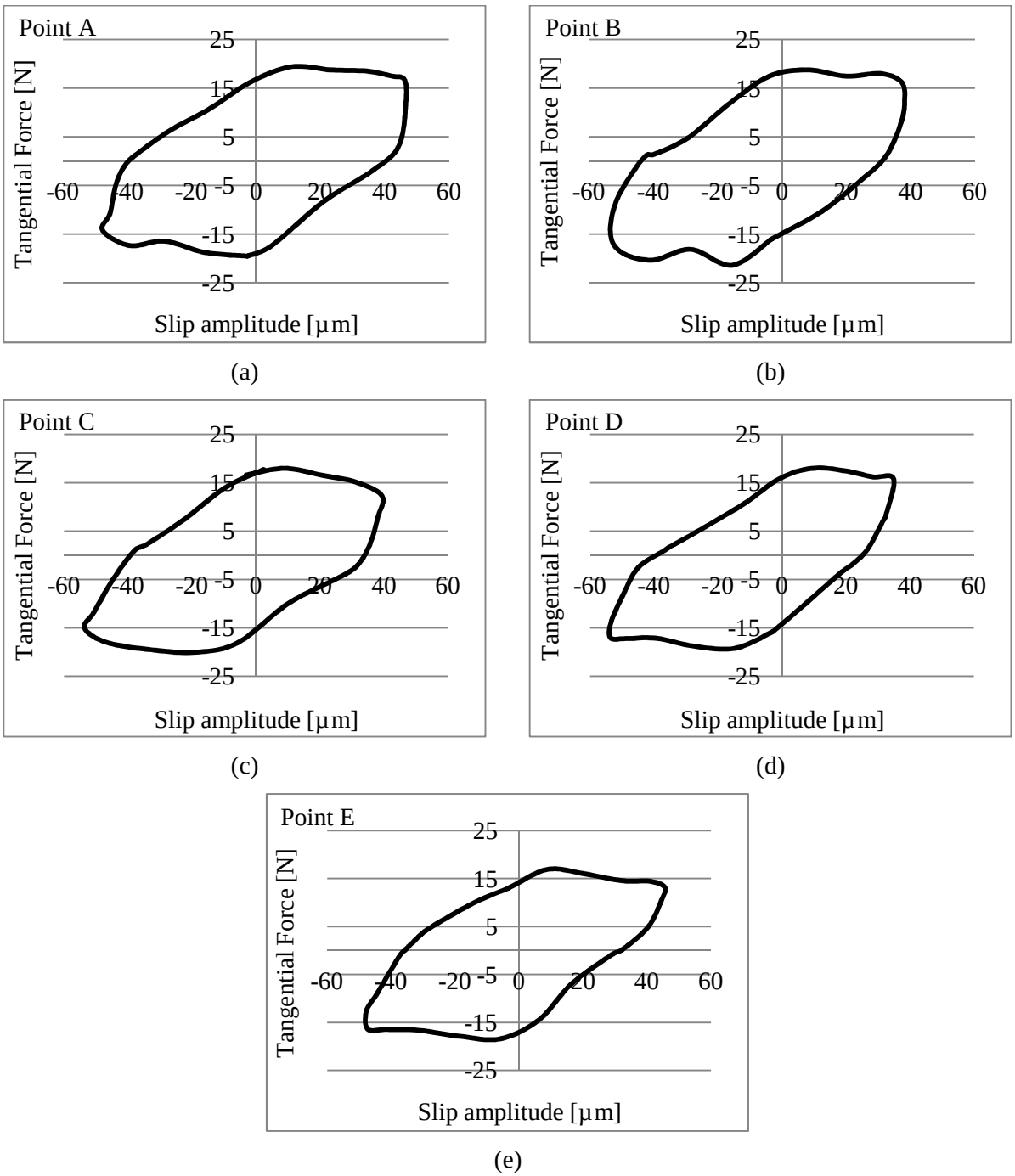

Figure 5.29: Hysteresis loops for the Ti-6Al-4V cylinder on WC-10wt%Co flat fretting contact subjected to tangential motion, taken at: (a) 10^5 cycles; (b) 3.125×10^5 cycles; (c) 5.125×10^5 cycles; (d) 7.125×10^5 cycles; (e) 9.125×10^5 cycles

A SEM image of the wear scar located on the flat WC-10wt%Co specimen is provided in Figure 5.30. Once again the direction of the fretting motion is indicated by the red arrow in the figure. The wear scar shows numerous areas of discoloration, but no evidence of actual wear on the WC-10wt%Co surface is visible.

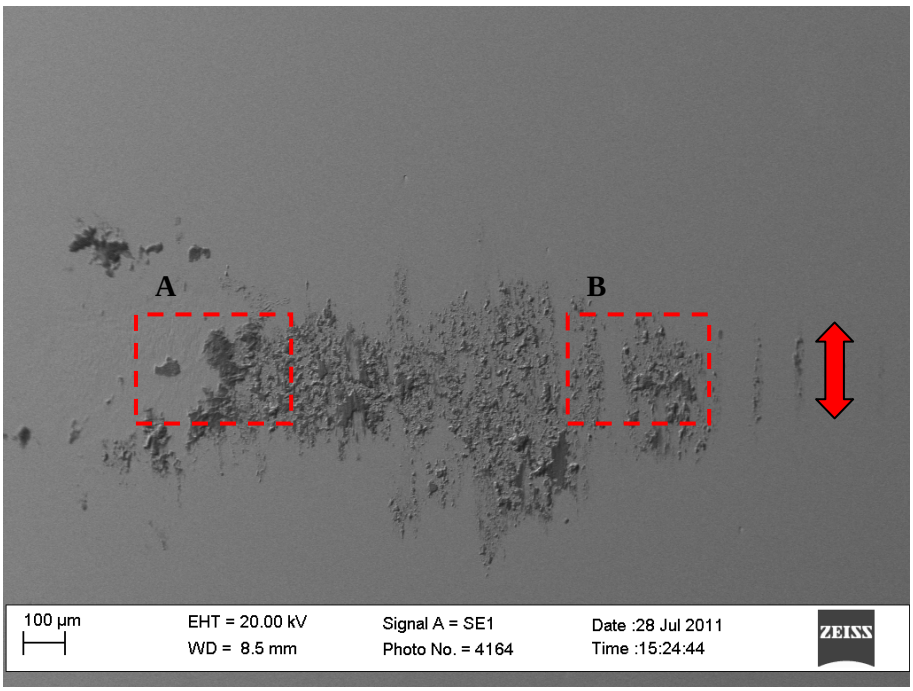

Figure 5.30: SEM image of the wear scar on the flat WC-10wt%Co specimen produced by the Ti-6Al-4V cylinder on a WC-10wt%Co flat fretting contact subjected to tangential motion

Area A and area B in Figure 5.30 represent two areas of interest that were identified in order to gain more insight into the wear mechanisms that occurred, as well as to find a reason for the high friction coefficient values provided in Figure 5.28. Magnified SEM images of the area A and area B be are provided in Figure 5.31(a) and Figure 5.31(b) respectively.

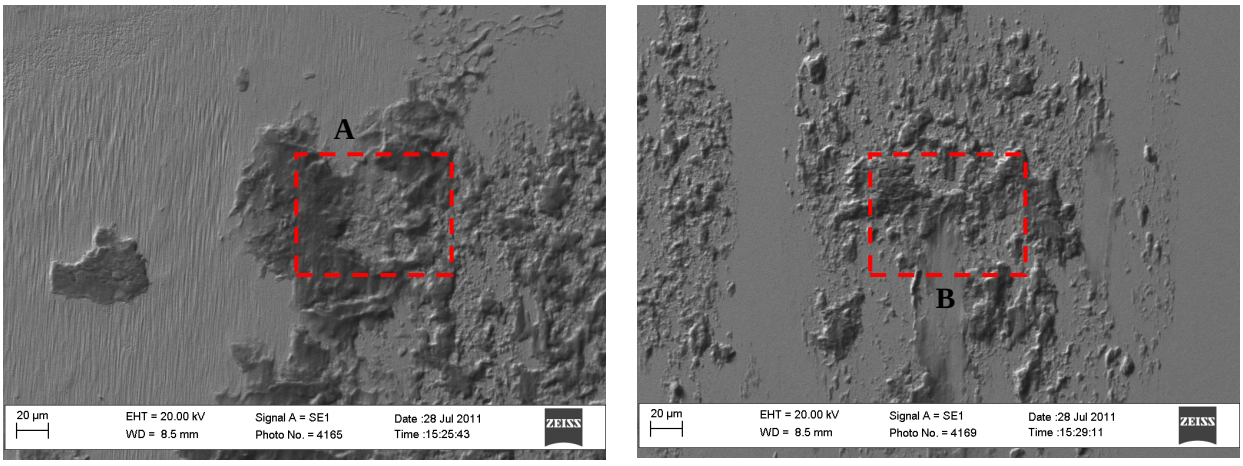

(a) (b)

Figure 5.31: (a) Magnified SEM image of point A in Figure 5.30; (b) magnified SEM image of point B in Figure 5.30

The Figure 5.31 provides no evidence wear on the flat WC-10wt%Co surface. Consequently the discoloration observed on the surface must have been caused by die attached of a foreign material. It was initially suspected that this foreign material originated from the Ti-6Al-4V cylinder. In order to investigate this assumption it was decided use an even higher magnification on the SEM, including quantitative EDX

analysis. The magnified SEM images of area A and area B in Figure 5.31, including the EDX analyses of both areas are provided in Figure 5.32.

The SEM image and EDX analysis of area A provided in Figure 5.32) revealed that the previously discussed assumption was indeed correct. The magnified SEM image of the area displays large areas where material was added to the flat surface, with no visible evidence of wear on the flat surface. This observation was supported by the EDX analysis of the image, provided in Figure 5.32(b). The analysis indicates that there is more titanium, and almost as much oxygen as tungsten present on the flat surface. This indicates that most of the material present in the image consists of oxide debris, originating from the Ti-6Al-4V cylinder. The magnified SEM image of area B in Figure 5.32(c) provided evidence of less material transfer, bust no visible wear. The EDX analysis in Figure 5.32(d) supported this observation.

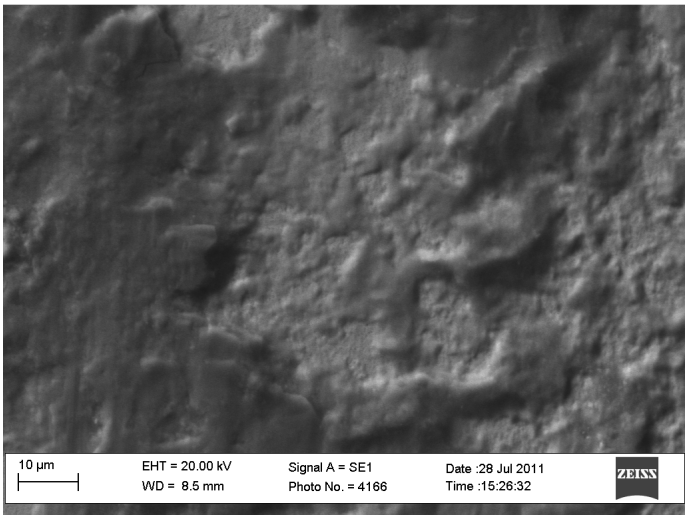

(a)

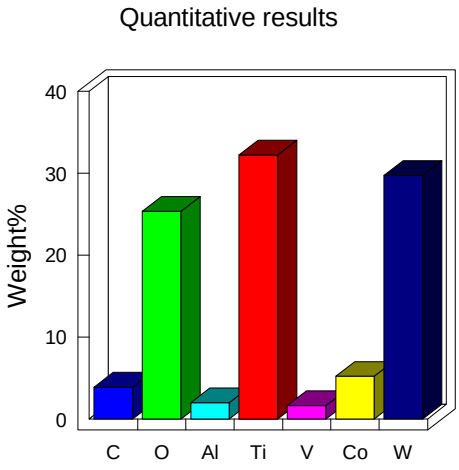

(b)

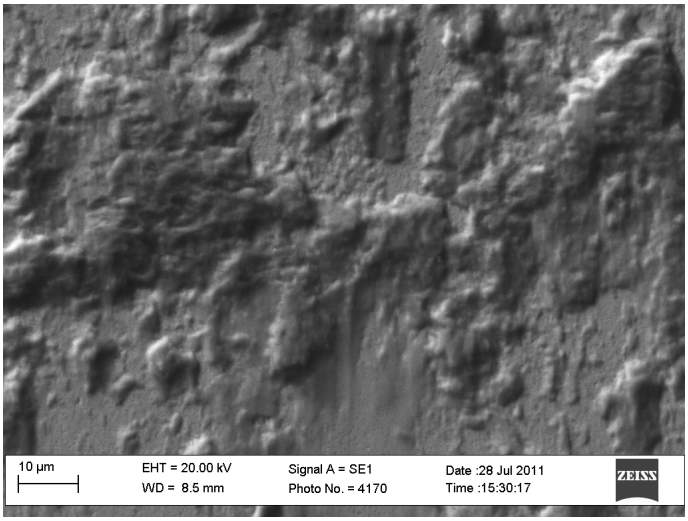

(c)

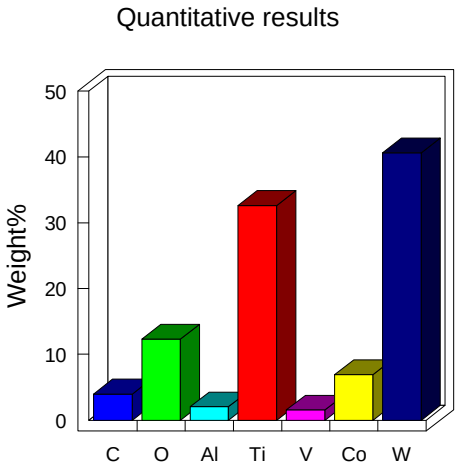

(d)

Figure 5.32: SEM image and EDAX analysis results of area A and area B in Figure 5.31: (a) SEM image of area A; (b) quantitative EDX analysis of area A; (c) SEM image of area B; (d) quantitative EDX analysis of area B

A summary of the quantitative EDX analysis results in Figure 5.32 is provided in Table 5.9.

Table 5.9: Summary of the quantitative EDX analyses in Figure 5.32 and Figure 5.33

	Weight%							
Figure	**W**	**Ti**	**O**	**Co**	**C**	**Al**	**V**	**Total**
Figure 5.31	29.709	32.215	25.345	5.215	3.889	1.995	1.632	100.000
Figure 5.32	40.614	32.615	12.322	6.921	3.971	2.027	1.529	100.000

A possible reason why no wear was observed on the flat WC-10wt%Co surface might be as a result of the high hardness of the material, compared to the Ti-6Al-4V cylinder. The information provided by the SEM analysis indicates that the three body wear phenomenon provides the best explanation for the high coefficient of friction. At the start of the experiment the Ti-6Al-4V cylinder was in full contact with the WC-10wt%Co flat surface. The high hardness of the carbide resulted in the wear of only the Ti-6Al-4V cylinder, detaching large particles and oxide debris from the cylinder. These particles might have initially impeded motion at the contact interface, resulting in the steep rise in the coefficient of friction. After at 10^5 cycles enough Ti-6Al-4V particles and oxide debris accumulated to cause three body wear.

As the wear process continued, a point might have been reached where the Ti-6Al-4V cylinder was almost completely separated from the WC-10wt%Co surface by Ti-6Al-4V wear debris. At this stage the fretting contact basically consisted of Ti-6Al-4V cylinder in contact with Ti-6Al-4V wear debris, located on the WC-10wt%Co flat surface. In essence, this boiled down to a Ti-6Al-4V cylinder on a Ti-6Al-4V flat fretting contact. This might explain the gradual decrease in the friction coefficient. The friction coefficient for Ti-6Al-4V cylinder-on-flat fretting experiment, discussed in Section 5.2.4 reached a steady state value just above 0.8. The coefficient of friction graph in Figure 5.28 seemed to also be decreasing towards a similar value, as more Ti-6Al-4V wear debris filled the contact and attached to the WC-10wt%Co flat surface.

According to Zhou [**74**] the fretting wear of Ti-6Al-4V is capable of inducing a so called tribologically transformed structure (TTS). Adhesion and the accumulation of plastic deformation, resulting in strain hardening at the fretting contact is responsible for the creation of this TSS [**16**]. According the Sauger [**75**] the TSS is capable of exhibiting twice the hardness of the bulk material. Gross slip in particular is renowned for creating a TTS in a short period of time [**74**]. After the TTS is subjected a sufficient amount of strain, the TSS will fragment into even more wear debris to join the third body material. The creation of such a TTS on the Ti-6Al-4V surface might be another reason for the high friction coefficient experienced during the first 4×10^5 cycles. The higher hardness of the titanium surface coupled with the superior hardness of the carbide surface might have caused the higher stress and strain values that were needed to break the asperity contact points, resulting from gross slip.

The results of the two other experiments involving Ti-6Al-4V and WC-10wt%Co, denoted 1.2 and 1.3 in Table 5.8, are provided in Section B.3 in APPENDIX B.

The graph of the coefficient of static friction for the Al7075-T6 cylinder on a WC-10wt%Co flat fretting contact subjected to axial motion is provided in Figure 5.33. From the figure it is evident that the friction coefficient remained fairly stable at value between 0.8 and 0.85. This coefficient is considerably lower than coefficient experienced during the previously discussed experiment, which involved Ti-6Al-4V.

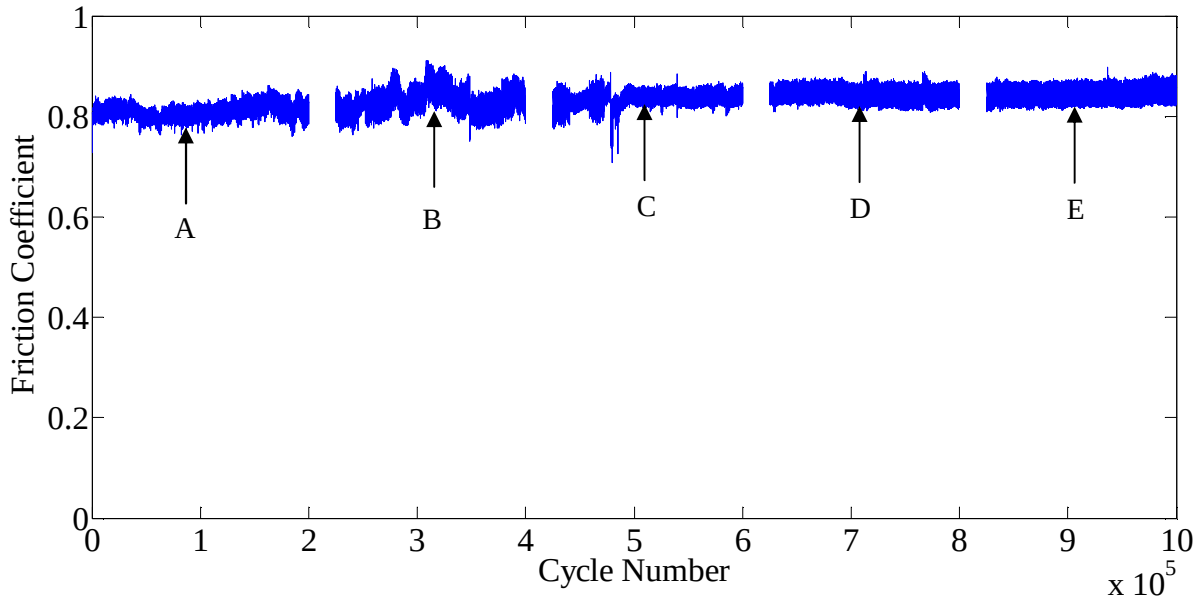

Figure 5.33: Coefficient of friction for a Al7075-T6 cylinder on a WC-10wt%Co flat fretting contact subjected to axial motion [Normal force = 20N, Frequency = 80Hz, Slip (peak-to-peak) = 100 µm; Cycles = 10^6]

The hysteresis loops of the cycles located at points A, B, C, D and E in Figure 5.33 are provided in Figure 5.34. The quasi-rectangular shape of these loops once again indicates that gross slip and consequently fretting wear occurred. From the figure it is evident that similar amounts of energy were dissipated in the form of friction at all five points. The reason for this is that the enclosed area of all five loops remained fairly constant. Comparing the loops in Figure 5.34 with the loops of the titanium experiment in Figure 5.29 reveals the tangential/friction force experienced for the Al7075-T6 experiment was considerably lower. This result corresponds to the lower static friction coefficient graph in Figure 5.33. The reason for this is not apparent from Figure 5.33 or Figure 5.34, and therefore a SEM analysis of the wear scar located on the WC-10wt%Co flat surface was also performed.

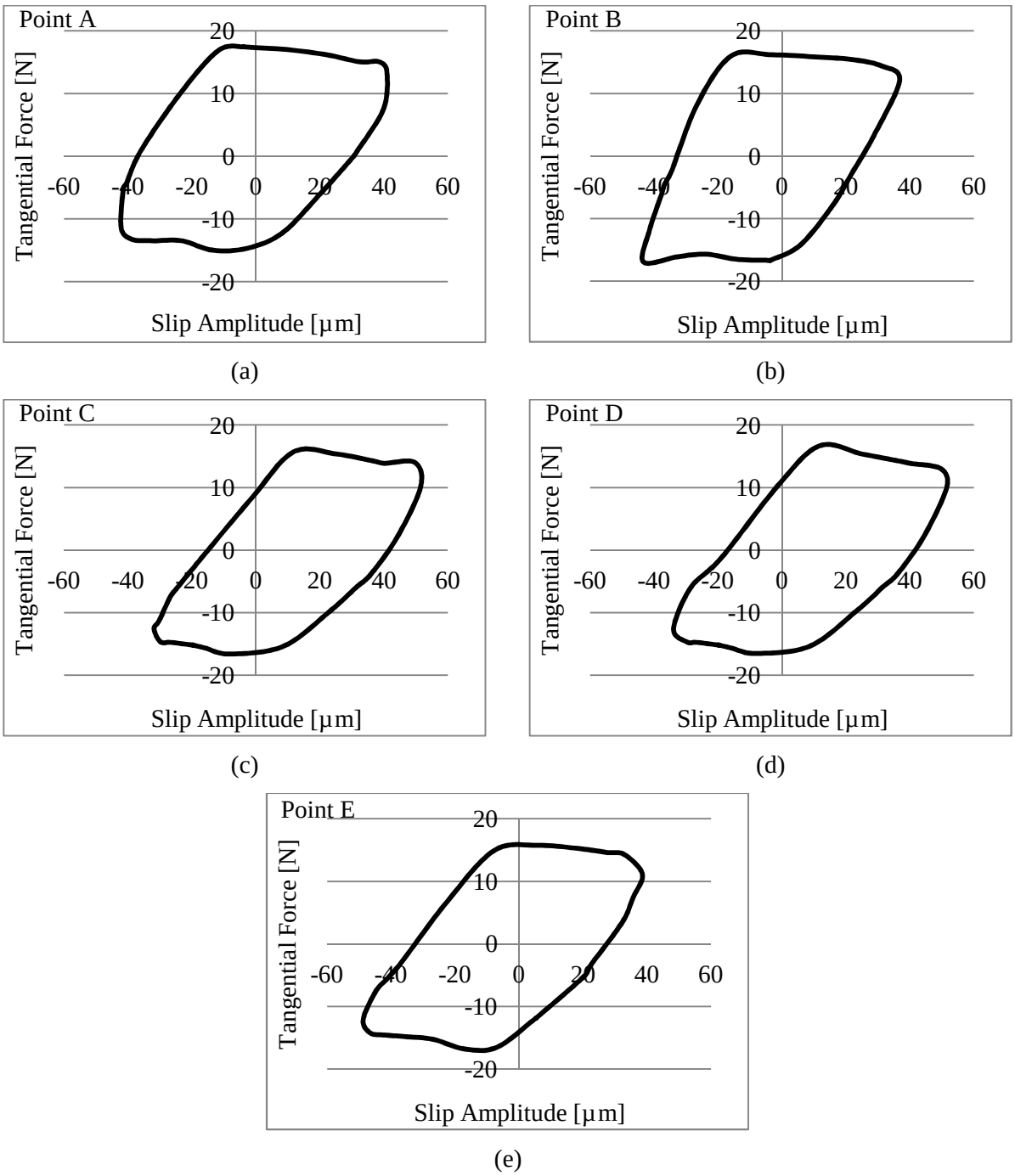

Figure 5.34: Hysteresis loops for the AL7075-T6 cylinder on WC-10wt%Co flat fretting contact subjected to axial motion, taken at: (a) 10^5 cycles; (b) 3.125×10^5 cycles; (c) 5.125×10^5 cycles; (d) 7.125×10^5 cycles; (e) 9.125×10^5 cycles

Figure 5.35 provides a SEM image of the wear scar located on the WC-10wt%Co flat. The red arrow in the figure represents the direction of the fretting motion. The wear scars shows several scattered areas of discoloration. Similar to the titanium experiment perilously discussed, no wear is visible on the WC-10wt%Co flat surface. The dashed red box in the figure represents an area of interest that was indentified for closer inspection. A magnified SEM image of this area, including the quantitative EDX analysis of the area is provided in Figure 5.36.

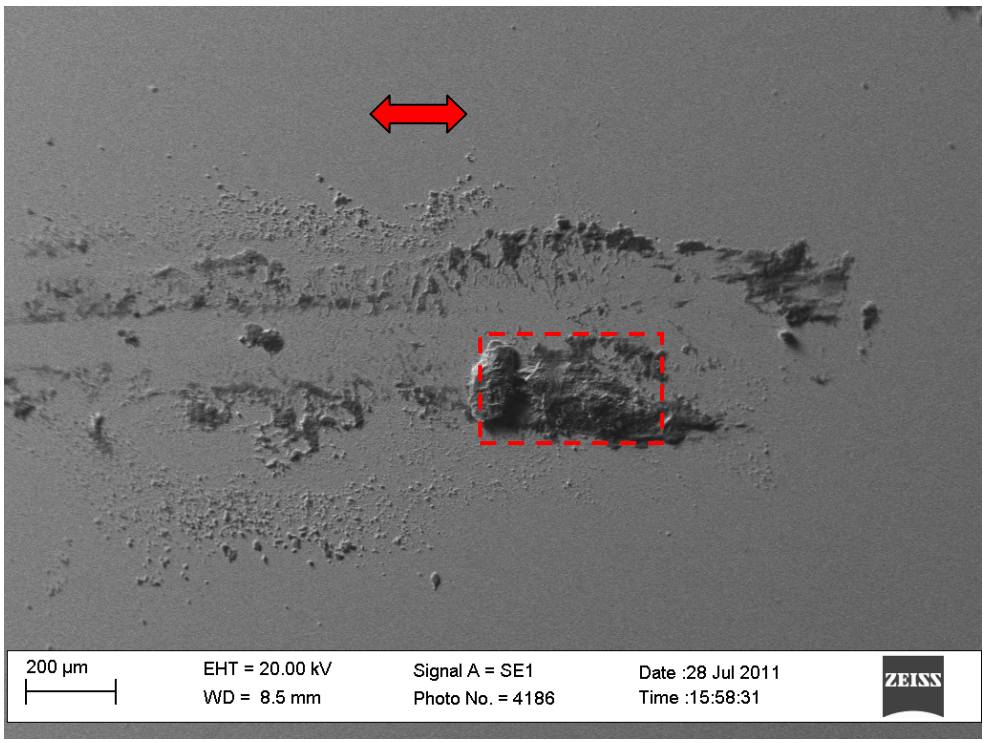

Figure 5.35: SEM image of the wear scar on the flat WC-10wt%Co specimen produced by the Al7075-T6 cylinder on a WC-10wt%Co flat fretting contact subjected to axial motion

The magnified SEM image in Figure 5.36(a) indicates that the wear scar on the WC-10wt%Co flat surface consists of foreign material that was added to the surface. The quantitative EDX analysis of the magnified SEM image provided in Figure 5.36(b) reveals that the material that was added primarily consists of aluminum and oxygen. Thus, the added material consists of wear particles and oxide debris that originated from the wear of the Al7075-T6 cylinder. To prove this assumption was it decided to inspect the added material in even more detail. The dashed red box in Figure 5.36(a) corresponds to a final area of interest, chosen for more detailed SEM analysis.

The results or this analysis are provided in Figure 5.37 and consist of a magnified SEM image as well as a quantitative EDX analysis of the highlighted area in Figure 5.36(a). The magnified SEM image in Figure 5.37(a) shows a surface area consisting of material that was added to the carbide surface. The image also provides evidence of loose wear debris that were trapped within the fretting contact. This evidence supports the assumption that the discolored areas on the carbide surface consist of material added to the surfaced as a result of the fretting wear.

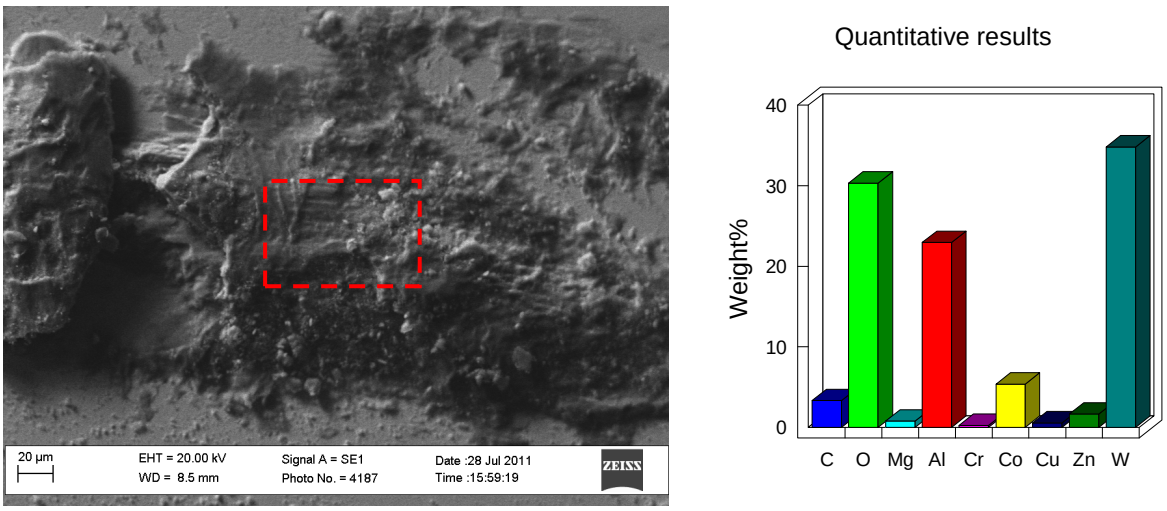

(a) (b)

Figure 5.36: SEM image and EDX analysis results of dashed area in Figure 5.35: (a) SEM image; (b) quantitative EDX analysis from image

According to the quantitative EDX analysis results in Figure 5.37(b) the material surface in Figure 5.37(a) almost entirely consists of aluminum and oxygen. This also proves the assumption that the material added to the flat carbide surface consist of wear particles and oxide debris that originated from the Al7075-T6 cylindrical specimen. A summary of the quantitative EDX analyses in Figure 5.36(b) and Figure 5.37(b) is provided in Table 5.10.

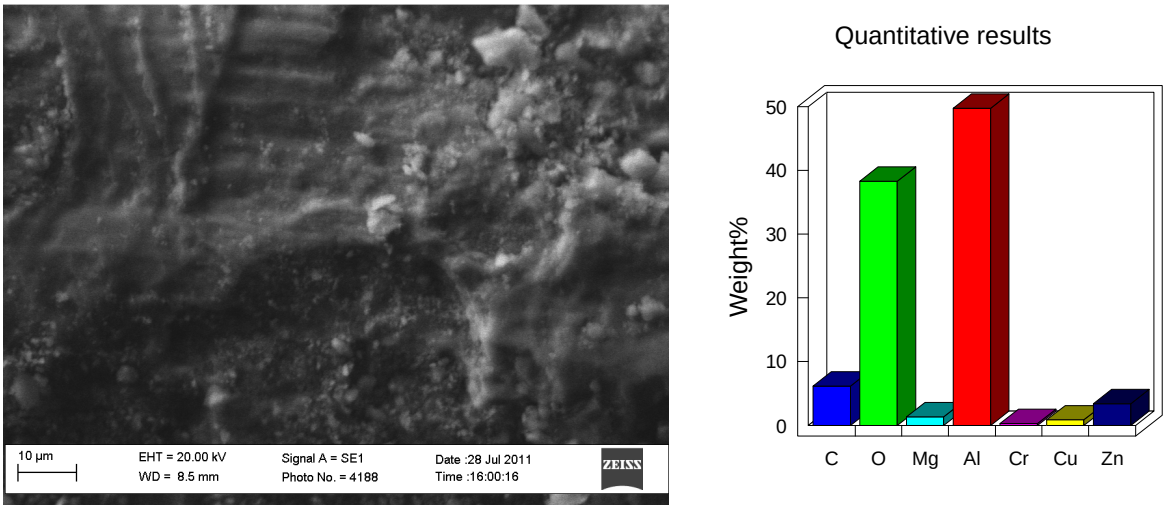

(a) (b)

Figure 5.37: SEM image and EDX analysis results of dashed area in Figure 5.36: (a) SEM image; (b) quantitative EDX analysis from image

Table 5.10: Summary of the quantitative EDX analyses in Figure 5.36 and Figure 5.37

	Weight%									
Figure	**W**	**O**	**Al**	**C**	**Co**	**Zn**	**Mg**	**Cu**	**Cr**	**Total**
Figure 5.36	34.819	30.346	22.949	3.313	5.361	1.659	0.767	0.547	0.239	100.000
Figure 5.37	0.000	38.295	49.723	6.144	0.000	3.381	1.322	0.867	0.268	100.000

The results of both experiments discussed, confirmed that no wear was found on the WC-10wt%Co surfaces. The extremely high hardness of the cemented carbide was responsible for this. However, the coefficient of static friction resulting of the Al7075-T6 on WC-10wt%Co contact couple was much lower than the coefficient of static friction of the Ti-6Al-4V on WC-10wt%Co contact couple. A possible reason for this is the low modulus of elasticity of Al7075-T6 (71.7 GPa), compared to Ti-6Al-4V (113.8 GPa). Consequently the stresses and strains needed to break the Al7075-T6 asperity contacts were much less than for the Ti-6Al-4V. The reason for this is that the asperities of Al7075-T6 yielded and fractured far more easily that the asperities of Ti-6Al-4V, resulting in lower friction forces. The results of the other experiment involving Al7075-T6 and WC-10wt%Co, denoted 1.4 in Table 5.8, is provided in Section B.3 in APPENDIX B.

5.4.2 Spark Plasma Sintered (SPS) Cemented Tungsten Carbides

In addition to conventionally sintered WC-Co, the fretting wear of as spark plasma sintered (SPS) cemented tungsten carbide was also investigated. During the SPS process the sintered powders are compacted under high pressure, within graphite dies. The powder is then subjected high pulsed DC currents, responsible for generating spark plasma [**76**]. The process allows for the sintering of materials at low temperatures, compared to conventional sintering techniques. The SPS process is also capable of dramatically reducing the sintering times of cemented carbides.

Excessive grain growth can sometimes be a problem in SPS cemented carbides. The materials are therefore doped with grain growth inhibitors in order to counteract the unwanted grain growth. The SPS cemented carbide tested used for this study is WC – 10wt%Co – 10wt%NbC - 0.3wt%Cr_3C_2. This material was manufactured at the Department of Materials and Environmental Chemistry, Stockholm University, Sweden.

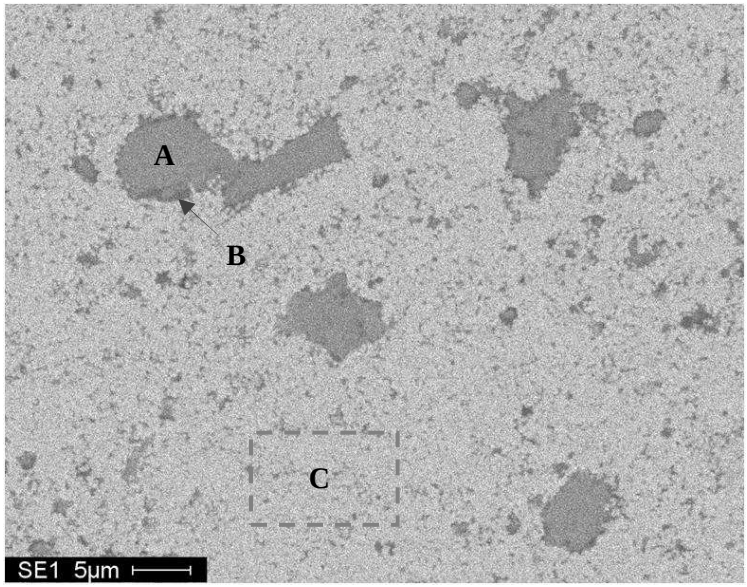

Figure 5.38: SEM image of WC – 10wt%Co – 10wt%NbC - 0.3wt%Cr3C2

Figure 5.38 provides a SEM image of WC – 10wt%Co – 10wt%NbC - 0.3wt%Cr3C2. This image was taken by a Philips XL30 ESEM-FEG. EDX analysis was also done using EDAX Genesis Imaging/Mapping Version 4.52 software, in order to identify the elements in the SEM image. Point A and point B in Figure 5.38 refers to two point analysis performed, while the dashed box indicates an area analysis performed. The elements and the relative weight percentages resulting from these three analyses are provided in Table 5.11. The mechanical properties of WC – 10wt%Co – 10wt%NbC - 0.3wt%Cr3C2 were determined at Element 6 (pty).Ltd and are provided in Table 5.12.

Table 5.11: SEM and EDX analysis of WC – 10wt%Co – 10wt%NbC - 0.3wt%Cr3C2

	Element	**Weight%**
Point A	C	27.77
	Nb	72.23
Point B	B	30.78
	O	07.66
	Nb	30.53
	Cr	03.54
	Co	08.18
	W	19.31
Area C	CK	08.67
	CoK	08.76
	WL	82.56

Table 5.12: Mechanical properties of WC – 10wt%Co – 10wt%NbC - 0.3wt%Cr3C2

Mechanical property	**Ti-6Al-4V**
Hardness [GPa]	14.35
Density [g/cm^3]	14.52
Fracture Toughness [MPa.m$^{1/2}$]	16.76
Modulus of Elasticity [GPa]	620.2

The WC – 10wt%Co – 10wt%NbC - 0.3wt%Cr3C2 flat specimens were involved in the same five extended fretting wear experiments as the conventionally sintered WC-10wt%Co flat specimens. The experimental parameters of these experiments were exactly the same as for extended experiments discussed in the previous three sections of this chapter. Table 5.13 provides a summary of all the materials involved, as well as the contact conditions of these five experiments.

Table 5.13: Summary of the WC – 10wt%Co – 10wt%NbC - 0.3wt%Cr3C2 fretting wear experiments

Number	Specimen 1	Specimen 2	Motion
2.1	WC – 10wt%Co – 10wt%NbC - 0.3wt%Cr3C2 flat	Ti-6al-4V cylinder	Tangential motion
2.2	WC – 10wt%Co – 10wt%NbC - 0.3wt%Cr3C2 flat	Ti-6al-4V cylinder	Axial motion
2.3	WC – 10wt%Co – 10wt%NbC - 0.3wt%Cr3C2 flat	Al7075-T6 cylinder	Tangential motion
2.4	WC – 10wt%Co – 10wt%NbC - 0.3wt%Cr3C2 flat	Al7075-T6 cylinder	Axial motion

Figure 5.39 provides a graph of the coefficient of static friction of the Ti-6Al-4V cylinder on WC – 10wt%Co – 10wt%NbC - 0.3wt%Cr3C2 flat fretting contact subjected to tangential motion. The coefficient in graph started off at value of 078 and increased to a value of about 1 within the first 60000 cycles. After 60000 cycles the coefficient remained fairly stable, displaying slight variations about for the remainder of the experiment. It is however important to note the coefficient of friction graph in Figure 5.39 fluctuated much more than the coefficient of friction graph of the Ti-6Al-4V - WC-10wt%Co experiment, provided in Figure 5.28.

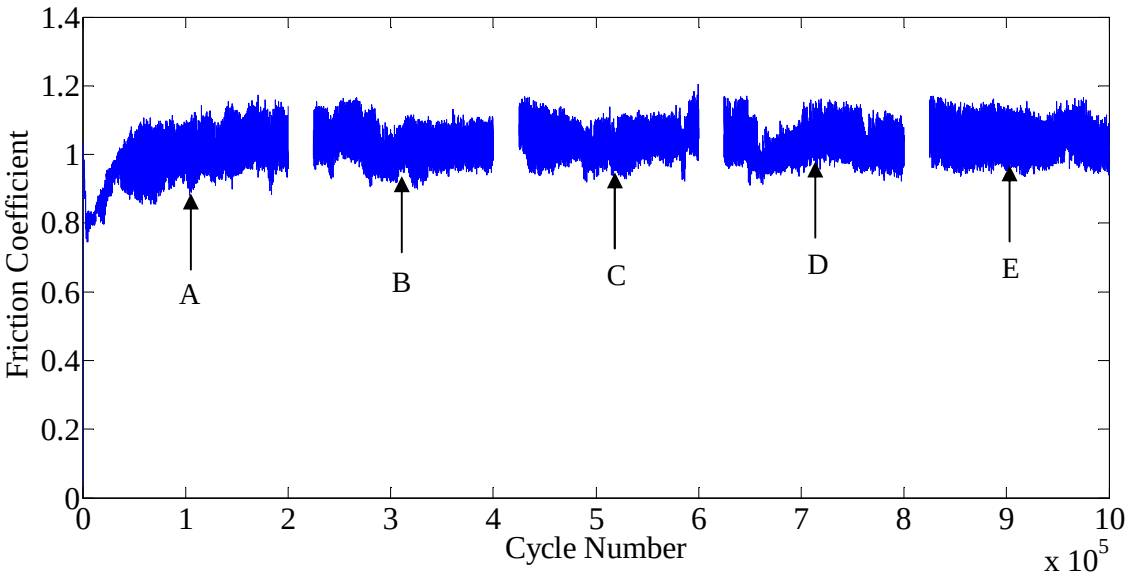

Figure 5.39: Coefficient of friction for the Ti-6Al-4V cylinder on WC – 10wt%Co – 10wt%NbC - 0.3wt%Cr3C2 flat fretting contact subjected to tangential motion [Frequency = 80Hz, Slip (peak-to-peak) = 100 μm; Cycles = 10^6]

The hysteresis loops for points A, B, C, D and E in Figure 5.39 are provided in Figure 5.40. The Five hysteresis loops in the figure display almost identical quasi-rectangular shapes, indicating that fretting wear had occurred as a result of gross slip. The similarities between the loops also indicate that the friction energy dissipated during the experiment remained fairly constant. This result corresponds to the information

provided by the graph in Figure 5.40, because a fairly constant friction coefficient should result in a constant amount of friction energy dissipated.

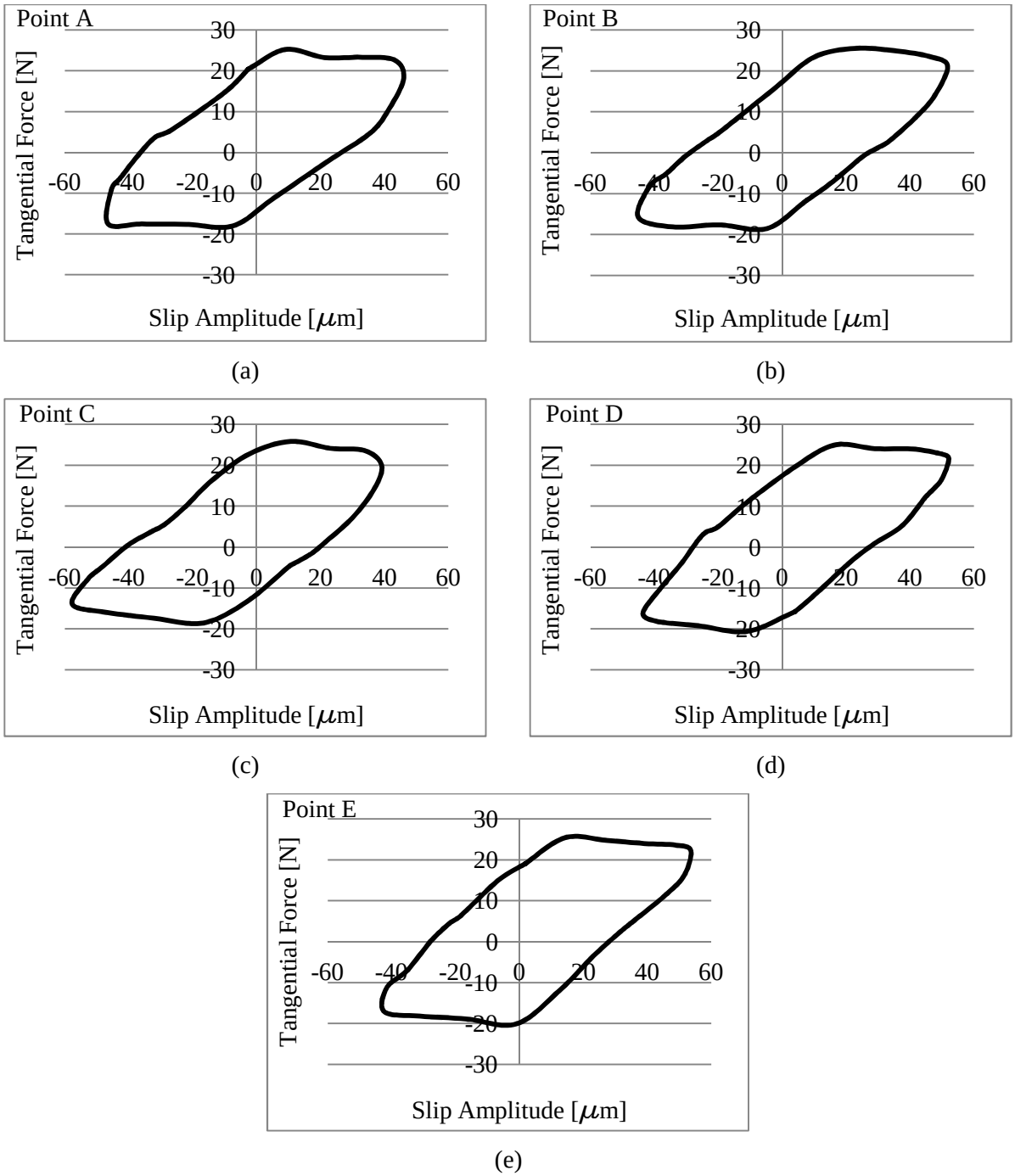

Figure 5.40: Hysteresis loops for the Ti-6Al-4V cylinder on WC – 10wt%Co – 10wt%NbC - 0.3wt%Cr3C2 flat fretting contact subjected to axial motion, taken at: (a) 10^5 cycles; (b) 3.125×10^5 cycles; (c) 5.125×10^5 cycles; (d) 7.125×10^5 cycles; (e) 9.125×10^5 cycles

The SEM image of the wear scar located on the flat WC – 10wt%Co – 10wt%NbC - 0.3wt%Cr3C2 specimen is provided in Figure 5.41, with the red arrow indicating the direction of the fretting motion. The image shows various areas of discoloration, but no wear of the flat carbide surface is visible at this magnification.

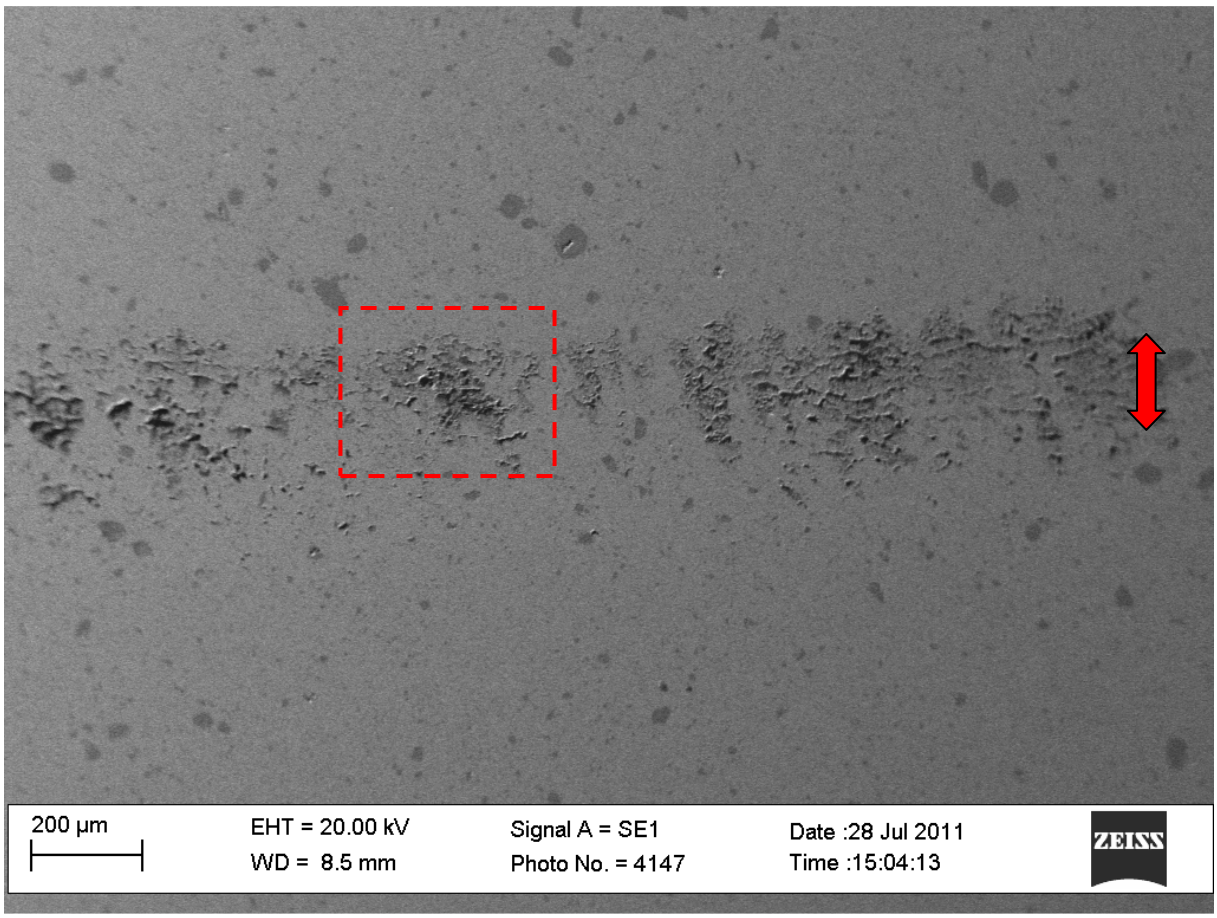

Figure 5.41: SEM image of the wear scar on the flat WC – 10wt%Co – 10wt%NbC - 0.3wt%Cr3C2 specimen produced by the Ti-6Al-4V cylinder on a WC – 10wt%Co – 10wt%NbC - 0.3wt%Cr3C2 flat fretting contact subjected to tangential motion

The magnified SEM image of the area enclosed by the dashed box in Figure 5.41, as well as quantitative EDX analysis of this area is provided in Figure 5.42. The image in Figure 5.42(a) indicates that the wear scar consists of foreign material that was added to the flat carbide surface. However, no evidence of actual wear is visible on the carbide surface. The quantitative EDX analysis provided in Figure 5.42(b) reveals that the surface area primarily consists of tungsten with traces of the cobalt bonder. Evidence of the niobium grains is also provided by the EDX analysis. The analysis indicates that titanium and oxygen are also present on the surface. In order to establish the origin of the foreign material it was decide the conducted a more detailed analysis on one of the dark patches of added material in Figure 5.42(a). The area chosen for this analysis is represented by the area enclosed by the dashed red box in Figure 5.42(a). The magnified SEM image as well as the quantitative EDX analysis of this area is provided in Figure 5.43.

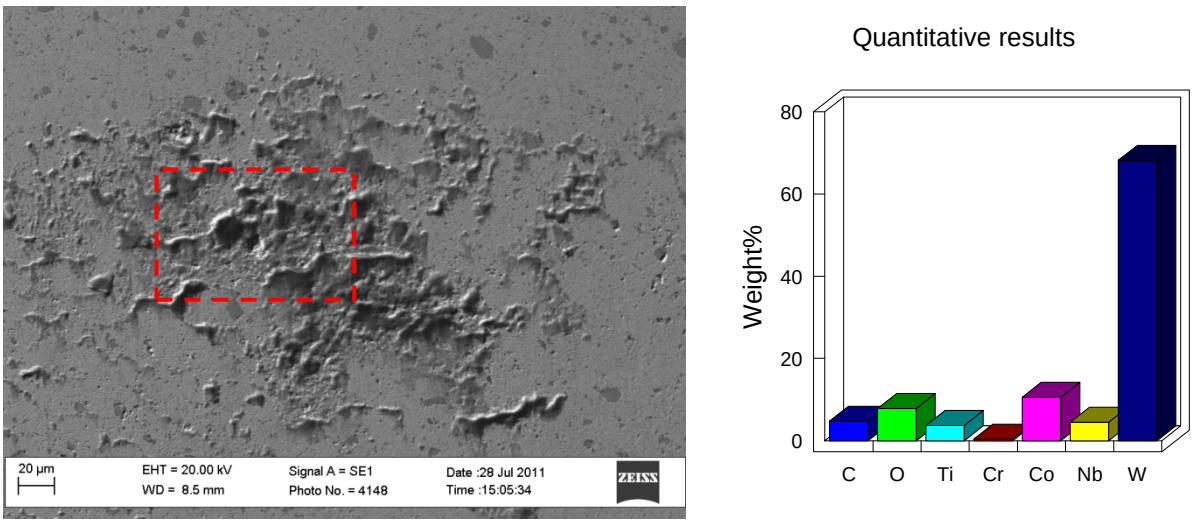

(a) (b)

Figure 5.42: Magnified SEM image of the area enclosed by the dashed red box in Figure 5.41; (b) quantitative EDX analysis of the magnified SEM image

The magnified SEM image in Figure 5.43(a) once again provides no evidence that any actual wear had taken place on the carbide surface. The image does however confirm that the discoloration was without a doubt caused by the addition of foreign material to the carbide surface. The increase in oxygen and titanium weight percentages from Figure 5.42(b) to Figure 5.43(b), proves that the foreign material added to the carbide surface primarily consists of titanium and oxygen. It is believed that the titanium and oxygen resulted from wear particles and oxide debris that originated from the Ti-6Al-4V cylindrical specimen, and adhered to the extremely hard carbide surface. A summary of the two quantitative EDX analyses in Figure 5.42(b) and Figure 5.43(b) are provided in Table 5.14.

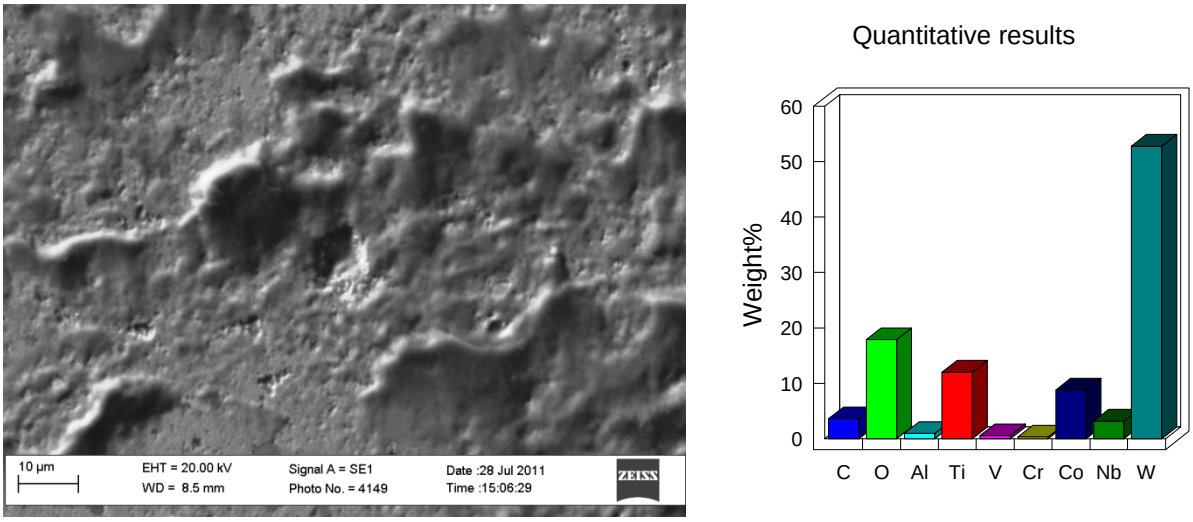

(a) (b)

Figure 5.43: Magnified SEM image of the area enclosed by the dashed red box in Figure 5.42; (b) quantitative EDX analysis of the magnified SEM image

Table 5.14: Summary of the quantitative EDX analysis results provided in Figure 5.42 and Figure 5.43

	Weight%									
Figure	**W**	**Co**	**O**	**Ti**	**C**	**Nb**	**Cr**	**Al**	**V**	**Total**
Figure 5.42(b)	68.217	10.564	7.820	3.688	4.778	4.495	0.440	0.000	0.000	100.000
Figure 5.43(b)	52.829	8.768	17.873	12.001	3.578	3.150	0.309	0.945	0.547	100.000

The results of the experiment are fairly similar to the results discussed for the Ti-6Al-4V on WC-10wt%Co fretting experiment. Once again no recognizable wear was found on the carbide surface. This is believed to be as a result of the high harness and modulus of elasticity of the SPS carbide, compared to Ti-6Al-4V. This resulted in the generation of only Ti-6Al-4V wear debris as a result of the asperity contact interaction. The high coefficient of friction observed in Figure 5.39 may once again have been caused by the generation of a called tribologically transformed structure (TTS), on the Ti-6Al-4V surface. The harder TTS on the Ti-6Al-4V surface might have been responsible for the high stresses and forces at that contact interface, resulting in the high friction observed. The results of the other experiment involving WC – 10wt%Co – 10wt%NbC - 0.3wt%Cr3C2, denoted 2.2 in Table 5.13 is provided in Section B.4 in APPENDIX B.

Figure 5.44 provides the graph of the coefficient of static friction of the Al7075-T6 cylinder on the WC – 10wt%Co – 10wt%NbC - 0.3wt%Cr3C2 fretting contact subjected tangential motion. The graph indicates that the friction coefficient remained fairly constant during the experiment, with small variations that occurred at regular intervals. Comparing Figure 5.44 with Figure 5.39 reveals that the friction generated by the Al7075-T6 – SPS fretting contact was much less and for more stable than the friction generated by the Ti-6Al-4V – SPS fretting contact.

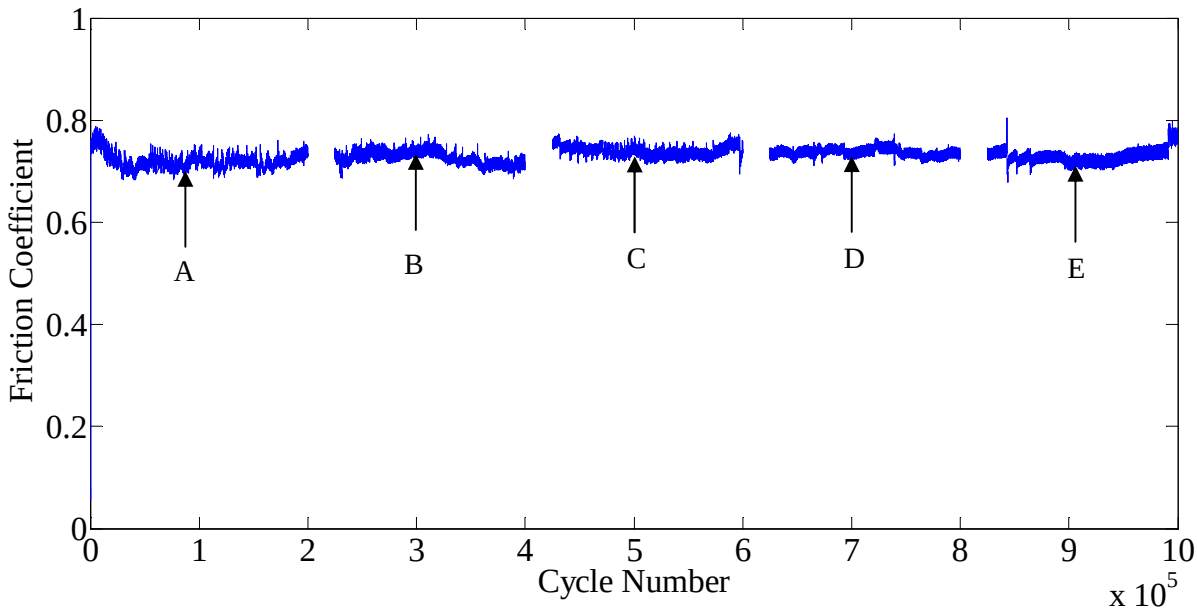

Figure 5.44: Coefficient of friction for the Al7075-T6 cylinder on WC – 10wt%Co – 10wt%NbC - 0.3wt%Cr3C2 flat fretting contact subjected to tangential motion [Frequency = 80Hz, Slip (peak-to-peak) = 100 μm; Cycles = 10^6]

Figure 5.45 provides the five hysteresis loops for the fretting cycles at points A, B, C, D and E in Figure 5.44. All five loops in the figure display the same quasi-rectangular shape, indicating that fretting wear had taken place. The information provided in Figure 5.45 also indicates that the friction energy dissipated during the experiment remained fairly constant throughout the 10^6 cycles.

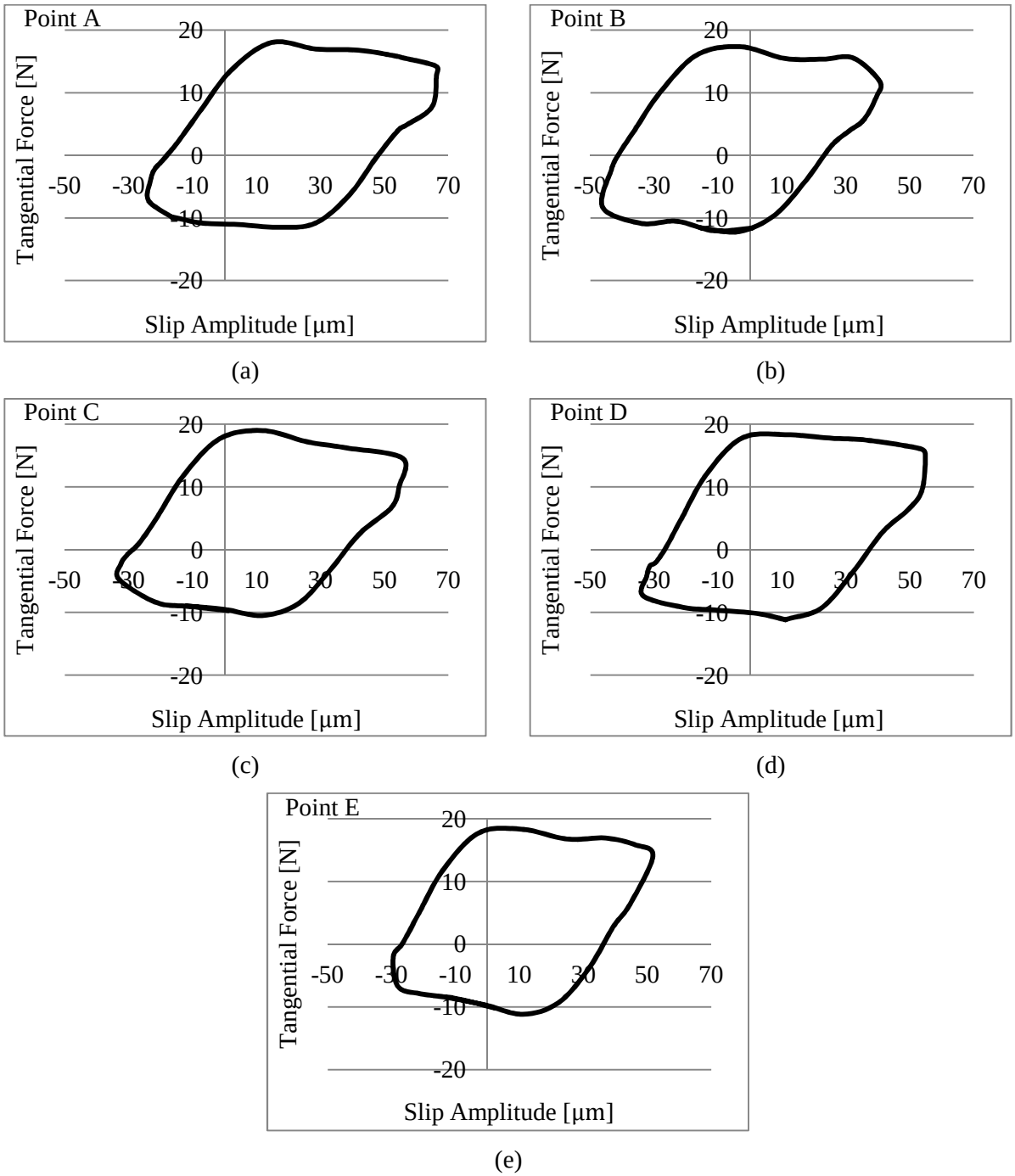

Figure 5.45: Hysteresis loops for the Al7075-T6 cylinder on WC – 10wt%Co – 10wt%NbC - 0.3wt%Cr3C2 flat fretting contact subjected to tangential motion taken at: (a) 10^5 cycles; (b) 3.125×10^5 cycles; (c) 5.125×10^5 cycles; (d) 7.125×10^5 cycles; (e) 9.125×10^5 cycles

SEM images of two different points of the wear scar located on the WC – 10wt%Co – 10wt%NbC - 0.3wt%Cr3C2 flat specimen are provided in Figure 5.46. These two wear scar images correspond to the two

end points of the cylinder-on-flat contact, and shows two large discolored areas on the flat specimen. The images however provide no evidence that any wear had taken place on the flat carbide surface. The red arrow in each image represents the direction of the fretting motion.

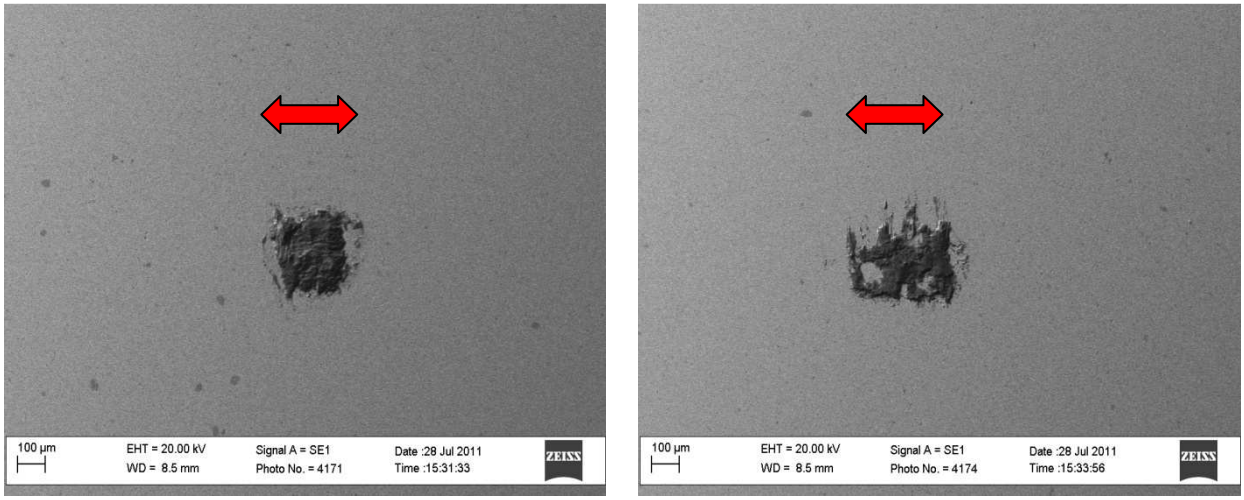

(a) (b)

Figure 5.46: Two SEM images of the wear scar on the flat WC – 10wt%Co – 10wt%NbC - 0.3wt%Cr3C2 specimen produced by the Al7075-T6 cylinder on a WC – 10wt%Co – 10wt%NbC - 0.3wt%Cr3C2 flat fretting contact subjected to tangential motion

In order to gain more insight into the wear mechanisms involved, higher magnified SEM images of the two wear scars in Figure 5.46 are provided in Figure 5.47. The two magnified SEM images provide no evidence of wear on the flat carbide surface. The images do however provided evidence that foreign material was added to the flat carbide surface.

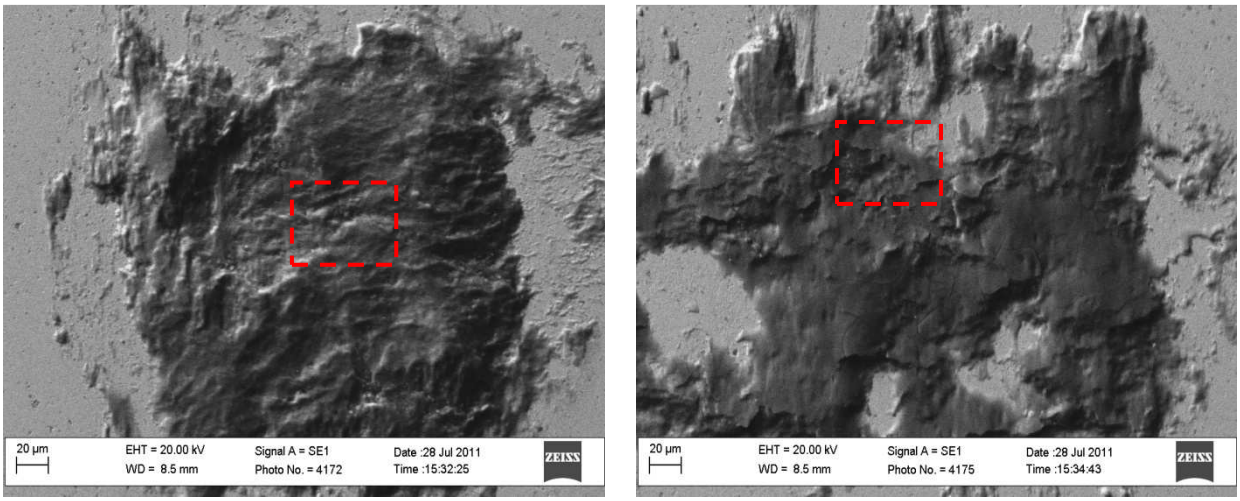

(a) (b)

Figure 5.47(a) Magnified SEM image of the fretting wear scar in Figure 5.46(a); (b) Magnified SEM image of the fretting wear scar in Figure 5.46(b)

The dashed red box in each SEM image in Figure 5.47 represents the area chosen in order to conduct a quantitative EDX analysis. The purpose of each analysis was to determine what elements were present in

each chosen area, as well as the relative weight percentages of each element. The magnified SEM images as well as the results of the quantitative EDX analyses of these images are provided in Figure 5.48.

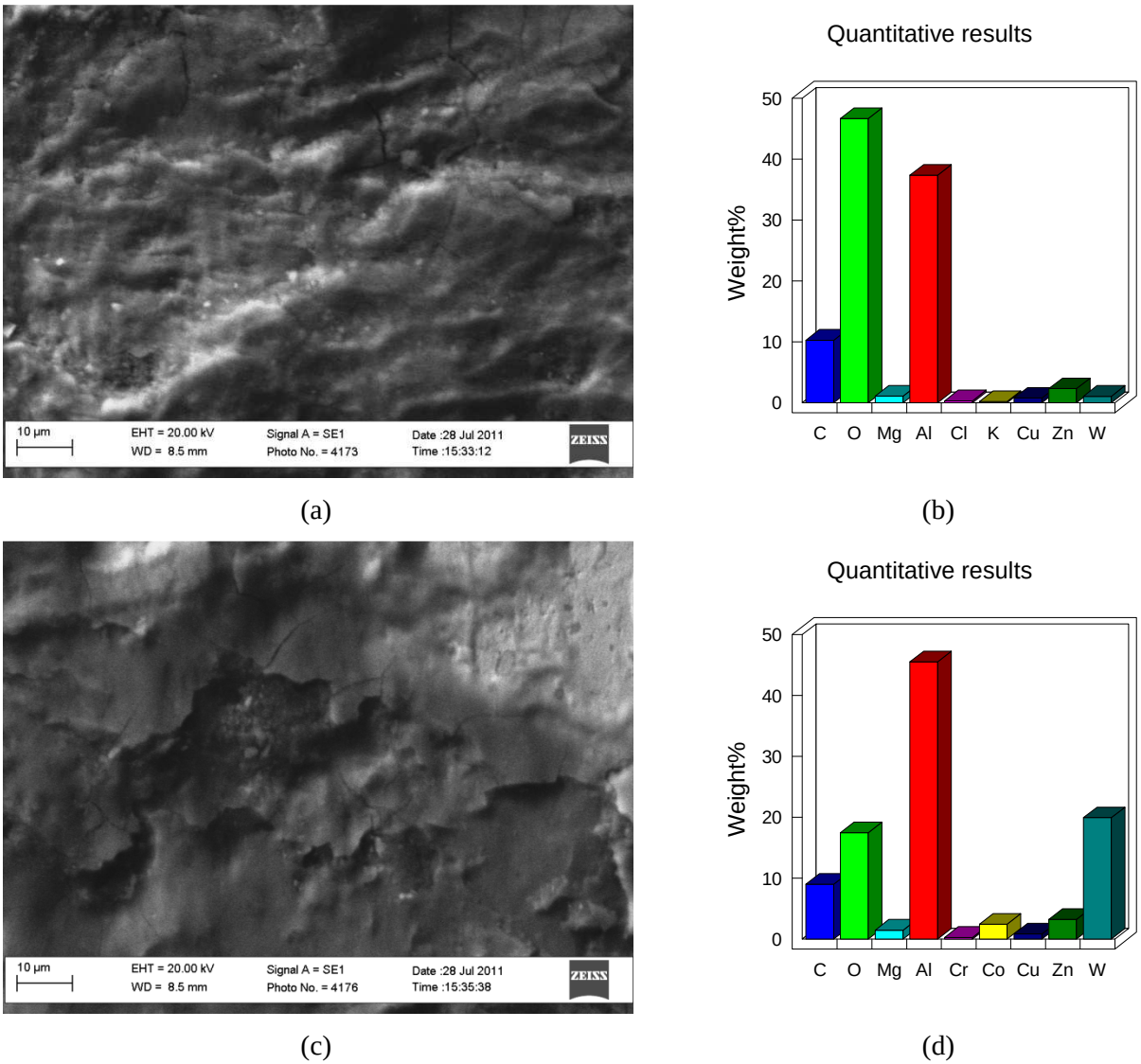

Figure 5.48: SEM images and quantitative EDX analysis results of the two dashed boxes in Figure 5.47 (a) SEM image represented by the dashed box in Figure 5.47(a); (b) quantitative EDX of the SEM images in (a); (c) SEM image represented by the dashed box in Figure 5.47(c); (d) quantitative EDX of the SEM images in (c)

Both of the SEM images in Figure 5.48 support the assumption that the two wear scars in Figure 5.46 are not wear scars, but actually areas where material was added. According to the quantitative EDX analyses, both surface areas primarily consist of aluminium and oxygen. It can thus be assumed that the foreign material added to the carbide surface, originated from the Al7075-T6 cylinder. Both of the SEM images in the figure also provide evidence of cracking and delaminating of the added material. This was not observed for the ti-6Al-4V experiments. A possible reason for this might be that aluminium oxide is known to be harder and more brittle than titanium oxide, causing the aluminium oxide on carbide surface to crack more easily. This observation corresponds to the result discussed for the extended Al7075-T6 – Al7075-T6 experiment in Section 5.3.3. A summary of the two quantitative EDX analyses in Figure 5.48 are provided in Table 5.15.

Table 5.15: Summary of the quantitative EDX analysis results provided in Figure 5.48(b) and (d)

	Weight%							
Spectrum	**O**	**Al**	**C**	**Zn**	**Mg**	**Co**	**Cu**	**Total**
Figure 5.48(b)	46.659	37.857	10.283	2.306	1.073	0.000	0.760	100.000
Figure 5.48(d)	41.525	33.943	8.482	2.002	0.963	1.405	0.520	100.000

The result of the other experiment involving WC – 10wt%Co – 10wt%NbC - 0.3wt%Cr3C2 and, denoted 2.4 and in Table 5.13 is provided in Section B.4 in APPENDIX B.

6 Conclusion and Recommendations

6.1 Conclusion

The five main research questions stipulated in Chapter 3 were addressed. The literature study and project motivation provided a comprehensive background on fretting, and on fretting encountered in aerospace applications in particular. It was discovered that not much research has been done on the effect of fretting wear in aerospace applications. This deficiency in the field of fretting research was the main motivation behind the study.

The fretting test apparatus utilized in the study was developed to simulate the possible fretting wear conditions encountered in two well known aircraft contact configurations. The experimental study found that the test apparatus was able to recreate these possible fretting wear conditions reasonable well. This was proven by the hysteresis loops and SEM analyses of the extended fretting wear experiments. The three possible fretting contacts encountered in the two aircraft applications were also successfully simulated by the test apparatus. The experimental study also provided sufficient evidence to suggest that the test apparatus is able to perform repeatable and fully controllable fretting wear experiments, giving the operator real time information regarding the key parameters of the fretting wear process.

Moreover, the experimental study showed that a change in the normal force affected the characteristics of the contact of material couples involved in the two aircraft applications. A decrease in the normal force resulted in an increase in the wear scar area, and the static friction coefficient of the Ti-6Al-4V-on-Ti-6L-4V and Al7075-T6-on- Al7075-T6 couples. The extended Ti-6Al-4V-on-Ti-6Al-4V and Al7075-T6-on-Al7075-T6 experiments highlighted that that abrasive wear, oxidation and plastic deformation of adhered layers in the contact zones played significant roles in the fretting wear. These mechanisms can be extremely destructive, especially in precision aerospace applications where a loss of fit or tolerance can have catastrophic consequences.

Additional fretting wear experiments were also conducted between the two aerospace materials and cemented carbides, since the carbides are currently being utilized as coatings in some aerospace contacts that are prone to fretting induced damage.The experimental results of these couples consistently indicated that gross slip, and consequently fretting wear had taken place. SEM analysis of the carbide surfaces however provided no visible evidence that any of the carbide surfaces had experienced wear. The analysis did however show that material was transferred from the Ti-6Al-4V and Al7075-T6 specimens to the respective carbide surfaces. The experimental study also indicated that the Ti-6Al-4V specimens coupled with both of the carbides produced the highest coefficient of static friction, irrespective of the contact configuration. The highest oxidation levels were encountered during the Al7075-T6-on-Al7075-T6, and the Al7075-T6-on-SPS

carbide experiments. These results will provide some additional insights into the interactions between carbide coated surface and counter surfaces in aerospace applications.

6.2 Recommendations

The following recommendations were made for furthering the information already gained from this study:

- Replacing the load cells of the fretting test apparatus with dedicated force transducers. This would allow the fretting test apparatus to operate at fretting frequencies above 100 Hz, whilst still providing reliable experimental data.
- The use of surface profilometry in order to quantify the wear volume loss caused by the fretting process.
- The use of cylindrical carbide pins in order to investigate the fretting wear phenomenon on carbide-on-carbide, carbide-on-Ti-6Al-4V and csrbide-on-Al7075-T6. This would provide sufficient information for decision making in terms of the applicability of carbides to aircraft contacts prone to fretting induced damage.
- Modifying the Force Application Subsystem in order to incorporate dynamic force damping mechanisms. This would counteract any possible resonance within the test apparatus. The proposed modifications to the subsystem are provided in Figure C.1 in Appendix C

References

[1] Kalin M, Vizintin J. Use of equations for wear volume determination in fretting experiments. Wear 2000;237(1):39-48.

[2] Hutchings I M. Tribology: Friction and Wear of Engineering Materials. Kent: Hobber and Stoughton Limited; 1992.

[3] Collins J A. Failure of Materials in Mechanical Design: Analysis, Prediction, Prevention. New York: John Wiley & Sons, Inc.; 1993

[4] Szolwinski M P, Farris T N. Mechanics of fretting fatigue crack formation. Wear 1996; 198(1-2): 93-107.

[5] Bock E M, Whitely J H. Fretting Corrosion in Electric Contacts. In: Twentieth Annual Holm Seminar on Electrical Contacts. Harrisburg: 1974.

[6] Stachowiak G W, Batchelor A W. Engineering Tribology. Boston: Butterworth-Heinemann; 1993: 2nd Edition.

[7] Shankar K, Dhamari R. Fatigue behaviour of aluminium alloy 7075 bolted joints treated with oily film corrosion compounds. Materials and Design 2002;23(2):209-216.

[8] Aggarwal M L, Khan R A, Aggrawal V P. Optimization of micro welds in leaf springs used in aumotive vehicles. Indian Journal of Engineering and Materials Sciences 2006;13: 217-220.

[9] Ratsimba C H H, McColl I R, Williams E J, Leen S B, Soh H P. Measurement, analysis and proediction of fretting wear damage in a representative aeroengine spline coupling. Wear 2004; 257(11): 1193-1206.

[10] Chaplin C R. Failure analysis in wire ropes. Engineering Failure Analysis 1995;2:45-57.

[11] Tillian T E. Failure Atlas for Hertz Contact Machine Elements. New York: American Society of Mechanical Engineers; 1992.

[12] Eden E M, Ross W N, Cunningham F L. The endurance of metals. In: Proceedings of the Institution of Mechanical Engineers: London: 1911; 4 :pp. 839-974.

[13] Tomlinson G A. The Rusting of Steel Surfaces in Contact. In: Proceedings of the Royal Society of London. Series A, Containing Papers of aMathematical and Physical Character: London: 1927; 115: pp. 472-183.

[14] Fillot N, Iordanoff I, Berthier Y. Wear Modelling and the third body concept. Wear 2007; 262(7-8):947-957.

[15] Waterhouse R B, Fretting Corrosion. Oxford: Pergamon Press, 1972.

[16] Hager C H, Sanders J H, Sharma S. Characterization of mixed and gross slip fretting wear regimes in Ti6Al4V interfaces at room temperature. Wear 2007;257(1-2):167-180.

[17] Godet M. The third body approach: a mechanical view of wear. Wear 1984;100(1-3):437-452.

[18] Berthier Y. Maurice Godet's third body. In: Proceedings of the 22nd Leeds-lyon Symposium on Tribology: The Third Body Conceps: Amsterdam: 1996, pp. 21-30.

[19] Bill R C. The Role of Oxidation in the Fretting Wear Process. NASA TM-81570 1980: NASA.

[20] Feng I M, Uhlig H H. Fretting Corrosion of Mild Steel in Air and in Nitrogen,. Journal of Applied Mechanics 1954;21(5): 395-400,.

[21] Fenner A J, Wright K H R, Mann J Y. Fretting Corrosion and its Influence on Fatigue Failure. In: Proceedings of International Conferrence on Fatigue of Metals: 1956, pp. 386-393.

[22] Bill R C. Fretting Wear and Fretting Fatigue - How are They Related . Journal of Lubrication

Technology 1983;105: 230-238.

[23] R B Waterhouse, A Iwabuchi. High Temperature fretting of Four Titanium Alloys. Wear 1985;106(1-3): 229-245.

[24] Waterhouse R B. "Introduction. Wear 1985; (1-3):1-4.

[25] Neyman A. The Influence of Oil Properties on the Fretting Wear of Mild Steel. Wear 1992; 152(1):171-181.

[26] Qiu Y, Roylance B J. The Effect of Lubricant Additives on Frettig Wear. Lubrication Engineering 1992;48:801-808.

[27] Weismantel E E. Friction and Fretting with Solid Film Lubricants. Lubrication Engineering 1955;11: 97-100.

[28 Batchelor A W, Stachowiak G W, Stachowiak G B, Leech P W, Reinhold O. Control of Fretting Friction and Wear of Roping Wire by Laser Surface alloying and Physical Vapour Deposition. Wear 1992;152(1):127-150.

[29] Leech P W, Batchelor A W, Stachowiak G W. Laser Surface Alloying of Steel Wire With Chromium and Zirconium. Journal of Material Science Letters 1992;11:1121-1123.

[30] Hurricks P L, Ashford K S. The Effect of Temperature on the Fretting Wear of Mild Steel. In: Proceedings of the Institute of Mechanical Engoneers 1969-1970;184. pp. 165-175.

[31] Nishioka K, Hirakawa K. Fundamental Investigation of Fretting Fatigue: Part 5, The Effect of Relative Slip Amplitude. Bulletin of Japan Society of Mechanical Engineers 1969;12:692-697.

[32] Vingsbo O, Soderberg S. On fretting maps. Wear 1988;126(2):131-147.

[33] Dobromirski J M. Variable of Freting Process: Are There 50 of Them?. In Attia M H ,Waterhouse R B, editors. Standardization of Fretting Fatgiue Test Methods and Equipment. Philadelphia: American Societ of Testing and Materials; 1992, pp. 60-66.

[34] Mindlin R D. Compliance of elastic bodies in contact. Journal of Applied Mechanics 1949;16: 259-268.

[35] Chen G X, Zhou Z R. Study on transition between fretting and reciprocating sliding wear. Wear 2001;250(1-12):665-672.

[36] Ohmae N, Tsukizoe T. The effect of slip amplitude on fretting. Wear 1974;27(3):281-294.

[37] Farokhi S. Aircraft Propulsion. New York: John Wiley & Sons, Inc.: 2009.

[38] Infante V, Silva J M, de Freitas M, Reis L. Failures analysis of compressor blades of aeroengines due to service. Engineering Failure Analysis 2009;16(4):1118-1125.

[39] Golden P J. Development of a dovetail fretting fatigue for turbine engine materials. International Jounal of Fatigue 2009;31(4):620-628.

[40] Mc Veigh P A, Harish G, Farris T N, Szolwinski M P. Modelling interfacial conditions in nominally flat contacts for application to fretting fatigue of turbine engine components. International Journal of Fatigue 1999;21:S157-S165.

[41] Paulin C, Fouvry S, Deyber S. Wear kinetics of Ti-6Al-4V under constant and variable fretting sliding conditions. Wear 2005;259(1-6)292-299.

[42] Namjoshi S A, Mall S. Fretting behaviour of Ti-6Al-4V under combined high cycle and low cycle fatigue loading. International Journal of Fatigue 2001;23: S455-S461.

[43] Hutson A L, Neslen C, Nicholas T. Characterization of fretting fatigue crack initiation processes in CR Ti-6Al-4V. Tribology International 2003;36(2):133-143.

[44] Fouvry S, Duo P, Perruchant Ph. A quantitative approach of Ti-6Al-4V fretting damage: Friction, wear and crack nucleation. Wear 2004;257(9-10):916-929.

[45] T Nicholas. Critical issues facing in high cycle fatigue. International Journal of Fatigue 1999; 21(9-11):221-231.

[46] Birch P R. A Syudy of Fretting Fatigue in Aircraft Component [unpublished dissertation]. Massachusettes: Massachusettes Institute of Technology: 1998.

[47] Hager Jr C H, Sanders J H, Sharma S. Unlubricated gross slip fretting wear of metallic plasma-sprayed coatings for Ti6Al4V surfaces. Wear 200:265(3-4):439-451.

[48] Sauger E, Fourvy S, Pansonnet L, Kapsa Ph, Martin J M, Vincent L. Tribologically transformed structure in fretting. Wear2000; 249(1-2):39-52.

[49] Chakherlou T N, Mirzajanzadeh M, Vogwell J. Effect of hole lubrication of the fretting fatigue of double shear lap joints: An Experimental and numerical study. Engineering Failure Analysis 2009;16(7):2388-2399.

[50] Majzoobi G H, Hojjati R, Soori M. Fretting fatigue behavior of Al7075-T6 at sub-zero temperature. Tribology International 2011; doi: 10.1016/j.triboint.2011.03.021.

[51] Paulin C, Fouvry S, Deyber S. Wear Kinematics of Ti-6Al-4V under constant and variable fretting sliding conditions. Wear 2005;259:292-299.

[52] Fouvry S, Vincent L, Kapsa P. Quantification of fretting damage. Wear1996;200(1-2):186-205.

[53] Waterhouse R B. The Problems of Fretting Fatigue Testing. In Attia M H ,Waterhouse R B, editors. Standardization of Fretting Fatgiue Test Methods and Equipment. Philadelphia: American Societ of Testing and Materials: 1992. pp. 13-19.

[54] Soderberg S, Bryggman U, McCullough T. Frequency Effects in FrettingWear. Wear 1986; 110(1): 19-34.

[55] Uhlig H H. Mechanism of fretting corrosion. Journal of Applied Mechanics 1966;31(4):401-407.

[56] Waterhouse R B. Fretting. Treatise on Material Science and Technology 1979;13:259-285.

[57] Bryggmann U, Soderberg S. Contact Conditions in Fretting. Wear 1986;110(1):1-17.

[58] Toth L. The investigation of the steady state of steel fretting,. Wear 1972;20(3):277-283.

[59] APC. Piezoelectric Ceramics: Principles and Applications. Pennsylvania: APC International Ltd.

[60] Preloaded Piezo Actuators (LVPZT) with Sensor Option. [Online][s.a.][acessed 2010, June 16]: Available: http://www.physikinstrumente.com/en/pdf/P842_Datasheet.pdf.

[61] Controller, Piezo System; High Power Amplifier Modules; USB Interface Module, Servo Module. [Online][s.a.][acessed 2010, June 16]: Available: **Error! Hyperlink reference not valid.**

[62] QuantumX MX410. [Online][s.a.][acessed 2010, August 22]: Available: http://www.hbm.com/fileadmin/mediapool/hbmdoc/technical/b2612.pdf.

[63] Jaffery S I, Mativenga P T. Assessment of the machinability of Ti-6Al-4V alloy using the wear map approach. International Journal of Advanced Manufufacturing Technology 2009;40: 687–696.

[64] Hughes J I, Sharman A R, Ridgway K. The effect of cutting tool material and edge geometry on tool life and workpiece surface integrity. IN: Proceedings of the Institution of Mechanical Engineers, Part B: Journal of Engineering Manufacture 2006;220. pp. 93–107.

[65] Su Y, He N, Li L, Li X L. An experimental investigation of effects of cooling/lubrication conditions on tool wear in high-speed end milling of Ti-6Al-4V. Wear 2006;261(7-8):760-766.

[66] Shen Y, Zhang D, Duan J, Wang D. Fretting wear behaviors of steel wires underfriction increasing grease conditions. Tribology Internation 2010; vol. doi:10.1016/j.triboint.2010.10.021.

[67] ASM Aerospace Specification Metals Inc. [Online][s.a.][acessed 2011, April 12]: Available:http://asm.matweb.com/search/SpecificMaterial.asp?bassnum=MA7075T6

[68] Otsuka A, Tohgo K, Matsuyama H. Fatigue carck initiation and growth under mixed mode loading in Aluminium Alloys 2017-T3 and 7075-T6. Engineering Fracture Mechanics 1987; 28(5-6):721-732.

[69] Lassner E, Schubert W D, Tungsten: Properties, Chemistry, Technology of the Element, Alloys, and Chemical Compounds. New York: Kluwer Academic/Plenum Publishers; 1999.

[70] Campbell P Q, Celis J P, Roos J R, Van Der Biest O. Fretting wear of selected ceramics and cerments. Wear 1994;174:47-56.

[71] Voevodin A A, O'Neill J P, Zabinski J S. Nonocomposite tribological coatings for aerospace applications. Surface and Coatings Tchnolog 1999y;116-119:36-45.

[72] Donnet C. Recent Progress on the tribology of doped diamond-like and carbon alloy coatings: a review. Surface and Coatingsb Technology 1998;100-101:180-186.

[73] Schell J D, Taylor K P. Wear of Jet Engine Components. In ASM Handbook: Friction, Lubrication and Wear Technology. USA: ASM International; 1992, pp. 588-592.

[74] Zhou Z, Sauger E, Liu J, Vincent L. Nucleation and early growth of tribologically transformed structure induced fretting. Wear 1997;212(1):50-58.

[75] Sauger E, Fouvry S, Ponsonnet L, Ph. Kapsa, J. M. Martin, L. Vincent., "Tribologically transformed structure in fretting," Wear, vol. 245(1-2), pp. 39-52, 2000.

[76] I Cha Seung, H Hong Soon, and K Kim Byung, "Spark plama sintering behaviour of nanocrystaline WC-10Co cemented carbide powders," Materials Sience and Engineering , vol. A351, pp. 31-38, 2003.

A APPENDIX A

Function Name: **static_vs_dynamic**

```
%Function Name:          static_vs_dynamic
%Program Function:       To calculate and plot the coefficient of static friction
%                        versus the coefficient of dynamic friction

%%%%%%%%%%%%%%%%%%%%%%%%%%40N experiment%%%%%%%%%%%%%%%%%%%%%%%%%%%%%%%%%%

N1 =  200000:            %number of fretting cycles for the 40N experiment

for i = 1 : N1

    TempNormForce(1:30,1) = 9.81 * x1((((i-1)*30)+1):(((i-1)*30)+30),4);
    TempTanForce = 9.81 * x1((((i-1)*30)+1):(((i-1)*30)+30),5);

    SumNormForce = 0;           %Variable initialization
    SumTanForce = 0;            %Variable initialization

    MaxTanForce = 0;            %Variable initialization
    MinTanForce = 0;            %Variable initialization

    Output.MinMax(i, 1) = min(TempTanForce);  %Minimum tangential force per
cycle
    Output.MinMax(i, 2) = max(TempTanForce);  %Maximum tangential force per
cycle

    for j = 1 : 30

        SumTanForce = SumTanForce + abs(TempTanForce(j, 1));
        SumNormForce = SumNormForce + TempNormForce(j, 1);

    end

    Output.Normal(i, 1) = SumNormForce / 30;                %Average normal
force per fretting cycle

    Output.TangentDynamic(i, 1) = SumTanForce / 30;         %Average Tangential
force per fretting cycles

    Output.TangentStatic(i, 1) = (abs(Output.MinMax(i, 1)) + Output.MinMax(i,
2)) / 2;  %Static force for each cycle

    Output.StaticFriction(i, 1) =Output.TangentStatic(i, 1) / Output.Normal(i,
1);   %Coefficient of static friction

    Output.DynamicFriction(i, 1) = Output.TangentDynamic(i, 1) /
Output.Normal(i, 1); %Coefficient of dynamic friction
end

% Comand to plots the coefficient of static friction versus the coefficient
% of dynamic friction


plot(Output.StaticFriction(:, 1), 'g');             %plot coefficient of static
friction
```

```
xlabel('Cycle Number');
ylabel('Friction Coefficient');
hold on
plot( Output.DynamicFriction(i, 1), 'r');            %plot coefficient of
dynamic friction
hold off

%End of Function%
```

Function Name: **normal_force_comparison**

```
%Function Name:         normal_force_comparison
%Program Function:      To calculate the coefficient of static friction
%                       for the 40N, 30N and 20N experiments

%%%%%%%%%%%%%%%%%%%%%%%%%%40N experiment%%%%%%%%%%%%%%%%%%%%%%%%%%%%%%%%

N1 =  200000:           %number of fretting cycles for the 40N experiment

for i = 1 : N1

    TempNormForce(1:30,1) = 9.81 * x1((((i-1)*30)+1):(((i-1)*30)+30),4);
    TempTanForce = 9.81 * x1((((i-1)*30)+1):(((i-1)*30)+30),5);

    SumNormForce = 0;           %Variable initialization
    SumTanForce = 0;            %Variable initialization

    MaxTanForce = 0;            %Variable initialization
    MinTanForce = 0;            %Variable initialization

    Output.MinMax(i, 1) = min(TempTanForce);  %Minimum tangential force per
cycle
    Output.MinMax(i, 2) = max(TempTanForce);  %Maximum tangential force per
cycle

    for j = 1 : 30

        SumTanForce = SumTanForce + abs(TempTanForce(j, 1));
        SumNormForce = SumNormForce + TempNormForce(j, 1);

    end

    Output.Normal(i, 1) = SumNormForce / 30;               %Average normal
force per fretting cycle

    Output.TangentDynamic(i, 1) = SumTanForce / 30;        %Average Tangential
force per fretting cycles

    Output.TangentStatic(i, 1) = (abs(Output.MinMax(i, 1)) + Output.MinMax(i,
2)) / 2;  %Static force for each cycle

    Output.StaticFriction(i, 1) =Output.TangentStatic(i, 1) / Output.Normal(i,
1);   %Coefficient of static friction

    Output.DynamicFriction(i, 1) = Output.TangentDynamic(i, 1) /
Output.Normal(i, 1); %Coefficient of dynamic friction
end
```

```
%%%%%%%%%%%%%%%%%%%%%%%%%30N experiment%%%%%%%%%%%%%%%%%%%%%%%%%%%%%%%%%%

N2 =  200000;               %number of fretting cycles for the 30N experiment

for i = 1 : N2

    TempNormForce2(1:30,1) = 9.81 * x2((((i-1)*30)+1):(((i-1)*30)+30),4);
    TempTanForce2 = 9.81 * x2((((i-1)*30)+1):(((i-1)*30)+30),5);

    SumNormForce2 = 0;           %Variable initialization
    SumTanForce2 = 0;            %Variable initialization

    MaxTanForce2 = 0;            %Variable initialization
    MinTanForce2 = 0;            %Variable initialization

    Output.MinMax2(i, 1) = min(TempTanForce2);  %Minimum tangential force per
cycle
    Output.MinMax2(i, 2) = max(TempTanForce2);  %Maximum tangential force per
cycle

    for j = 1 : 30

        SumTanForce2 = SumTanForce2 + abs(TempTanForce2(j, 1));
        SumNormForce2 = SumNormForce2 + TempNormForce2(j, 1);

    end

    Output.Normal2(i, 1) = SumNormForce2 / 30;                %Average normal
force per fretting cycle

    Output.TangentDynamic2(i, 1) = SumTanForce2/ 30;         %Average Tangential
force per fretting cycles

    Output.TangentStatic2(i, 1) = (abs(Output.MinMax2(i, 1)) + Output.MinMax2(i,
2)) / 2;  %Static force for each cycle

    Output.StaticFriction2(i, 1) =Output.TangentStatic2(i, 1) /
Output.Normal2(i, 1);   %Coefficient of static friction

    Output.DynamicFriction2(i, 1) = Output.TangentDynamic2(i, 1) /
Output.Normal2(i, 1); %Coefficient of dynamic friction
end

%%%%%%%%%%%%%%%%%%%%%%%%%20N experiment%%%%%%%%%%%%%%%%%%%%%%%%%%%%%%%%%%

N3 =  200000;           %number of fretting cycles for the 20N experiment

for i = 1 : N3

    TempNormForce3(1:30,1) = 9.81 * x3((((i-1)*30)+1):(((i-1)*30)+30),4);
    TempTanForce3 = 9.81 * x3((((i-1)*30)+1):(((i-1)*30)+30),5);

    SumNormForce3 = 0;          %Variable initialization
    SumTanForce3 = 0;           %Variable initialization

    MaxTanForce3 = 0;           %Variable initialization
    MinTanForce3 = 0;           %Variable initialization
```

```
    Output.MinMax3(i, 1) = min(TempTanForce3);  %Minimum tangential force per
cycle
    Output.MinMax3(i, 2) = max(TempTanForce3);  %Maximum tangential force per
cycle

    for j = 1 : 30

        SumTanForce3 = SumTanForce3 + abs(TempTanForce3(j, 1));
        SumNormForce3 = SumNormForce3 + TempNormForce3(j, 1);

    end

    Output.Normal3(i, 1) = SumNormForce3 / 30;                %Average normal
force per fretting cycle

    Output.TangentDynamic3(i, 1) = SumTanForce3/ 30;         %Average Tangential
force per fretting cycles

    Output.TangentStatic3(i, 1) = (abs(Output.MinMax3(i, 1)) + Output.MinMax3(i,
2)) / 2;  %Static force for each cycle

    Output.StaticFriction3(i, 1) =0.8*Output.TangentStatic3(i, 1) /
Output.Normal3(i, 1);   %Coefficient of static friction

    Output.DynamicFriction3(i, 1) = Output.TangentDynamic3(i, 1) /
Output.Normal3(i, 1); %Coefficient of dynamic friction
end

%Command to print the coefficient of static friction graphs of all three
%experiments

figure(1)
plot(Output.StaticFriction(:, 1), 'g');
xlabel('Cycle Number');
ylabel('Friction Coefficient');
hold on
plot( Output.StaticFriction2(:, 1), 'b');
hold on
plot(Output.StaticFriction3(:, 1), 'r');
hold off

%End of function%
```

Function Name: **10^6_cycle_experimetns**

```
%Function Name:         10^6_cycle_experimetns
%Program Function:      To calculate the coefficient of static friction
%                       for 10^6 cycle experiments

%0 to 200000 Cycles%

N1 =  200000:

for i = 1 : N1

    TempNormForce(1:30,1) = 9.81 * x1((((i-1)*30)+1):(((i-1)*30)+30),4);
    TempTanForce = 9.81 * x1((((i-1)*30)+1):(((i-1)*30)+30),5);
```

```
    SumNormForce = 0;           %Variable initialization
    SumTanForce = 0;            %Variable initialization

    MaxTanForce = 0;            %Variable initialization
    MinTanForce = 0;            %Variable initialization

    Output.MinMax(i, 1) = min(TempTanForce);  %Minimum tangential force per
cycle
    Output.MinMax(i, 2) = max(TempTanForce);  %Maximum tangential force per
cycle

    for j = 1 : 30

        SumTanForce = SumTanForce + abs(TempTanForce(j, 1));
        SumNormForce = SumNormForce + TempNormForce(j, 1);

    end

    Output.Normal(i, 1) = SumNormForce / 30;                %Average normal
force per fretting cycle

    Output.TangentDynamic(i, 1) = SumTanForce / 30;         %Average Tangential
force per fretting cycles

    Output.TangentStatic(i, 1) = (abs(Output.MinMax(i, 1)) + Output.MinMax(i,
2)) / 2;  %Static force for each cycle

    Output.StaticFriction(i, 1) =Output.TangentStatic(i, 1) / Output.Normal(i,
1);   %Coefficient of static friction

    Output.DynamicFriction(i, 1) = Output.TangentDynamic(i, 1) /
Output.Normal(i, 1); %Coefficient of dynamic friction
end

%225000 to 400000 Cycles%

N2 =  175000;

for i = 1 : N2

    TempNormForce2(1:30,1) = 9.81 * x2((((i-1)*30)+1):(((i-1)*30)+30),4);
    TempTanForce2 = 9.81 * x2((((i-1)*30)+1):(((i-1)*30)+30),5);

    SumNormForce2 = 0;          %Variable initialization
    SumTanForce2 = 0;           %Variable initialization

    MaxTanForce2 = 0;           %Variable initialization
    MinTanForce2 = 0;           %Variable initialization

    Output.MinMax2(i, 1) = min(TempTanForce2);  %Minimum tangential force per
cycle
    Output.MinMax2(i, 2) = max(TempTanForce2);  %Maximum tangential force per
cycle

    for j = 1 : 30

        SumTanForce2 = SumTanForce2 + abs(TempTanForce2(j, 1));
```

```
 SumNormForce2 = SumNormForce2 + TempNormForce2(j, 1);

    end

    Output.Normal2(i, 1) = SumNormForce2 / 30;                %Average normal
force per fretting cycle

    Output.TangentDynamic2(i, 1) = SumTanForce2/ 30;         %Average Tangential
force per fretting cycles

    Output.TangentStatic2(i, 1) = (abs(Output.MinMax2(i, 1)) + Output.MinMax2(i,
2)) / 2;  %Static force for each cycle

    Output.StaticFriction2(i, 1) =Output.TangentStatic2(i, 1) /
Output.Normal2(i, 1);   %Coefficient of static friction

    Output.DynamicFriction2(i, 1) = Output.TangentDynamic2(i, 1) /
Output.Normal2(i, 1); %Coefficient of dynamic friction
end

%425000 to 600000 Cycles%

N3 =  175000;

for i = 1 : N3

    TempNormForce3(1:30,1) = 9.81 * x3((((i-1)*30)+1):(((i-1)*30)+30),4);
    TempTanForce3 = 9.81 * x3((((i-1)*30)+1):(((i-1)*30)+30),5);


    SumNormForce3 = 0;          %Variable initialization
    SumTanForce3 = 0;           %Variable initialization

    MaxTanForce3 = 0;           %Variable initialization
    MinTanForce3 = 0;           %Variable initialization

    Output.MinMax3(i, 1) = min(TempTanForce3);  %Minimum tangential force per
cycle
    Output.MinMax3(i, 2) = max(TempTanForce3);  %Maximum tangential force per
cycle

    for j = 1 : 30

        SumTanForce3 = SumTanForce3 + abs(TempTanForce3(j, 1));
        SumNormForce3 = SumNormForce3 + TempNormForce3(j, 1);

    end

    Output.Normal3(i, 1) = SumNormForce3 / 30;                %Average normal
force per fretting cycle

    Output.TangentDynamic3(i, 1) = SumTanForce3/ 30;         %Average Tangential
force per fretting cycles

    Output.TangentStatic3(i, 1) = (abs(Output.MinMax3(i, 1)) + Output.MinMax3(i,
2)) / 2;  %Static force for each cycle

    Output.StaticFriction3(i, 1) =Output.TangentStatic3(i, 1) /
Output.Normal3(i, 1);   %Coefficient of static friction
```

```
    Output.DynamicFriction3(i, 1) = Output.TangentDynamic3(i, 1) /
Output.Normal3(i, 1); %Coefficient of dynamic friction
end

%625000 to 800000 Cycles%

N4 =  175000;

for i = 1 : N4

    TempNormForce4(1:30,1) = 9.81 * x4((((i-1)*30)+1):(((i-1)*30)+30),4);
    TempTanForce4 = 9.81 * x4((((i-1)*30)+1):(((i-1)*30)+30),5);

    SumNormForce4 = 0;          %Variable initialization
    SumTanForce4 = 0;           %Variable initialization

    MaxTanForce4 = 0;           %Variable initialization
    MinTanForce4 = 0;           %Variable initialization

    Output.MinMax4(i, 1) = min(TempTanForce4);  %Minimum tangential force per
cycle
    Output.MinMax4(i, 2) = max(TempTanForce4);  %Maximum tangential force per
cycle

    for j = 1 : 30

        SumTanForce4 = SumTanForce4 + abs(TempTanForce4(j, 1));
        SumNormForce4 = SumNormForce4 + TempNormForce4(j, 1);

    end

    Output.Normal4(i, 1) = SumNormForce4 / 30;               %Average normal
force per fretting cycle

    Output.TangentDynamic4(i, 1) = SumTanForce4/ 30;         %Average Tangential
force per fretting cycles

    Output.TangentStatic4(i, 1) = (abs(Output.MinMax4(i, 1)) + Output.MinMax4(i,
2)) / 2;  %Static force for each cycle

    Output.StaticFriction4(i, 1) =Output.TangentStatic4(i, 1) /
Output.Normal4(i, 1);   %Coefficient of static friction

    Output.DynamicFriction4(i, 1) = Output.TangentDynamic4(i, 1) /
Output.Normal4(i, 1); %Coefficient of dynamic friction
end

%825000 to 1000000 Cycles%

N5 =  175000;

for i = 1 : N5

    TempNormForce5(1:30,1) = 9.81 * x5((((i-1)*30)+1):(((i-1)*30)+30),4);
    TempTanForce5 = 9.81 * x5((((i-1)*30)+1):(((i-1)*30)+30),5);


    SumNormForce5 = 0;          %Variable initialization
```

```
    SumTanForce5 = 0;           %Variable initialization

    MaxTanForce5 = 0;           %Variable initialization
    MinTanForce5 = 0;           %Variable initialization

    Output.MinMax5(i, 1) = min(TempTanForce5);  %Minimum tangential force per
cycle
    Output.MinMax5(i, 2) = max(TempTanForce5);  %Maximum tangential force per
cycle

    for j = 1 : 30

        SumTanForce5 = SumTanForce5 + abs(TempTanForce5(j, 1));
        SumNormForce5 = SumNormForce5 + TempNormForce5(j, 1);

    end

    Output.Normal5(i, 1) = SumNormForce5 / 30;               %Average normal
force per fretting cycle

    Output.TangentDynamic5(i, 1) = SumTanForce5/ 30;         %Average Tangential
force per fretting cycles

    Output.TangentStatic5(i, 1) = (abs(Output.MinMax5(i, 1)) + Output.MinMax5(i,
2)) / 2;  %Static force for each cycle

    Output.StaticFriction5(i, 1) =Output.TangentStatic5(i, 1) /
Output.Normal5(i, 1);   %Coefficient of static friction

    Output.DynamicFriction5(i, 1) = Output.TangentDynamic5(i, 1) /
Output.Normal5(i, 1); %Coefficient of dynamic friction
end

c1=1:200000;                          %Counter 1
c2=225001:400000;                     %Counter 2
c3=425001:600000;                     %Counter 3
c4=625001:800000;                     %Counter 4
c5=825001:1000000;                    %Counter 5

figure(1)
plot(c1,Output.StaticFriction(:, 1), 'b');           %Plot 0 to 200000 Cycles
xlabel('Cycle Number');
ylabel('Friction Coefficient');
hold on
plot( c2,Output.StaticFriction2(:, 1), 'b');           %Plot 225000 to 400000
Cycles
hold on
plot( c3,Output.StaticFriction3(:, 1), 'b');           %Plot 425000 to 600000
Cycles
hold on
plot( c4,Output.StaticFriction4(:, 1), 'b');           %Plot 625000 to 800000
Cycles
hold on
plot( c5,Output.StaticFriction5(:, 1), 'b');           %Plot 825000to 1000000
Cycles
hold off

%End of Function%
```

B APPENDIX B

B.1 Fretting Wear in Aircraft Turbo Machinery

B.1.1 Cylinder-on-flat Ti-6Al-4V Fretting Contact Subjected to Axial Motion

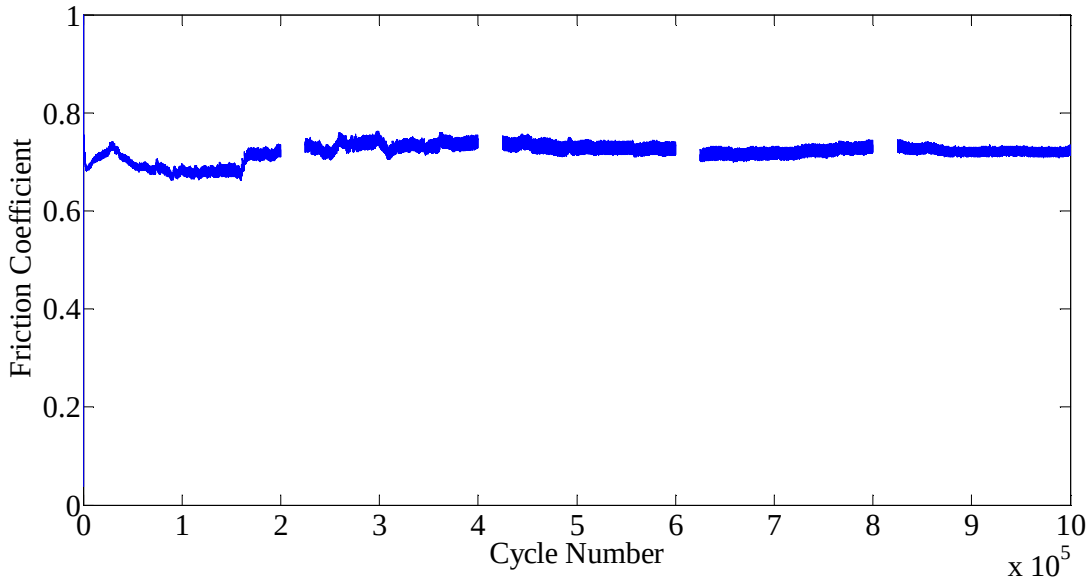

Figure B.1: Coefficient of friction for Ti-6Al-4V cylinder on Ti-6Al-4V flat subjected to axial motion [Frequency = 80Hz, Slip (peak-to-peak) = 100 micro meter; Cycles = 1000000]

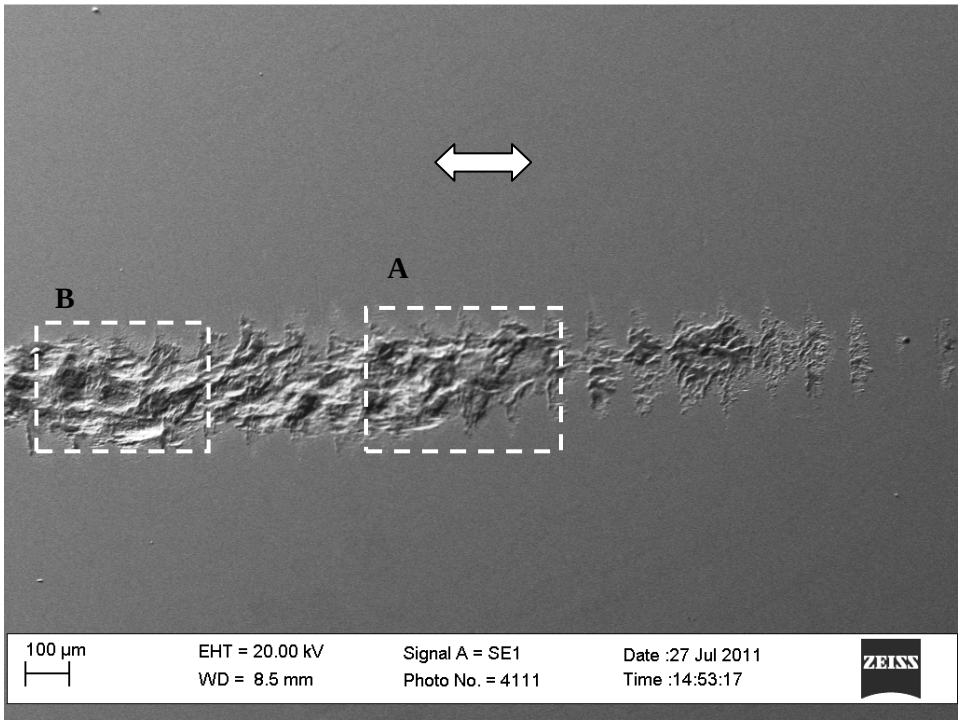

Figure B.2: SEM image of the wear scar on the flat Ti-6Al-4V specimen produced by the cylinder-on-flat Ti-6Al-4V fretting contact subjected to axial motion

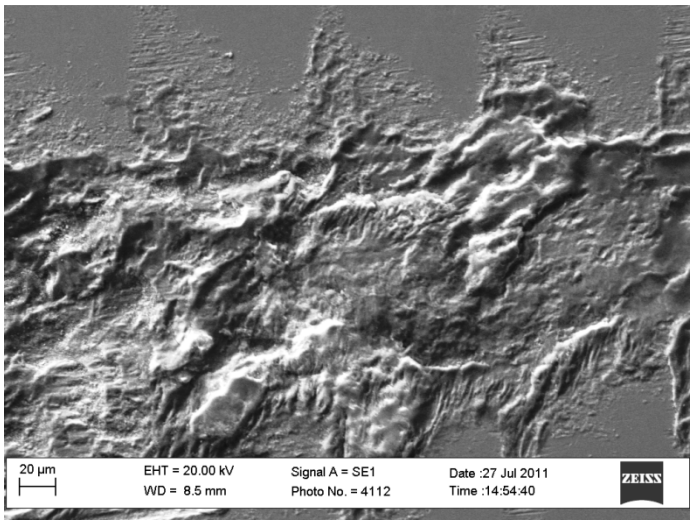

(a)

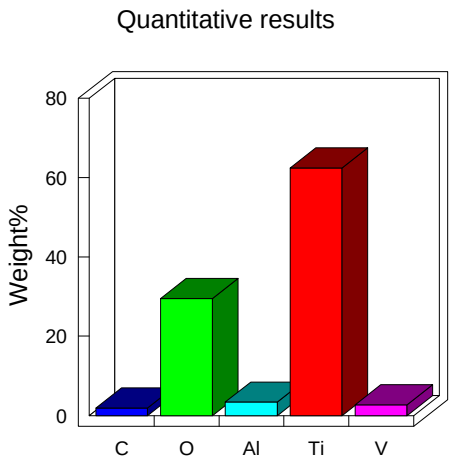

(b)

Figure B.3: SEM image and EDAX analysis results taken at area B in Figure B.2: (a) SEM image; (b) quantitative EDX analysis from image

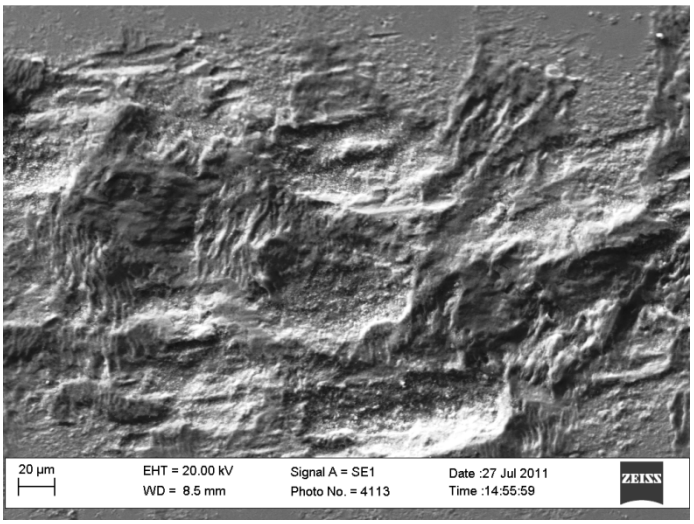

(a)

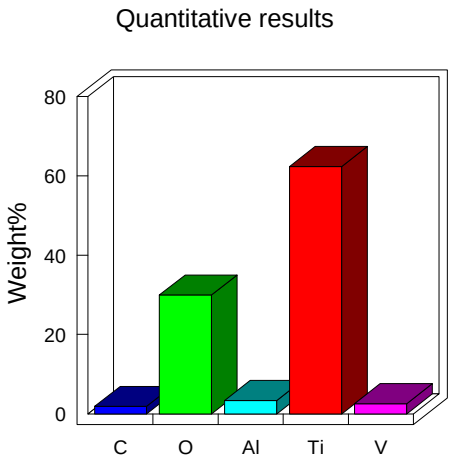

(b)

Figure B.4: SEM image and EDAX analysis results taken at area A in Figure B.2: (a) SEM image; (b) quantitative EDX analysis from image

Table B.1: Summary of the three quantitative EDX analyses performed on the SEM images in Figure B.2, Figure B.3 and Figure B.4

	Weight%				
Figure	**O**	**Al**	**Ti**	**V**	**Total**
Figure B.2	0	5.102	91.412	3.486	100.000
Figure B.3	31.457	3.362	62.467	2.714	100.000
Figure B.4	31.785	3.322	62.361	2.531	100.000

B.1.2 Flat-on-Flat Ti-6Al-4V Fretting Contact Subjected to Fretting Motion

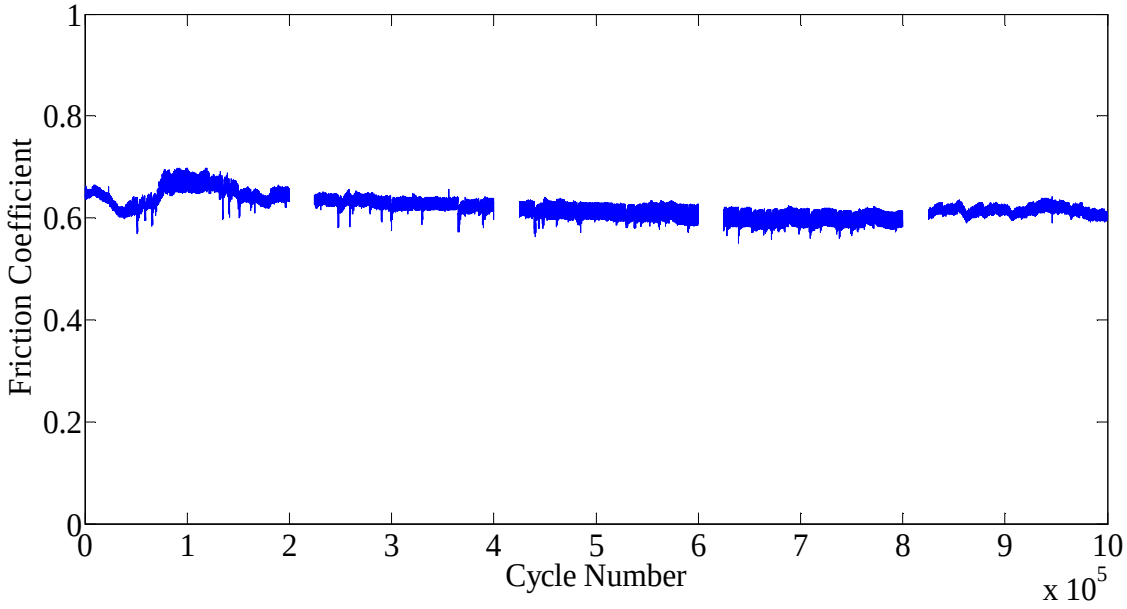

Figure B.5: Coefficient of static friction for Ti-6Al-4V flat-on-flat fretting contact subjected to fretting motion [Frequency = 80Hz, Slip (peak-to-peak) = 100 micro meter; Cycles = 1000000]

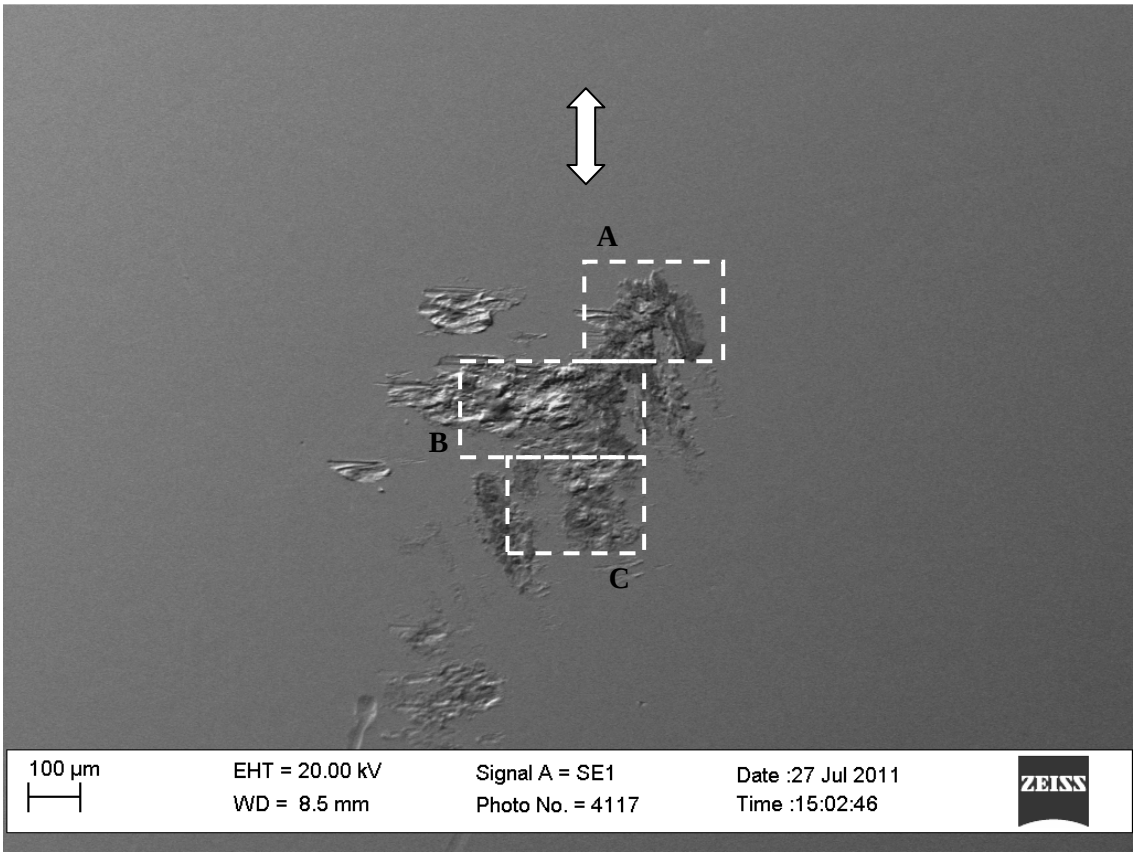

Figure B.6: SEM image of the wear scar on the flat Ti-6Al-4V flat-on-flat fretting contact subjected to fretting motion

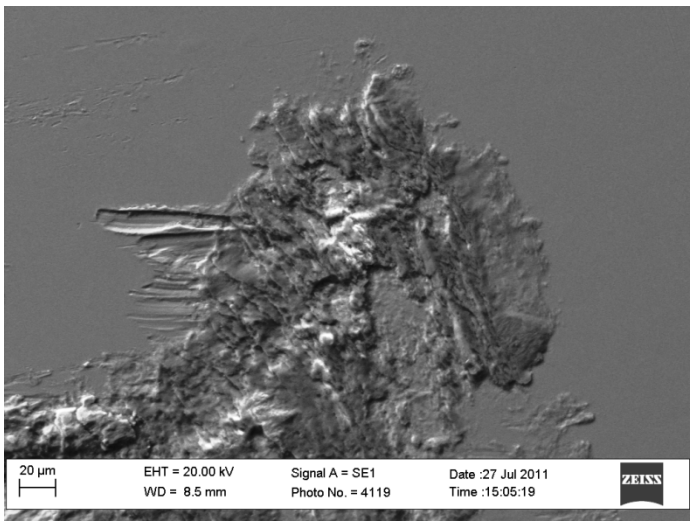

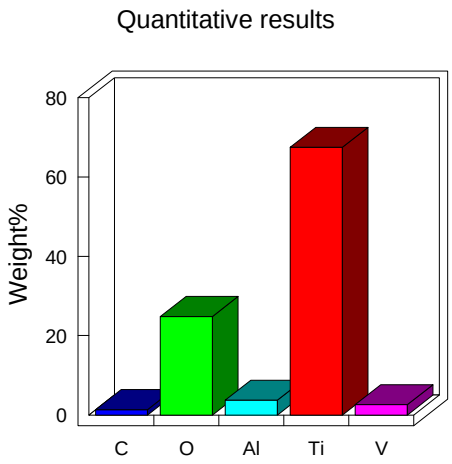

(a) (b)

Figure B.7: SEM image and EDAX analysis results taken at area A in Figure B.6: (a) SEM image; (b) quantitative EDX analysis from image

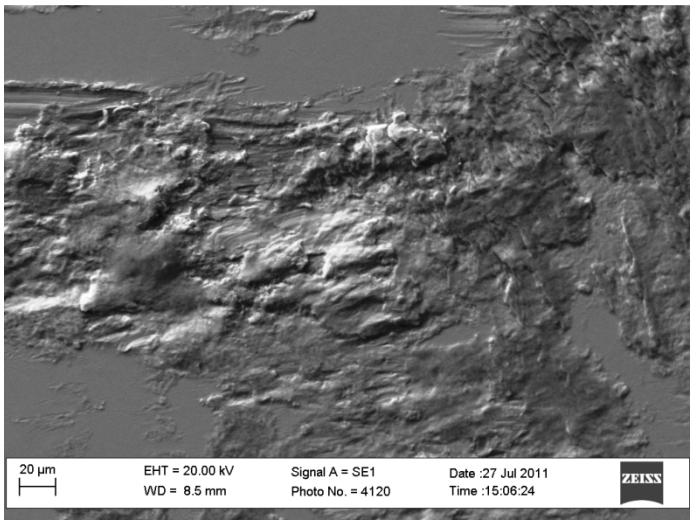

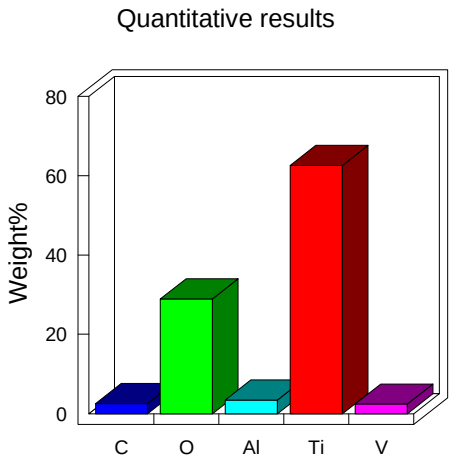

(a) (b)

Figure B.8: SEM image and EDAX analysis results taken at area B in Figure B.6: (a) SEM image; (b) quantitative EDX analysis from image

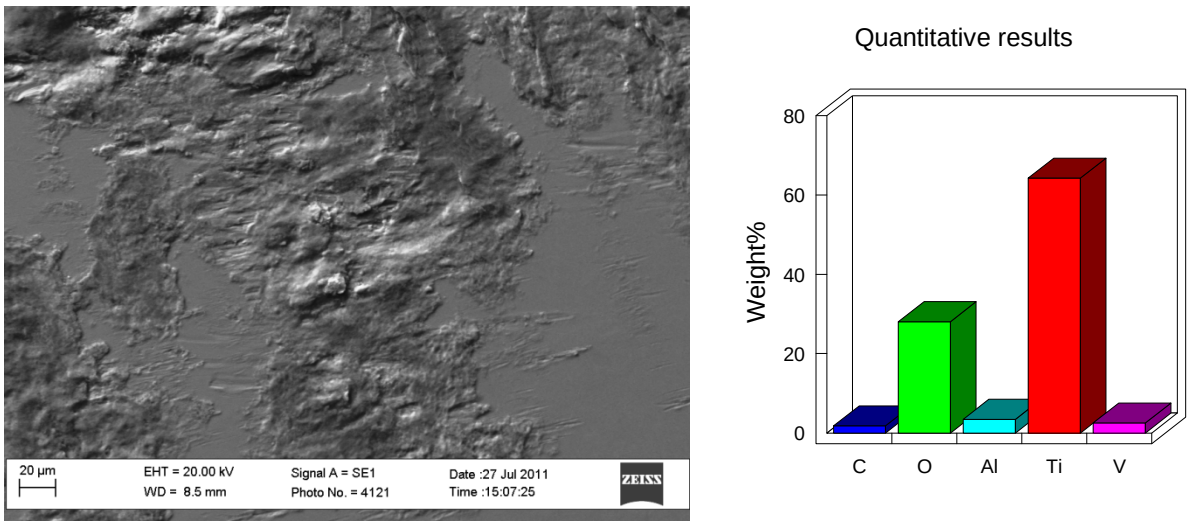

(a) (b)

Figure B.9: SEM image and EDAX analysis results taken at area C in Figure B.6: (a) SEM image; (b) quantitative EDX analysis from image

Table B.2: Summary of the three quantitative EDX analyses performed on the SEM images in Figure B.2, Figure B.8 and Figure B.9

	Weight%					
Figure	**C**	**O**	**Al**	**Ti**	**V**	**Total**
Figure B.7	1.383	24.822	3.722	67.494	2.579	100.000
Figure B.8	2.545	28.973	3.466	62.589	2.427	100.000
Figure B.9	1.763	28.020	3.416	64.312	2.490	100.000

B.2 Fretting Wear in Aircraft Structural Joints

B.2.1 Cylinder-on-Flat Al7075-T6 Fretting Contact Subjected to Tangential Motion

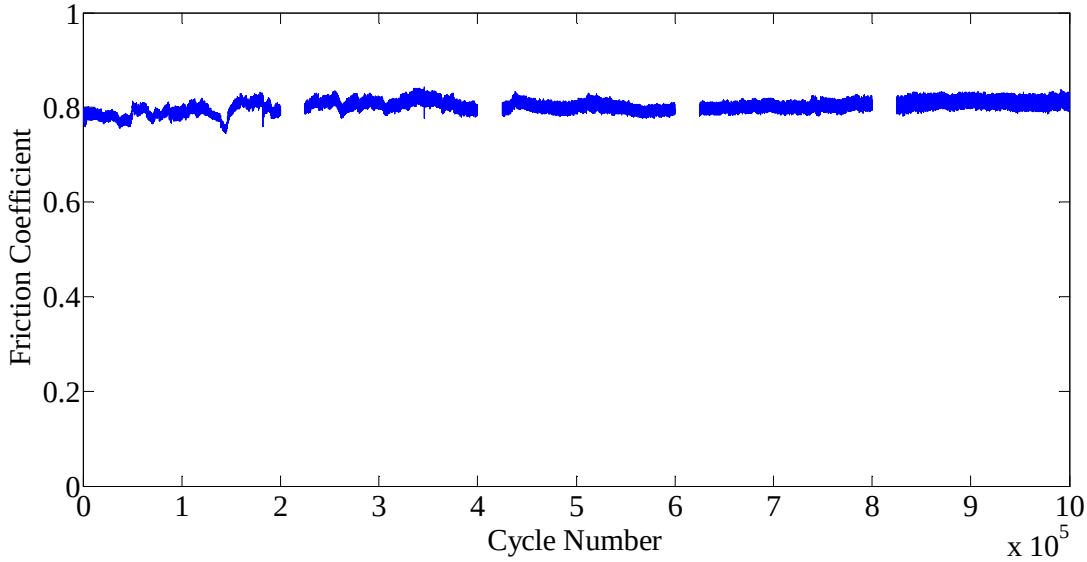

Figure.B.10: Coefficient of friction for Al7075-T6 cylinder on Al7075-T6 flat subjected to tangential motion [Frequency = 80Hz, Slip (peak-to-peak) = 100 micro meter; Cycles = 1000000]

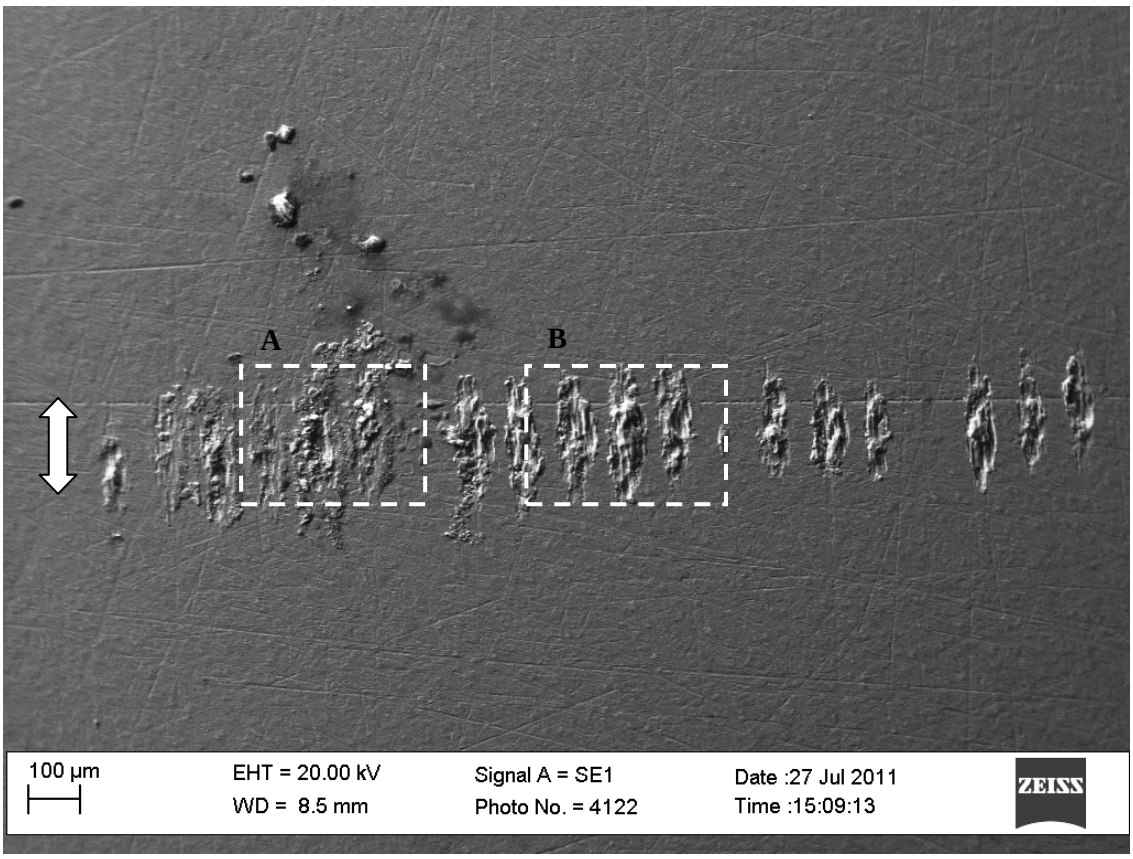

Figure.B.11: SEM image of the wear scar on the flat Al7075-T6 specimen produced by the cylinder-on-flat Al7075-T6 fretting contact subjected to tangential motion

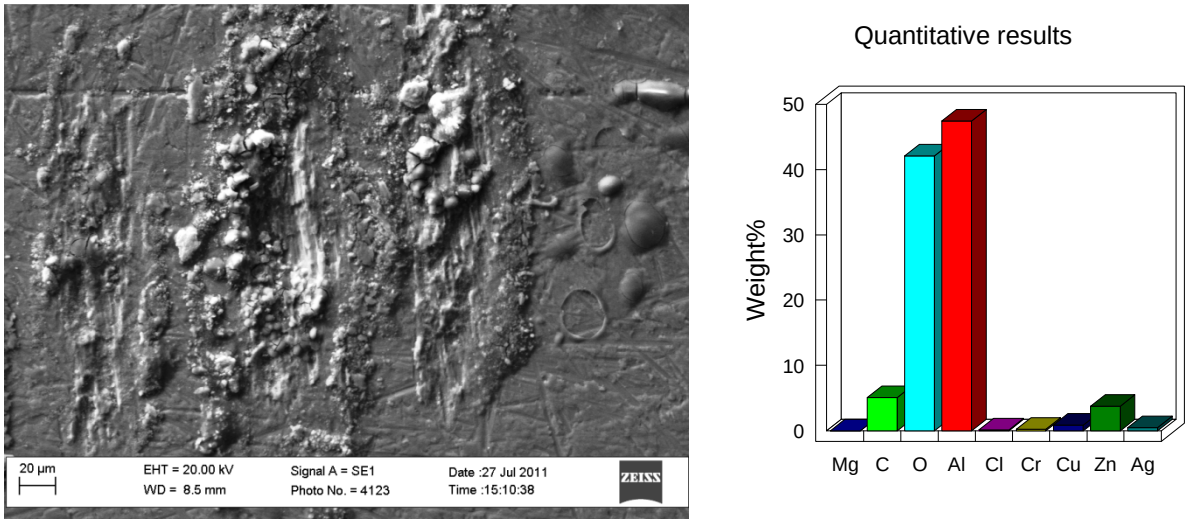

(a) (b)

Figure.B.12: SEM image and EDAX analysis results taken at area A in Figure.B.11: (a) SEM image; (b) quantitative EDX analysis from image

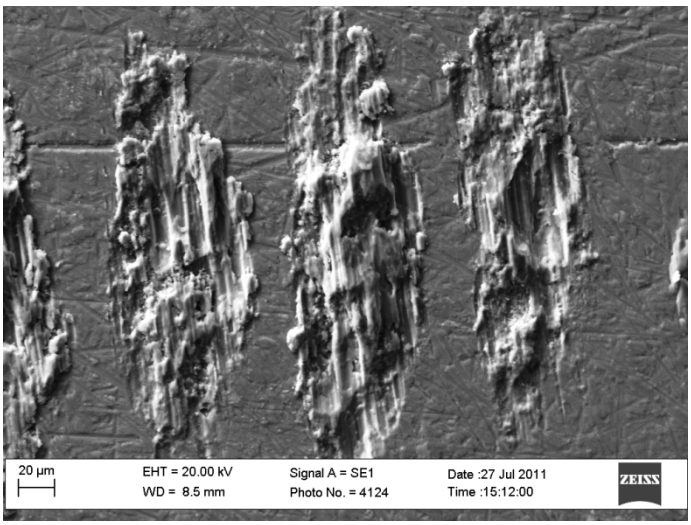

(a)

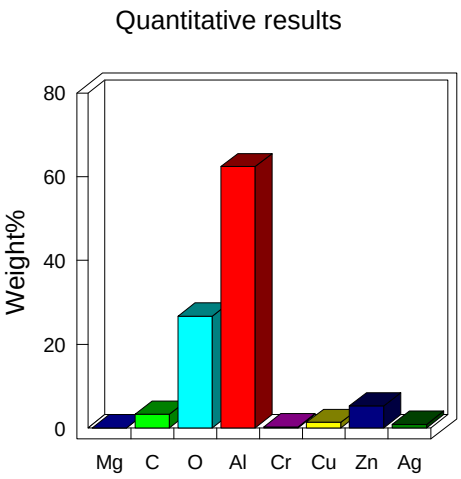

(b)

Figure B.13: SEM image and EDAX analysis results taken at area B in Figure.B.11: (a) SEM image; (b) quantitative EDX analysis from image

Table.B.3: Summary of the three quantitative EDX analyses performed on the SEM images in Figure.B.11, Figure.B.12 and Figure B.13

	Weight%								
Figure	**C**	**O**	**Al**	**Cl**	**Cr**	**Cu**	**Zn**	**Ag**	**Total**
Figure.B.11	5.0392	10.691	76.660	0	0.24990	1.3984	5.3793	0.58088	100
Figure.B.12	5.0546	42.116	47.435	0.1120	0.1969	0.8732	3.7376	0.4732	100
Figure B.13	6.703	21.580	64.142	0.1727	0.17357	1.1979	5.2034	0.8262	100

B.3 Fretting Wear of Conventionally Sintered Carbides

B.3.1 Ti-6Al-4V Cylinder on a WC-10wt%Co Flat Fretting Contact Subjected to Axial Motion

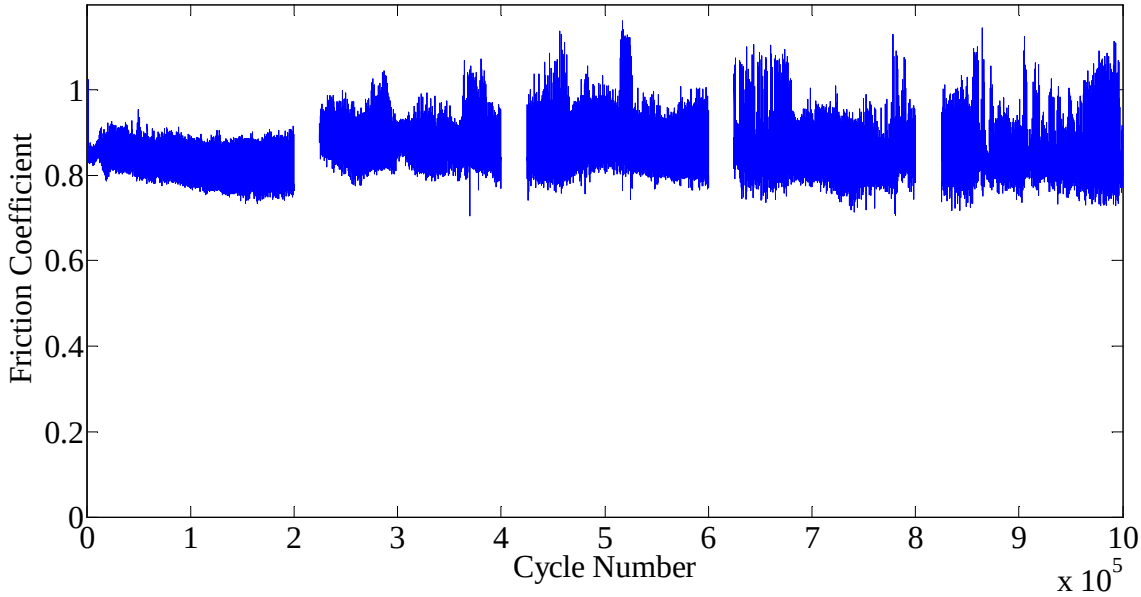

Figure B.14: Coefficient of friction for a Ti-6Al-4V cylinder on a WC-10wt%Co flat fretting contact subjected to axial motion [Normal force = 20N, Frequency = 80Hz, Slip (peak-to-peak) = 100 μm; Cycles = 1000000]

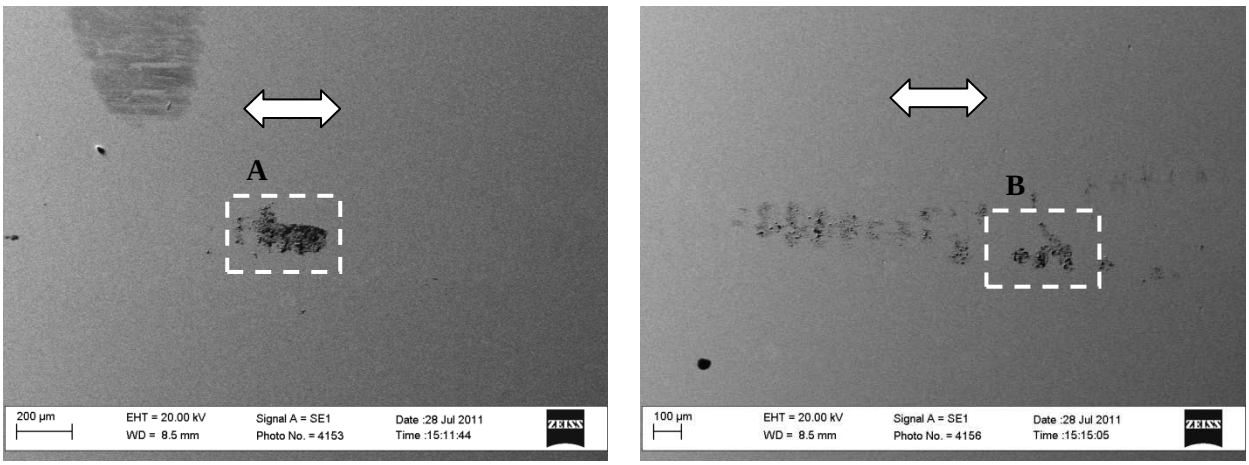

(a) (b)

Figure B.15: Two SEM images of the wear scar on the flat WC-10wt%Co specimen produced by the Ti-6Al-4V cylinder on WC-10wt%Co flat fretting contact subjected to axial motion

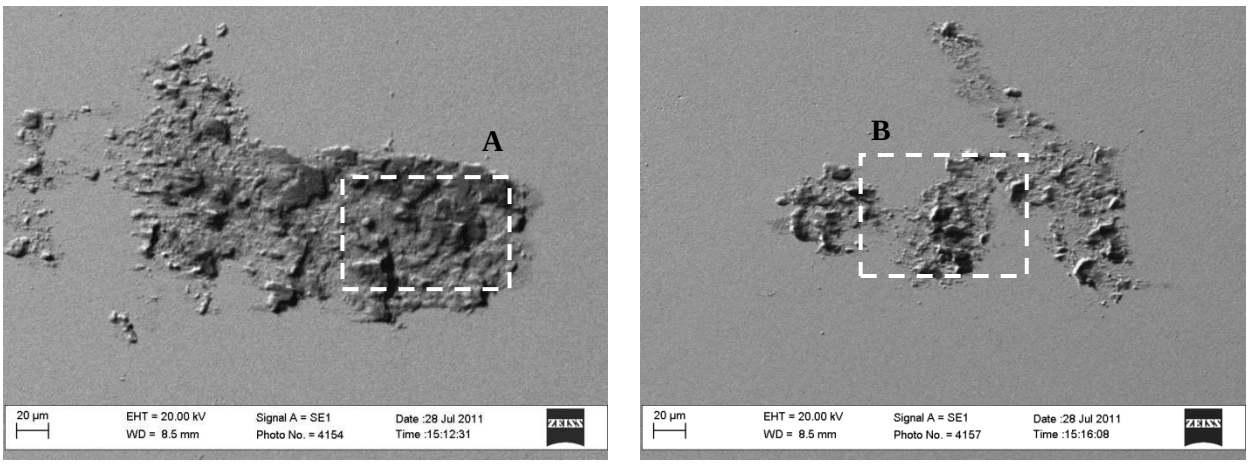

(a) (b)

Figure B.16: Magnified SEM image of area A in Figure B.15(a); (b) Magnified SEM image of area B in Figure B.15(b)

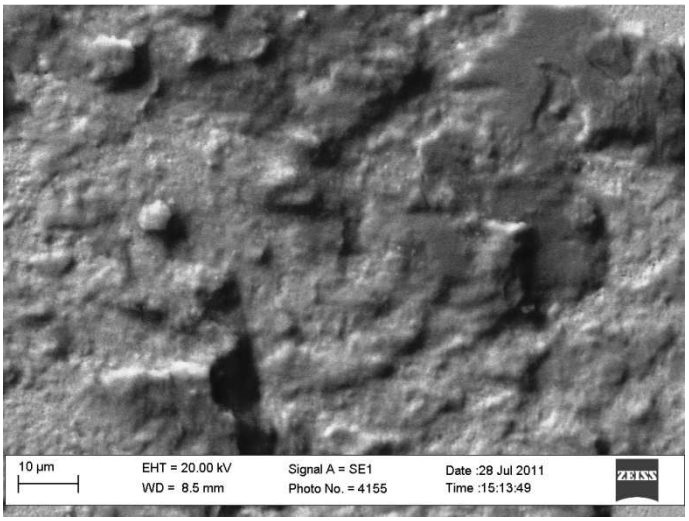

(a)

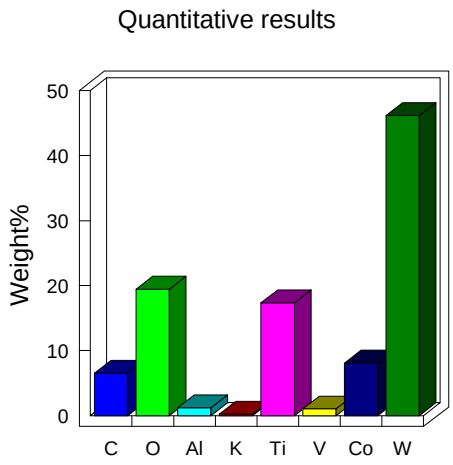

(b)

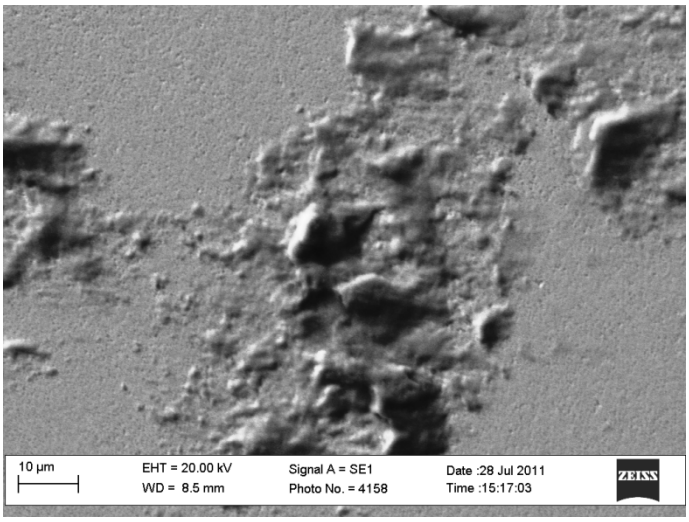

(c)

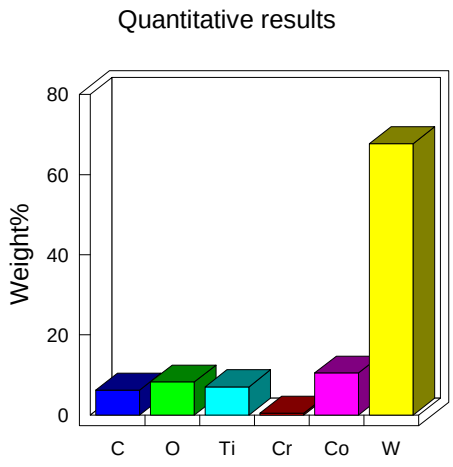

(d)

Figure B.17 (a) SEM image of area A in Figure B.16(a); (b) quantitative EDX analysis of the SEM images in (a); (c) SEM image of area B in Figure B.16(b); (d) quantitative EDX analysis of the SEM images in (c)

Table B.4: Summary of the three quantitative EDX analyses performed on the SEM images in Figure B.17(b) and Figure B.17(d)

	Weight%								
Figure	**C**	**O**	**Al**	**Ti**	**V**	**Cr**	**Co**	**W**	**Total**
Figure B.17(b)	6.525	19.454	1.214	17.340	1.040	0	8.053	46.165	100.000
Figure B.17(d)	6.195	8.211	0	7.030	0	0.418	10.445	67.701	100.000

B.3.2 Ti-6Al-4V Flat on a WC-10wt%Co Flat Fretting Contact

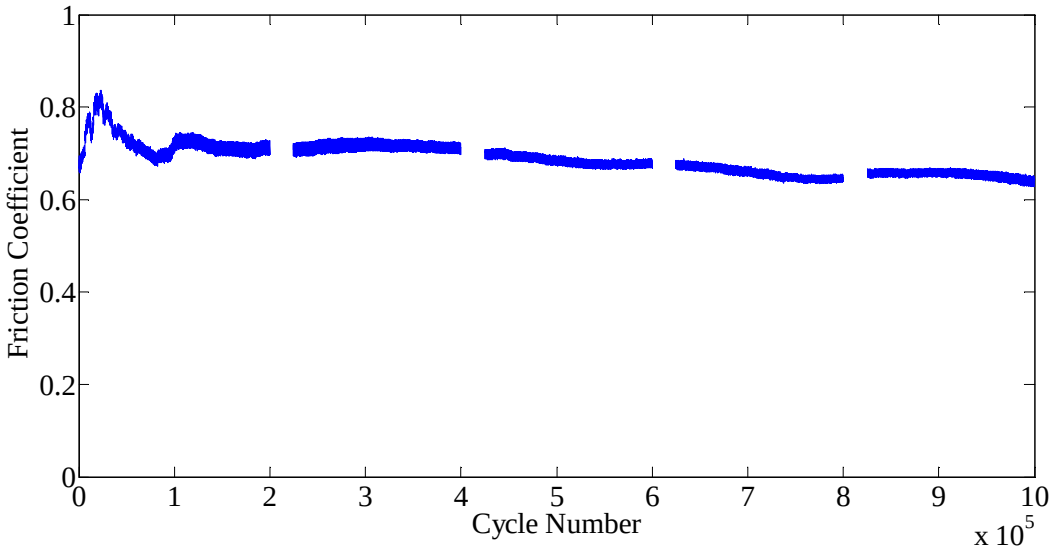

Figure B.18: Coefficient of static friction for Ti-6Al-4V flat on WC-10wt%Co flat fretting contact [Frequency = 80Hz, Slip (peak-to-peak) = 100 micro meter; Cycles = 1000000]

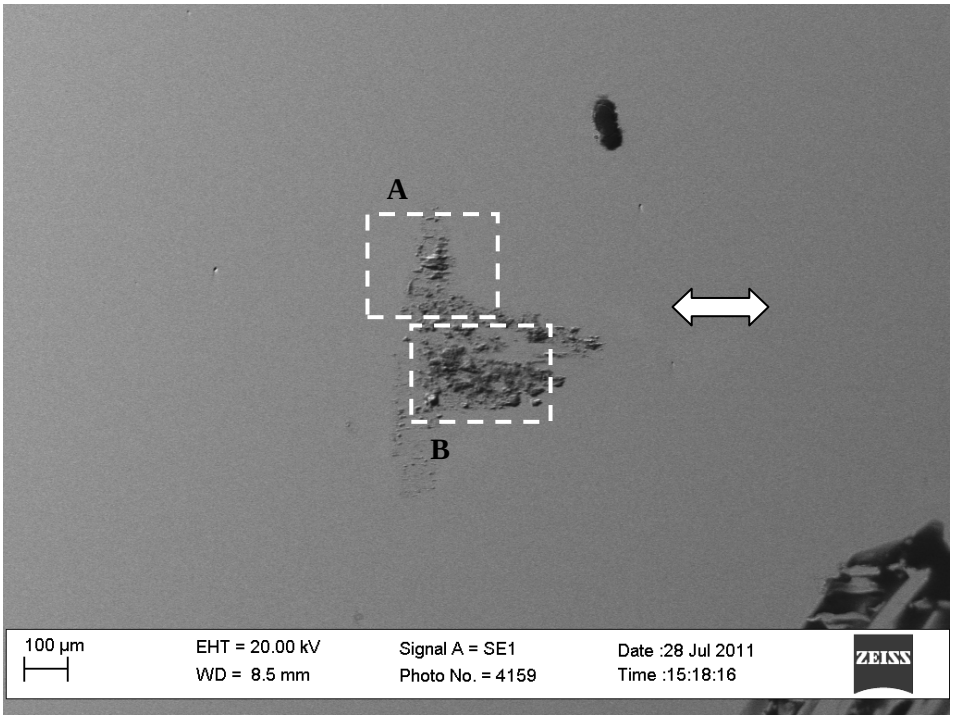

Figure B.19: SEM image of the wear scar on the flat WC-10wt%Co specimen produced by the Ti-6Al-4V cylinder on WC-10wt%Co flat fretting contact

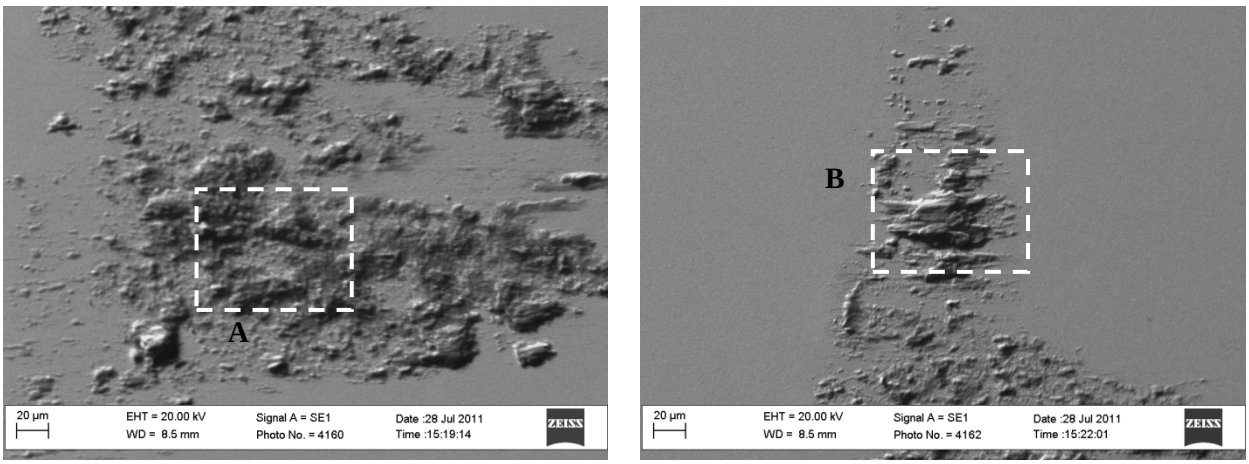

(a) (b)

Figure B.20: Magnified SEM image of area A in Figure B.19; (b) Magnified SEM image of area B in Figure B.19

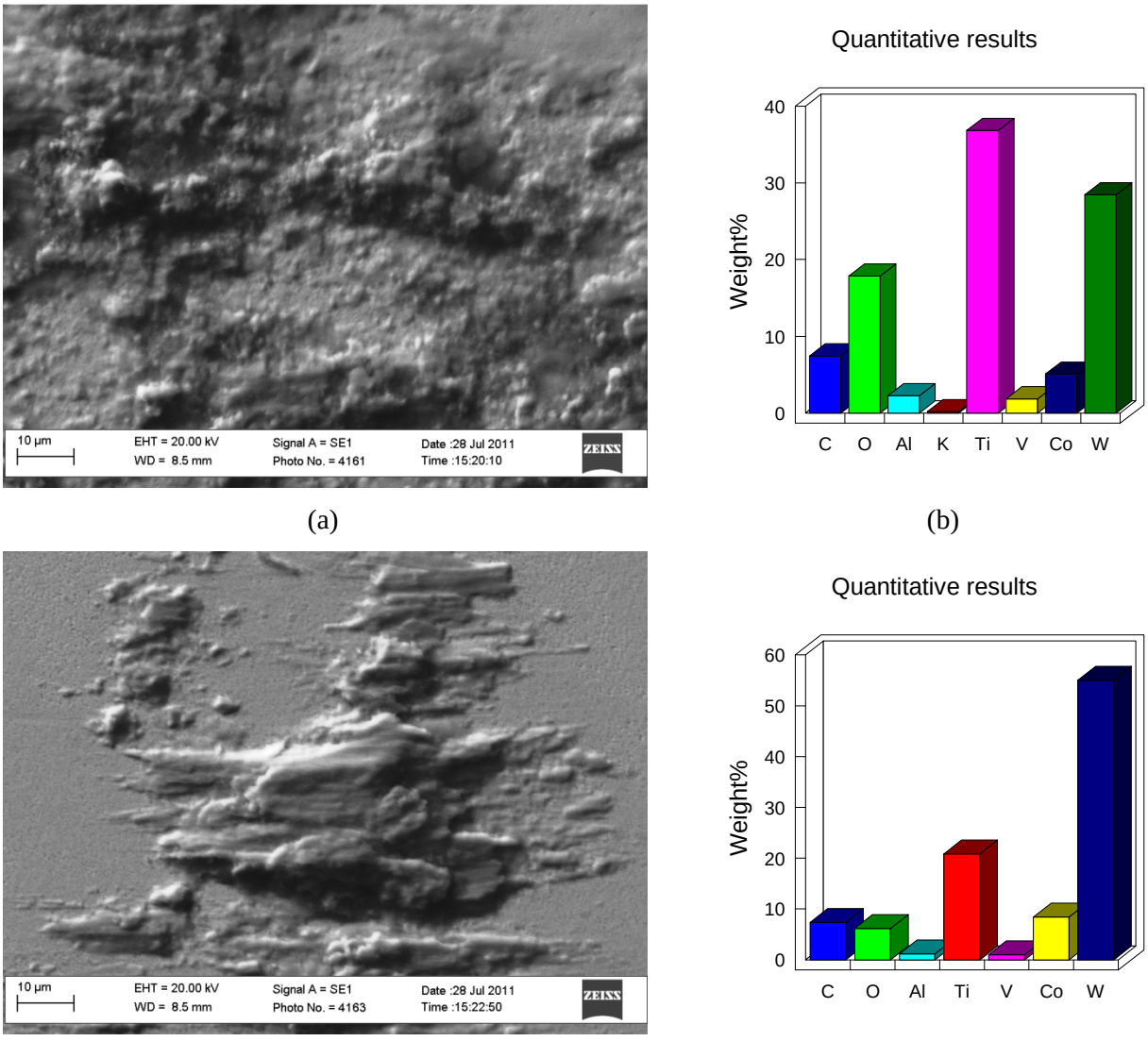

(a) (b)

(c) (d)

Figure B.21: (a) SEM image of area A in Figure B.20(a); (b) quantitative EDX analysis of the SEM images in (a); (c) SEM image of area B in Figure B.20(b); (d) quantitative EDX analysis of the SEM images in (c)

Table B.5: Summary of the three quantitative EDX analyses performed on the SEM images in Figure B.21(b) and Figure B.21(d)

	Weight%							
Figure	**C**	**O**	**Al**	**Ti**	**V**	**Co**	**W**	**Total**
Figure B.21(b)	7.439	17.867	2.274	37.037	1.833	5.089	28.462	100
Figure B.21(d)	7.359	6.145	1.157	20.863	1.024	8.438	55.014	100

B.3.3 Al7075-T6 Cylinder on a WC-10wt%Co Flat Fretting Contact Subjected to Tangential Motion

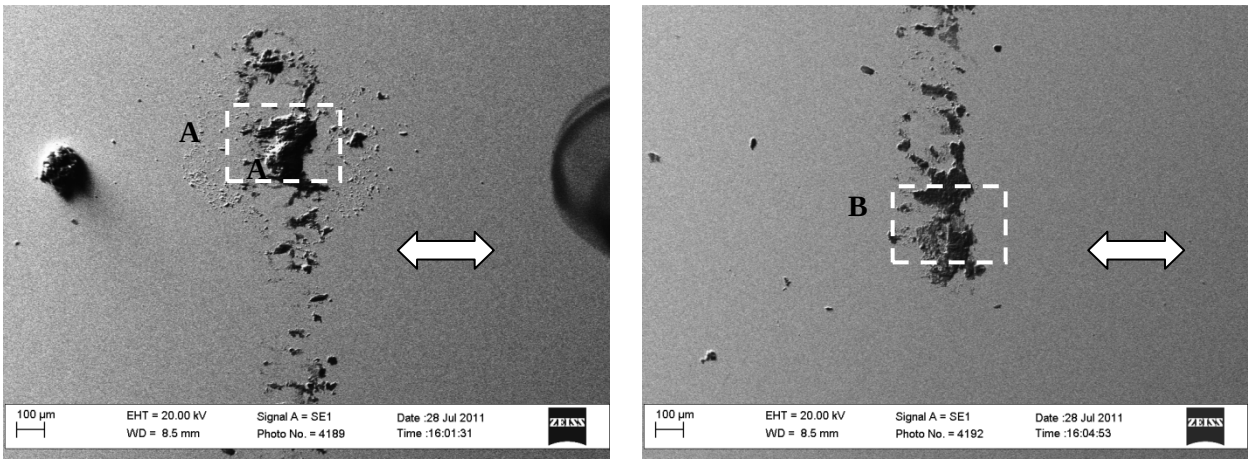

(a) (b)

Figure B.22 Two SEM images of the wear scar on the flat WC-10wt%Co specimen produced by the Al7075-T6 cylinder on WC-10wt%Co flat fretting contact subjected to tangential motion

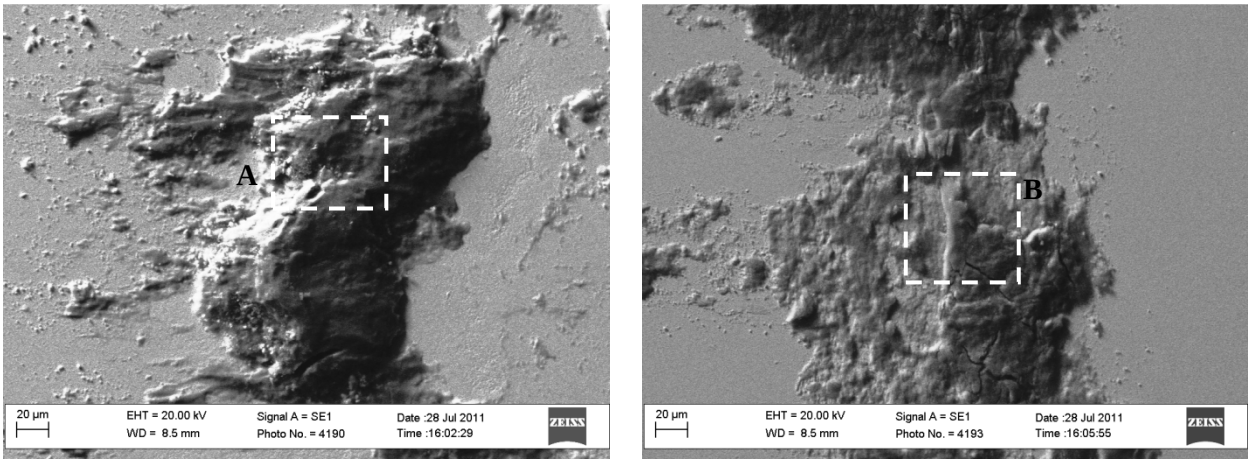

(a) (b)

Figure B.23: Magnified SEM image of area A in Figure B.22(a); (b) Magnified SEM image of area B in Figure B.22(b)

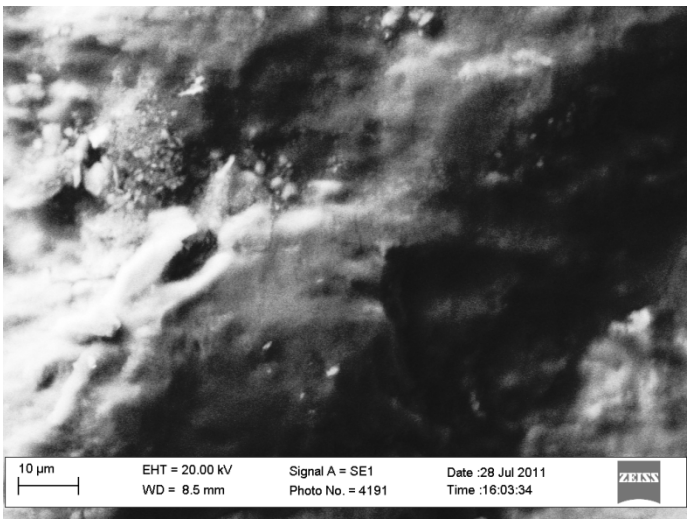

(a)

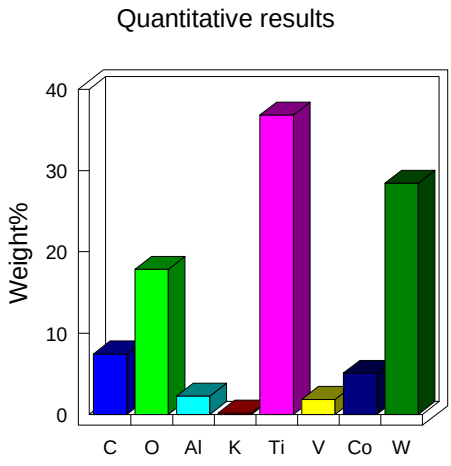

(b)

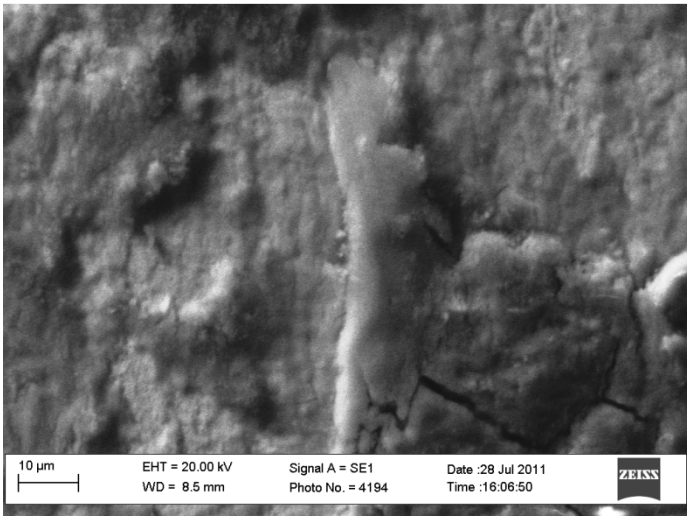

(c)

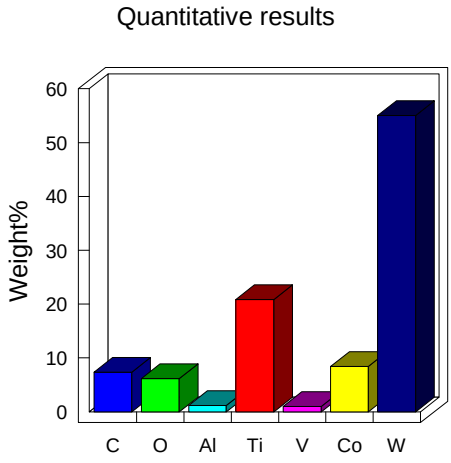

(d)

Figure B.24: (a) SEM image of area A in Figure B.23(a); (b) quantitative EDX analysis of the SEM images in (a); (c) SEM image of area B in Figure B.23(b); (d) quantitative EDX analysis of the SEM images in (c)

Table B.6: Summary of the three quantitative EDX analyses performed on the SEM images in Figure B.24(b) and Figure B.24(d)

	Weight%									
Figure	**C**	**O**	**Mg**	**Al**	**Cr**	**Co**	**Cu**	**Zn**	**W**	**Total**
Figure B.24(b)	4.902	38.233	1.128	42.580	0	1.231	0.804	3.267	7.856	100
Figure B.24(d)	1.953	44.657	0.442	12.911	0.287	5.991	0	0.661	33.098	100

B.4 Fretting Wear of Spark Plasma Sintered Carbides

B.4.1 Ti-6Al-4V Cylinder on a WC – 10wt%Co – 10wt%NbC - 0.3wt%Cr3C2 Flat Fretting Contact Subjected to Axial Motion

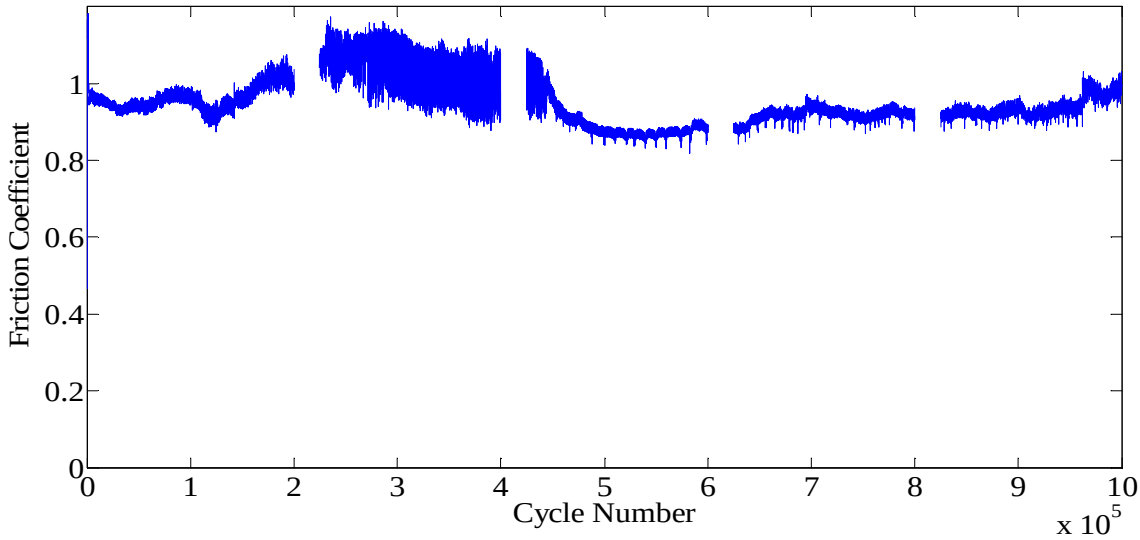

Figure B.25: Coefficient of static friction for Ti-6Al-4V cylinder on WC – 10wt%Co – 10wt%NbC - 0.3wt%Cr3C2 flat fretting contact subjected to axial motion [Frequency = 80Hz, Slip (peak-to-peak) = 100 micro meter; Cycles = 1000000]

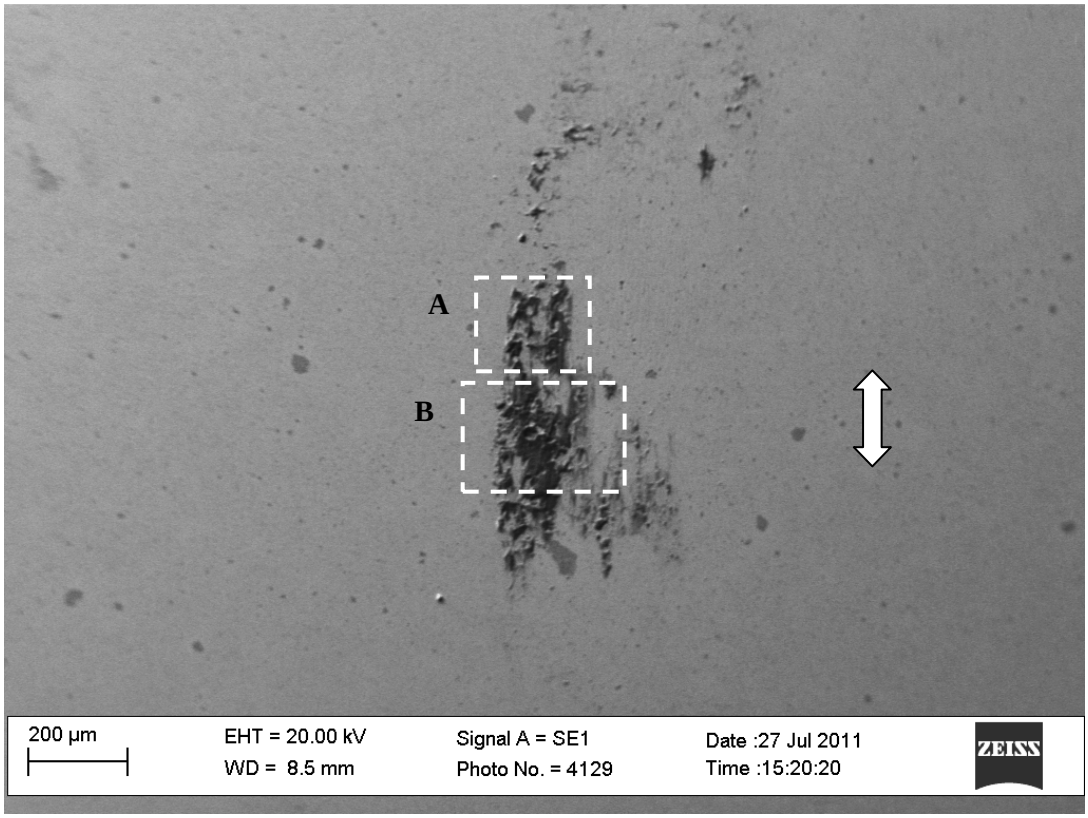

Figure B.26: SEM image of the wear scar on the flat WC – 10wt%Co – 10wt%NbC - 0.3wt%Cr3C2 specimen produced by the Ti-6Al-4V cylinder on WC – 10wt%Co – 10wt%NbC - 0.3wt%Cr3C2 flat fretting contact subjected to axial motion

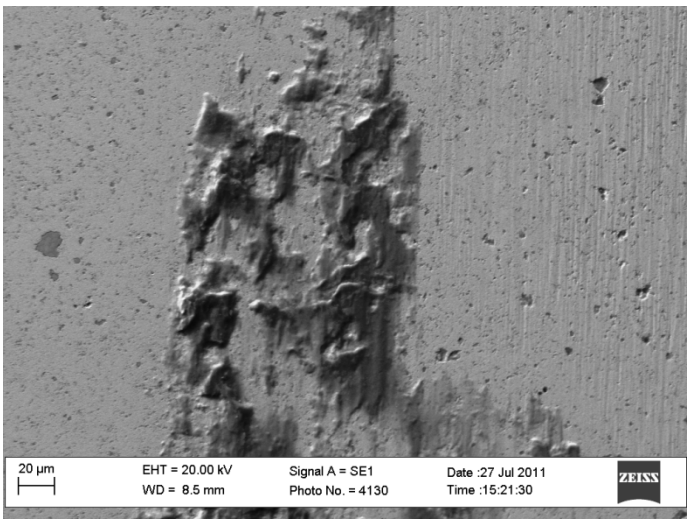

(a)

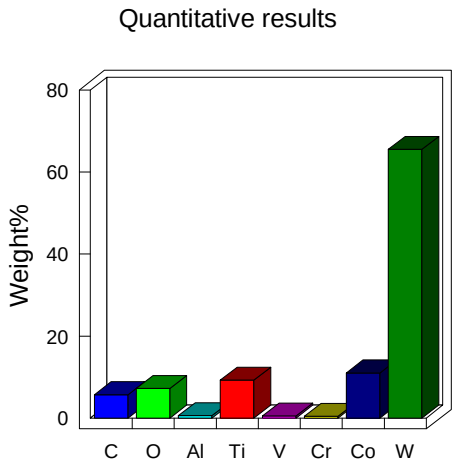

(b)

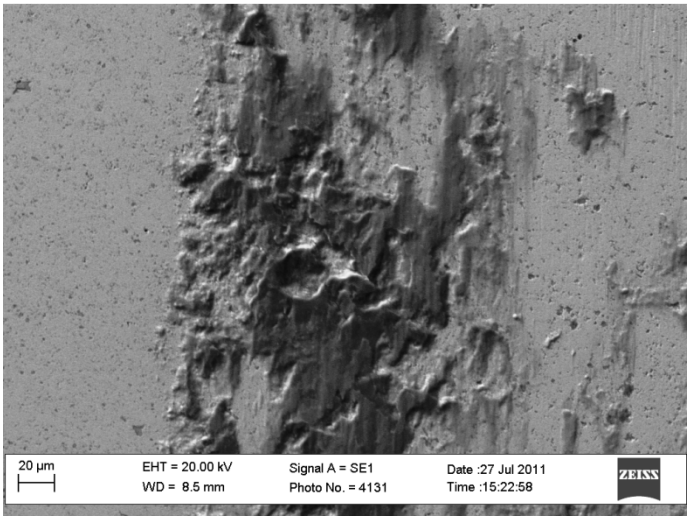

(c)

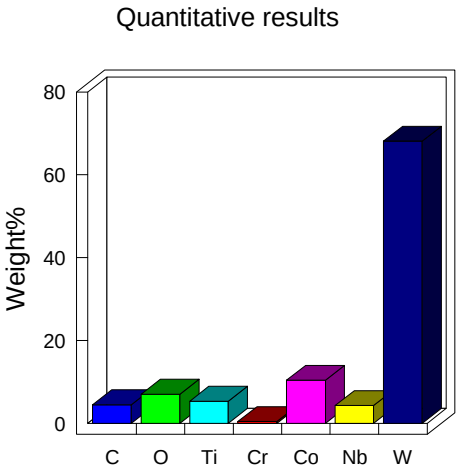

(d)

Figure B.27: a) SEM image of area A in Figure B.26; (b) quantitative EDX analysis of the SEM images in (a); (c) SEM image of area B in Figure B.26; (d) quantitative EDX analysis of the SEM images in (c)

Table B.7: Summary of the three quantitative EDX analyses performed on the SEM images in Figure B.27(b) and Figure B.27(d)

	Weight%								
Figure	**C**	**O**	**Al**	**Ti**	**V**	**Cr**	**Co**	**W**	**Total**
Figure B.27**(b)**	5.685	7.182	0.545	9.254	0.469	0.374	10.967	65.525	100.000
Figure B.27**(d)**	5.633	10.692	1.001	15.615	0.734	0.309	9.927	56.089	100.000

B.4.2 Al7075 Cylinder on a WC – 10wt%Co – 10wt%NbC - 0.3wt%Cr3C2 Flat Fretting Contact Subjected to Axial Motion

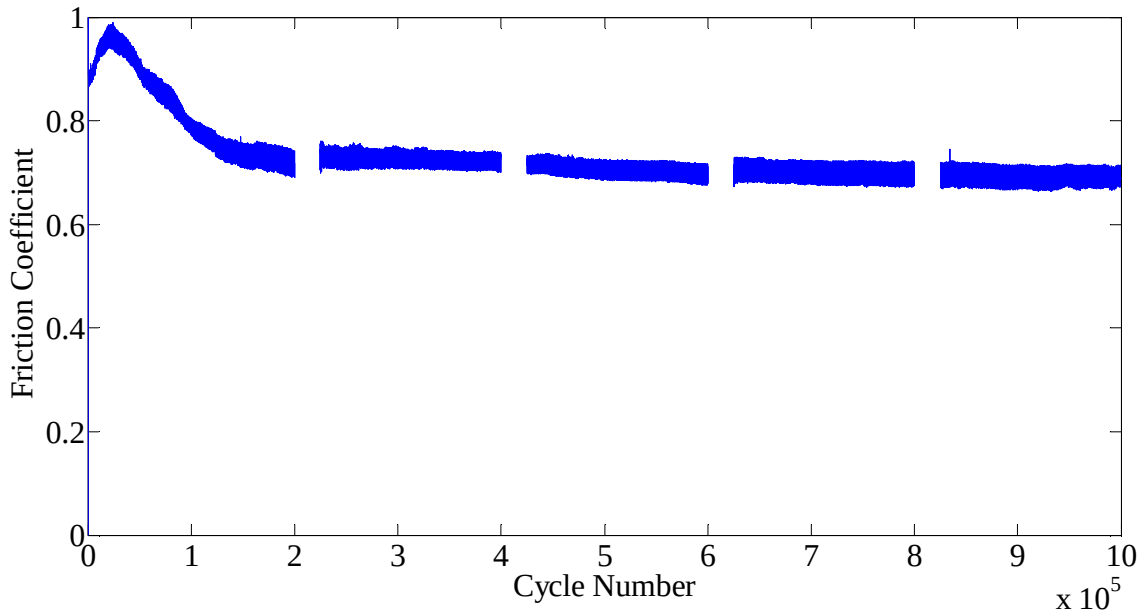

Figure B.28: Figure B.29: Coefficient of static friction for Al7075-T6 cylinder on WC – 10wt%Co – 10wt%NbC - 0.3wt%Cr3C2 flat fretting contact subjected to axial motion [Frequency = 80Hz, Slip (peak-to-peak) = 100 micro meter; Cycles = 1000000]

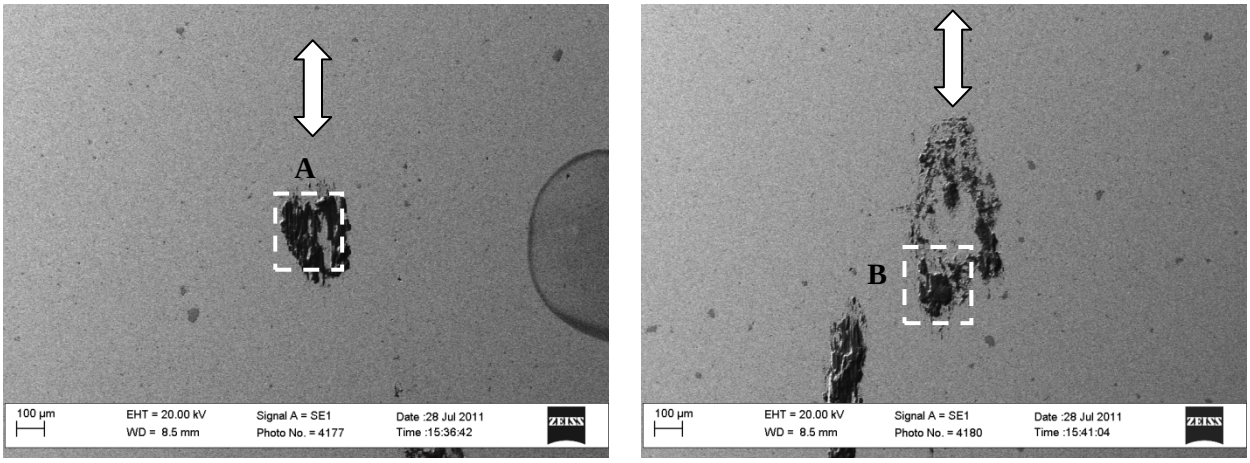

(a) (b)

Figure B.30: Two SEM images of the wear scar on the flat WC – 10wt%Co – 10wt%NbC - 0.3wt%Cr3C2 specimen produced by the Al7075-T6 cylinder on WC – 10wt%Co – 10wt%NbC - 0.3wt%Cr3C2 flat fretting contact subjected to axial motion

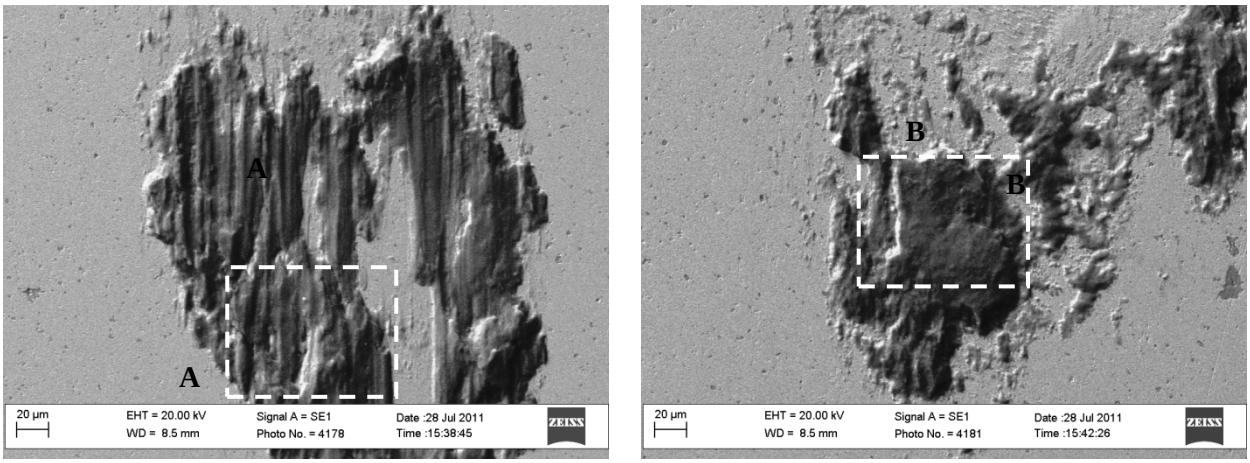

(a) (b)

Figure B.31: Magnified SEM image of area A in Figure B.30; (b) Magnified SEM image of area B in Figure B.30

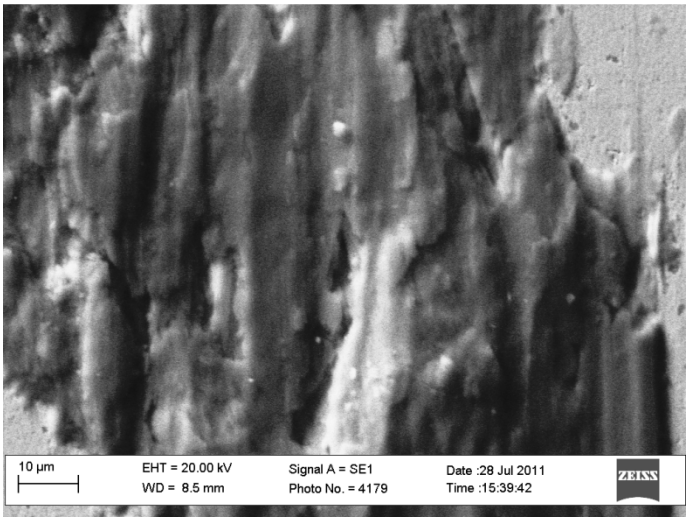

(a)

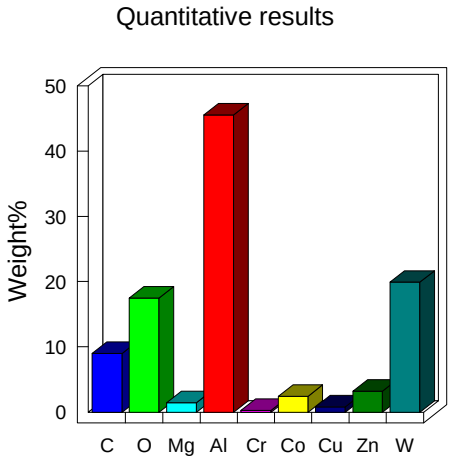

(b)

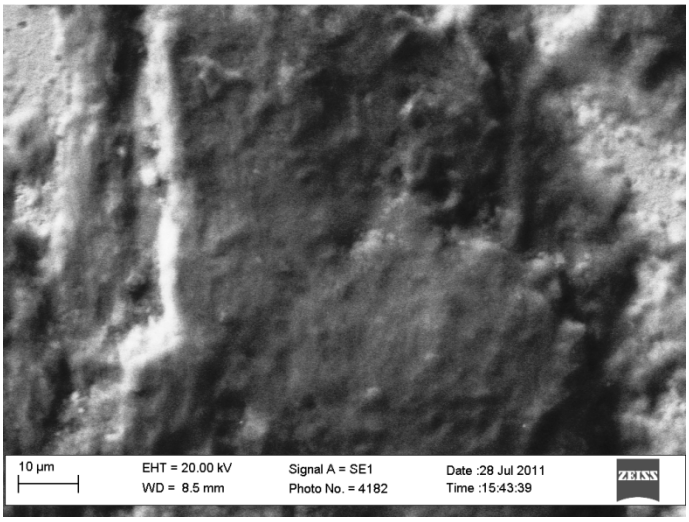

(c)

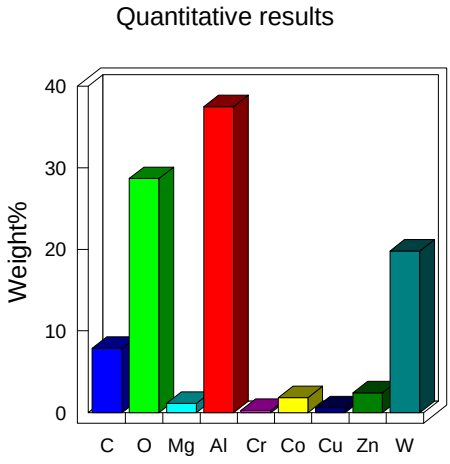

(d)

Figure B.32: (a) SEM image of area A in Figure B.31(a); (b) quantitative EDX analysis of the SEM images in (a); (c) SEM image of area B in Figure B.31(b); (d) quantitative EDX analysis of the SEM images in (c)

Table B.8: Summary of the three quantitative EDX analyses performed on the SEM images in Figure B.32(b) and Figure B.32(d)

	Weight%									
Spectrum	**C**	**O**	**Mg**	**Al**	**Fe**	**Cu**	**Zn**	**Ag**	**W**	**Total**
5-2-1-1-1	8.969	17.460	1.437	45.521	0.242	2.431	0.809	3.224	19.906	100.000
5-2-2-1-1	7.866	28.660	1.123	37.464	0.245	1.834	0.575	2.440	19.794	100.000

C APPENDIX C

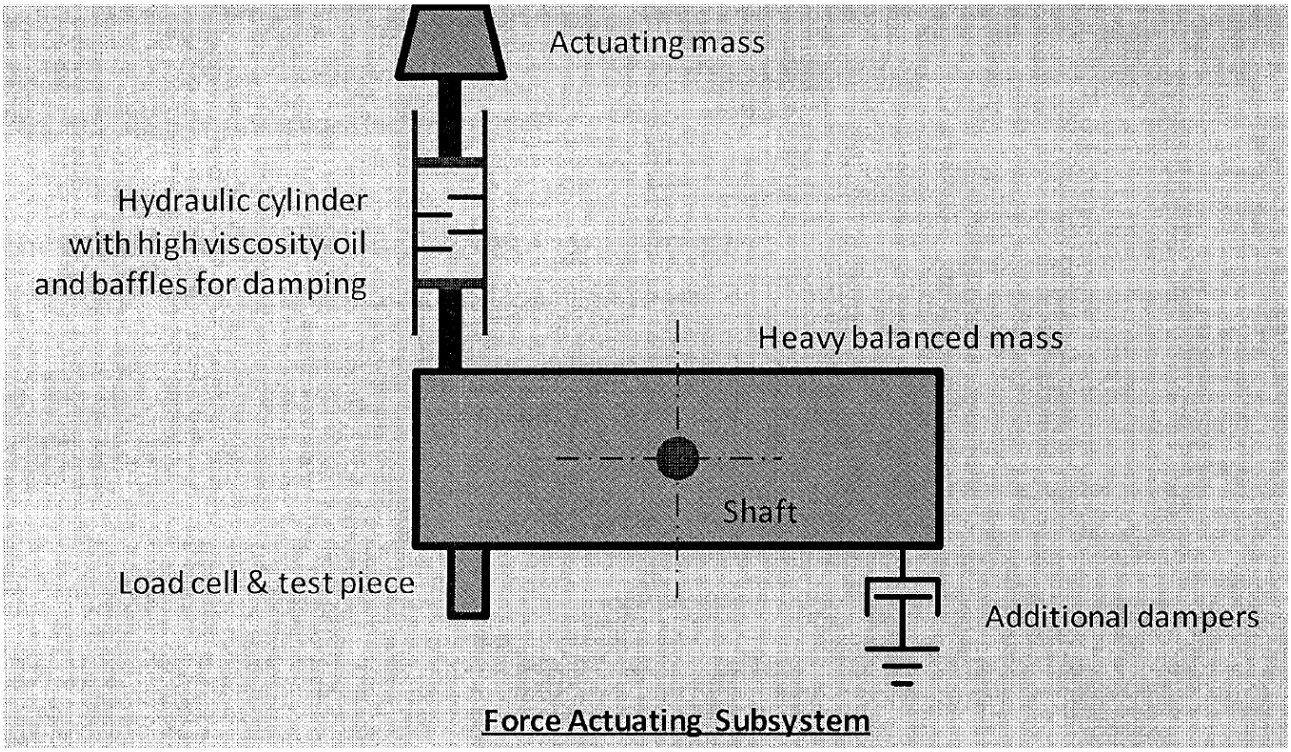

Figure C.1 Improved Force Application Subsystem